VILNIUS UNIVERSITY
CENTER FOR PHYSICAL SCIENCES AND TECHNOLOGY

MARTYNAS MISEVIČIUS

SYNTHESIS, STRUCTURAL CHARACTERIZATION AND OPTICAL PROPERTIES OF SELECTED STRONTIUM ALUMINATES

Doctoral Dissertation

Physical Sciences, Chemistry (03 P)

Vilnius, 2016

The disssertation was carried out from 2012 to 2016 at Vilnius University.

Scientific supervisors:

Prof. Habil. Dr. Aivaras Kareiva
Vilnius University, Physical Sciences, Chemistry – 03 P
(From 2012-10-01 to 2015-06-15)

Prof. Dr. Jurgis Barkauskas
Vilnius University, Physical Sciences, Chemistry – 03 P
(From 2015-06-16 to 2016-09-30)

VILNIAUS UNIVERSITETAS
FIZINIŲ IR TECHNOLOGIJOS MOKSLŲ CENTRAS

MARTYNAS MISEVIČIUS

PASIRINKTŲ STRONCIO ALIUMINATŲ SINTEZĖ, STRUKTŪRINIS APIBŪDINIMAS IR OPTINĖS SAVYBĖS

Daktaro disertacija

Fiziniai mokslai, Chemija (03 P)

Vilnius, 2016

Disertacija rengta 2012–2016 metais Vilniaus universitete.

Moksliniai vadovai:

Prof. Habil. Dr. Aivaras Kareiva
Vilniaus universitetas, fiziniai mokslai, chemija – 03 P
(Nuo 2012-10-01 iki 2015-06-15)

Prof. Dr. Jurgis Barkauskas
Vilniaus universitetas, fiziniai mokslai, chemija – 03 P
(Nuo 2015-06-16 iki 2016-09-30)

Contents

Acronyms

FTIR Furier Transform Infra-Red Spectroscropy

XRD X-Ray Diffractometry

PL Photoluminescence

TG Thermogravimetry

SEM Scanning Electron Microscopy

LED Light Emitting Diode

UV Ultraviolet

Vis Visible (part of light spectrum)

NMR Nuclear Magnetic Resonance

VUV Vacuum Ultraviolet

PSF Peak Shape Function

FWHM Full Width at Half Max

PDF Powder Diffraction File

ICSD Inorganic Crystal Structure Database

Introduction

The discovery of advanced optical materials with multiple superior qualities for display applications remains a difficult problem. The specific luminescence properties of multinary oxides are highly sensitive to the changes in dopant composition, host stoichiometry, and processing conditions [1, 2, 3, 4]. Part of the widely studied inorganic luminescent materials is the group of strontium aluminates. In $SrO-Al_2O_3$ system, there are several possible phases, namely $Sr_3Al_2O_6$, $SrAl_2O_4$, $SrAl_4O_7$, $SrAl_{12}O_{19}$, $Sr_2Al_6O_{11}$, $Sr_7Al_{12}O_{25}$, $Sr_4Al_{14}O_{25}$, $Sr_{12}Al_{14}O_{33}$ and $Sr_{10}Al_6O_{19}$, as described in the literature [5]. The most studies on strontium aluminates are related with the strong green emission ($\sim 530\,\mathrm{nm}$) of Eu^{2+} in stoichiometric $SrAl_2O_4$ with monoclinic trydimite structure [6, 7]. Another interesting system is orthorhombic $Sr_4Al_{14}O_{25}$:Eu^{2+},Dy^{3+} with its blue emission around $490\,\mathrm{nm}$ [8, 9]. Such systems exhibit phenomenon called persistent luminescence [10] with afterglow time of several hours [11]. In addition to higher chemical stability, the intensity and the duration of the phosphorescence of $SrAl_2O_4$:Eu^{2+},Dy^{3+},B^{3+} make it possible to observe a continuous light emission for $10\,\mathrm{h}$ [12]. Last two decades have brought a lot of research in the field of persistent luminescence, however, only a handful of systems exist, that are bright enough to consider their use in practical applications [13]. Moreover, there is a great lack of materials that exhibit long and bright afterglow in longer wavelengths (like yellow, orange and red). Another open question in this field is the mechanism of persistent luminescence, since there is some kind of agreement on general mechanism, however many details remain unclear [10, 13, 14].

The current study aims on expanding the knowledge related to strontium aluminates in perspective of persistent phosphors. It is generally agreed that defects play an important role in prolonging the afterglow. Therefore, the synthesis route of host materials plays major role in characteristics of phosphors. Most commonly such materials are synthesized by conventional solid-state reaction between oxides, but in our case an aqueous sol-gel synthesis route was chosen as the main preparative method. On the other hand, the successful synthesis

of monophasic $SrAl_4O_7$ using solid-state reaction method, to the best of our knowledge, is reported for the first time. In this study, Ce^{3+} was often chosen as an activator as it is one of most promising ions in non-Eu^{2+} based persistent phosphors [14]. Cerium is cheaper and requires milder reducing conditions in comparison to europium, so efficient Ce^{3+} based persistent phosphor might lead to commercially competitive product in the market.

The main tasks of the present thesis are synthesis and characterization of monophasic strontium aluminates:

1) undoped and cerium-doped $SrAl_2O_4$, $Sr_3Al_2O_6$, $SrAl_{12}O_{19}$ and $Sr_4Al_{14}O_{25}$ by aqueous sol-gel route;

2) calcium or barium substituted $Sr_4Al_{14}O_{25}$ by conventional solid-state reaction method;

3) undoped, europium-doped and dysprosium co-doped $SrAl_4O_7$ by aqueous sol-gel route and conventional solid-state reaction method.

1 Subject Literature Review

1.1 Strontium aluminates

Strontium aluminates are a range of minerals found naturally or obtained artificially by heating strontium oxide and aluminum oxide together at high temperatures. They are known in refractory and cement industry although their closely related calcium counterparts are much more common [5]. The $SrO-Al_2O_3$ system phase diagram has been described in 1959 by Massazza [15] and, although incomplete, it is the most cited one. The complete phase diagram was published in 1979 [16] and in 2006 it was modeled theoretically by Ye *et al.* [17]. Resulting diagram of this study, along with comparison with other works is presented in figure1.1.

As seen from figure 1.1, at ambient conditions there are four stable compounds – $Sr_3Al_2O_6$, $SrAl_2O_4$, $SrAl_4O_7$ and $SrAl_{12}O_{19}$. The authors decided not to include $Sr_4Al_{14}O_{25}$ as its composition is close to $SrAl_4O_7$ [17], although it is well known structure and modification of part of $SrO-Al_2O_3$ phase diagram has been suggested by Capron and Douy (Figure 1.2) [18].

These five phases ($Sr_3Al_2O_6$, $SrAl_2O_4$, $Sr_4Al_{14}O_{25}$, $SrAl_4O_7$ and $SrAl_{12}O_{19}$) will be described in detail later in this section. Moreover, it should be mentioned, that more strontium aluminate phases are encountered in the literature, namely $Sr_{12}Al_{14}O_{33}$[19], $Sr_{10}Al_6O_{19}$ [20], $Sr_2Al_6O_{11}$ [21] and $Sr_7Al_{12}O_{25}$ [22].

Yamaguchi *et al.* has synthesized $Sr_{12}Al_{14}O_{33}$ using sol-gel synthesis [19]. Later it was confirmed that this compound is isostructural with $Ca_{12}Al_{14}O_{33}$ and is cubic with space group $I\bar{4}3d$ (№ 220) and cell parameter $a = 12.322$ Å [23]. To our extent of knowledge, besides these two studies no more structural analysis has been made on the crystal structure. Although there are some research of preparation and characterization of epitaxial thin films of $Sr_{12}Al_{14}O_{33}$ prepared using pulsed laser deposition [24, 25] and also recent studies of using this phase as catalyst (after incorporation of Ni or Ru ions) [26, 27, 28].

Kahlenberg has found and characterized single crystals of $Sr_{10}Al_6O_{19}$ on the

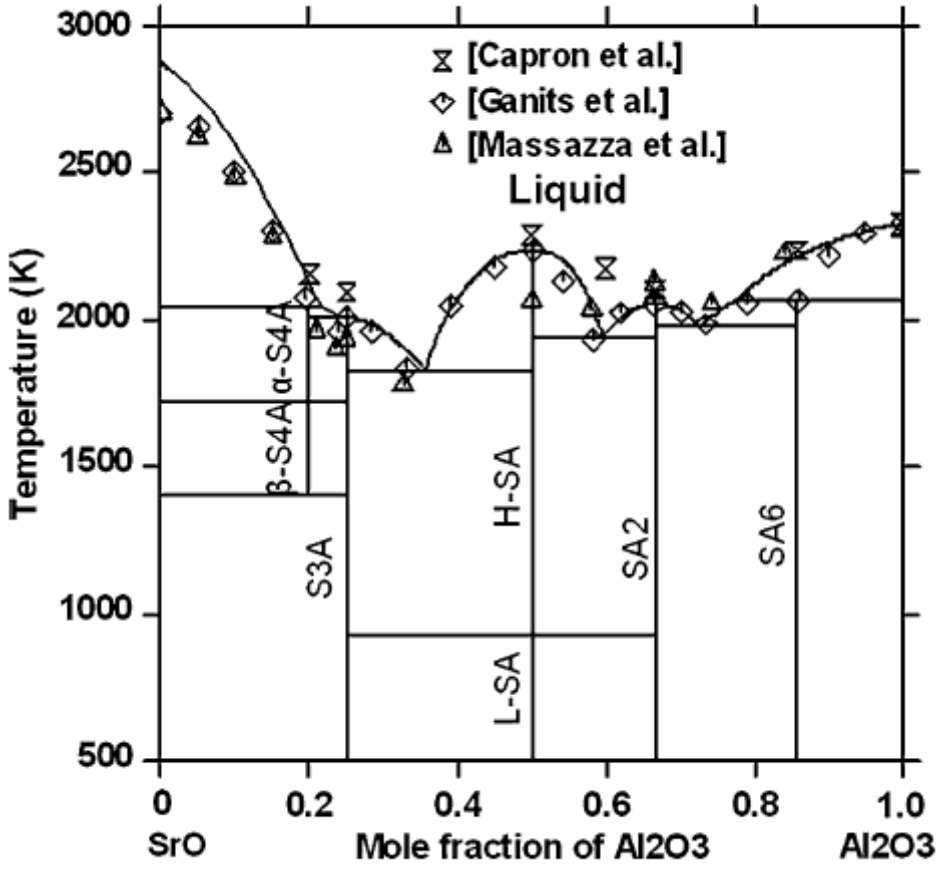

Figure 1.1. Calculated phase diagram compared with experimental data (S = SrO, A = Al_2O_3) [17].

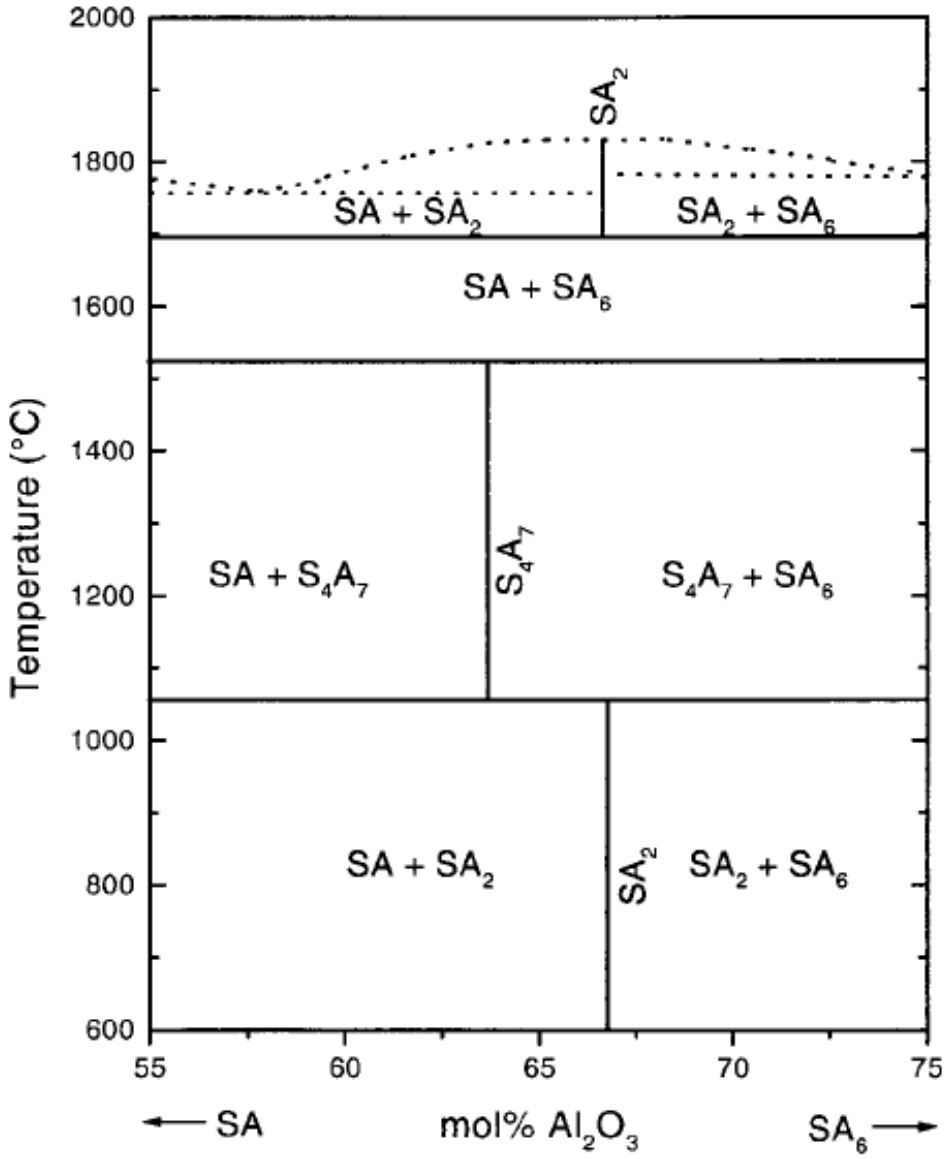

Figure 1.2. Proposed modification of a part of the $SrO-Al_2O_3$ phase diagram showing the closely related domains of stability of $SrAl_4O_7$ and $Sr_4Al_{14}O_{25}$ (S = SrO, A = Al_2O_3) [18].

surface of strontium-rich pellets sintered at $1600\,^{\circ}\mathrm{C}$ for $144\,\mathrm{h}$ [20]. Unfortunately, despite few claims that $Sr_{10}Al_6O_{19}$ has formed as side phase in the mixture of strontium aluminates, this is the only source confirming existence of such structure.

First discovered by Smets *et al.* $Sr_2Al_6O_{11}$:Eu^{2+}, is reported as blue-green phosphor and has crystal structure close to $Sr_{1.33}Pb_{0.67}Al_6O_{11}$ [29]. This was later questioned by Wang and Wang as their study on $Sr_2Al_6O_{11}$ revealed that the product consists of two phases – $SrAl_2O_4$ and $Sr_4Al_{14}O_{25}$ [30]. However, Takeda *et al.* prepared and characterized crystal structure of $Sr_2Al_6O_{11}$, although obtained samples contained impurity phases of other strontium aluminates [21].

$Sr_7Al_{12}O_{25}$ has been described by Nevskij as having trigonal crystal structure with space group $P3$ (№ 143) and cell parameters $a = 17.91$ and $c = 7.16$ Å [22, 31]. Doped with Eu^{2+} it is claimed to be a violet phosphor [32], but any more studies, to our knowledge, has not been published.

1.1.1 $SrAl_2O_4$

For more than a century, $SrAl_2O_4$ has been known by mineralogists and was described as having tridymite-like structure (a derivative of polymorph of silica) [33]. It has been synthesized and described as being structurally similar to barium aluminate [34]. Ito *et al.* found that at high temperature strontium aluminate has the undistorted $BaAl_2O_4$ structure, but undergoes reversible phase transition to lower symmetry at temperature of $650\,^{\circ}\mathrm{C}$ and suggested to call low-temperature (monoclinic) and high-temperature (hexagonal) as α- and β-$SrAl_2O_4$, respectively [35]. The results of in situ high-temperature X-ray and neutron powder diffraction experiments showed that in fact the material undergoes two reversible phase transitions $P2_1 \Longleftrightarrow P6_3$ and $P6_3 \Longleftrightarrow P6_322$ at $\sim$680 and $\sim 860\,^{\circ}\mathrm{C}$, respectively [7].

The room temperature $SrAl_2O_4$ has a monoclinic structure of stuffed tridymite with space group $P2_1$ (№ 4) and cell parameters $a = 8.447$, $b = 8.816$, $c = 5.163$ Å, $\alpha = 90$, $\beta = 93.42$, $\gamma = 90°$ [36]. The structure of the low-temperature phase (see figure 1.3) has a three-dimensional network of corner-sharing AlO_4 tetrahedra, which has channels in the a- and c-directions where the Sr^{2+} ions are located. There are two crystallographically different sites for Sr^{2+}, which have identical coordination numbers (i.e., 6+1), similar average Sr−O distances (i.e., 2.695 Å and 2.667 Å) and similar individual Sr−O distances. The two environ-

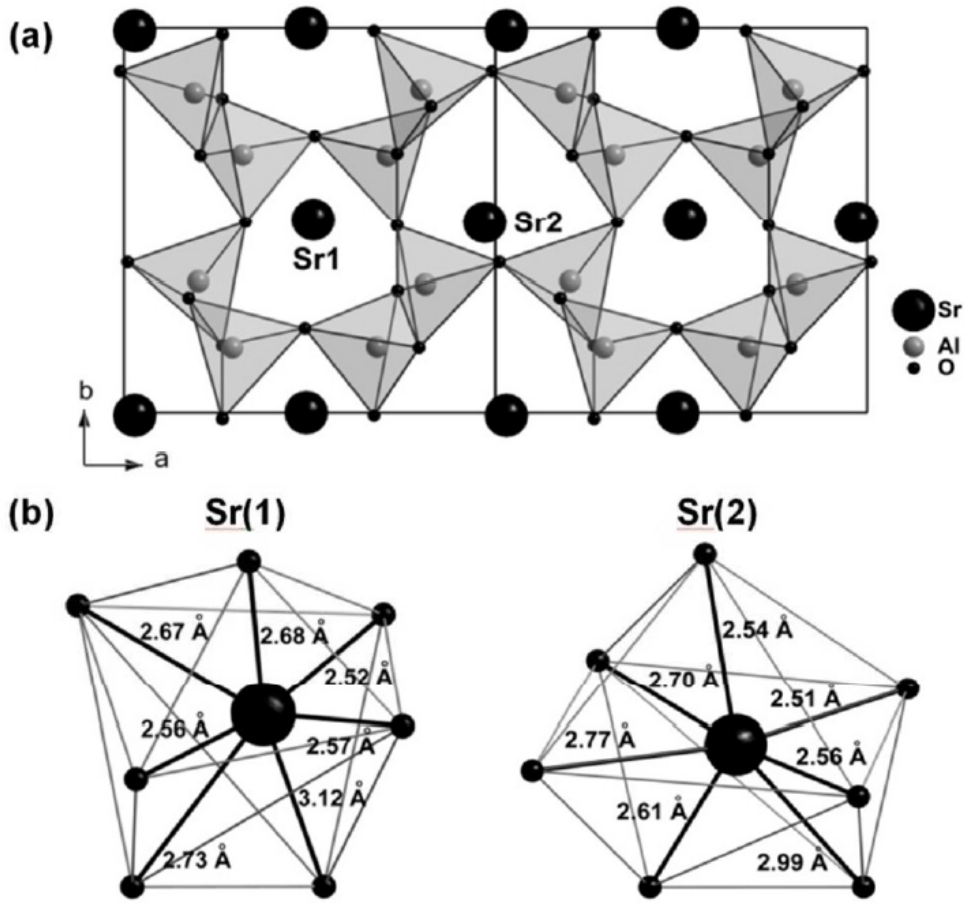

Figure 1.3. (a) Unit cell of $SrAl_2O_4$ along the c-axis, (b) Local coordination geometry environment of Sr^{2+} [37].

ments differ only by a slight distortion of their "square planes" [12].

Usually, $SrAl_2O_4$ is being doped (and quite often, co-doped) with rare-earth elements, in most cases – Eu^{2+}, which enables it to exhibit persistent luminescence [11]. It has been prepared by solid-state reaction [38], sol-gel synthesis [39], combustion synthesis [40], floating-zone technique [41], laser-heated pedestal growth method [42], microwave route [43], molten salt method [44], hydrothermal synthesis [45], electrospinning preparation [46], microemulsion route [47] and spray-drying technique [5]. It should be mentioned that not all the techniques lead to identical crystallographic and luminescent properties of the end products [13]. For example, $SrAl_2O_4$:Eu,Dy phosphors prepared by sol-gel processing shows a blue shift of the emission spectrum, possibly due to the small grain size, compared to the solid-state synthesis products [48].

As mentioned above, $SrAl_2O_4$ is a popular host in preparation of persistent luminescent materials [10, 49, 50] [40-42]. Doped with Eu^{2+} and co-doped with

Dy^{3+} it exhibits fluorescence in green region ($\lambda_{max} \approx 520\,\mathrm{nm}$) and afterglow lasting for more than $30\,\mathrm{h}$ [11]. Quite recently a new interest has sparked in trivalent dysprosium doped strontium aluminate ($SrA_{12}O_4$:Dy^{3+}) [51, 52, 53, 54, 55]. Various attempts have been made to improve luminescence and afterglow properties of $SrAl_2O_4$:Eu^{2+},Dy^{3+} by incorporating more co-dopants into the system, such as Ce^{3+} [56], Ho^{3+} [57], Er^{3+} [58], Nd^{3+} [59], Tb^{3+} [60] or replacing dysprosium with other lanthanides [41, 45, 61]. Other activators also have been used in $SrAlO_4$ host, namely Ce^{3+} [62] and Ce^{3+}, Mn^{2+} [63] exhibiting long afterglow in the UV and green region, respectively. Moreover, there are studies on dopants, such as Cr^{3+} [64], Pr^{3+} [65], Tb^{3+} [66], Er^{3+} and Yb^{3+} [67]. These studies are interesting fundamentally, although only Eu^{2+} activated and Dy^{3+} co-doped $SrAl_2O_4$, to our knowledge, has been commercialized successfully.

1.1.2 $Sr_3Al_2O_6$

$Sr_3Al_2O_6$ has also been known since early 1900s [68] and was considered isostructural with $Ca_3Al_2O_6$ [69]. Alonso *et al.* refined the structure from neutron diffraction data and described it as a superstructure of the perovskites (ABO_3) [70]. Its conversion to hydrogarnet, $Sr_3Al_2(O_4H_4)_3$, has attracted some more structural studies, since this conversion in calcium aluminate system is one of the principal hydration reactions in the setting of Portland cements [71, 72, 73].

$Sr_3Al_2O_6$ has a cubic structure with space group $Pa\bar{3}$ (№ 205) and cell parameter $a = 15.8425\,\text{Å}$ [70]. The structure (Figure 1.4) consists of rings of six corner-sharing AlO_4 tetrahedra with the resulting Al_6O_{18} rings centered on a three-fold axis and held together by the Sr^{2+} cations. There are six sites occupied by the Sr^{2+} cations. These can be divided into two groups, the three six-coordinated sites and the three sites with higher coordination numbers [72].

Synthesis routes for $Sr_3Al_2O_6$ and its doped versions are similar as previously, namely solid state reaction [70], floating-zone technique [74], microwave synthesis [75], citric-acid route [76], sol-gel technique [77], combustion synthesis [78], co-precipitation technique [79], hydrothermal method [80] and spray-drying technique [5].

$Sr_3Al_2O_6$:Eu,Dy has been studied as a luminescent material. Its emission colour is disputed, since the published results are quite contradictory [13]. Katsumata *et al.* reported that emission consists of broad peaks at 420 and $480\,\mathrm{nm}$

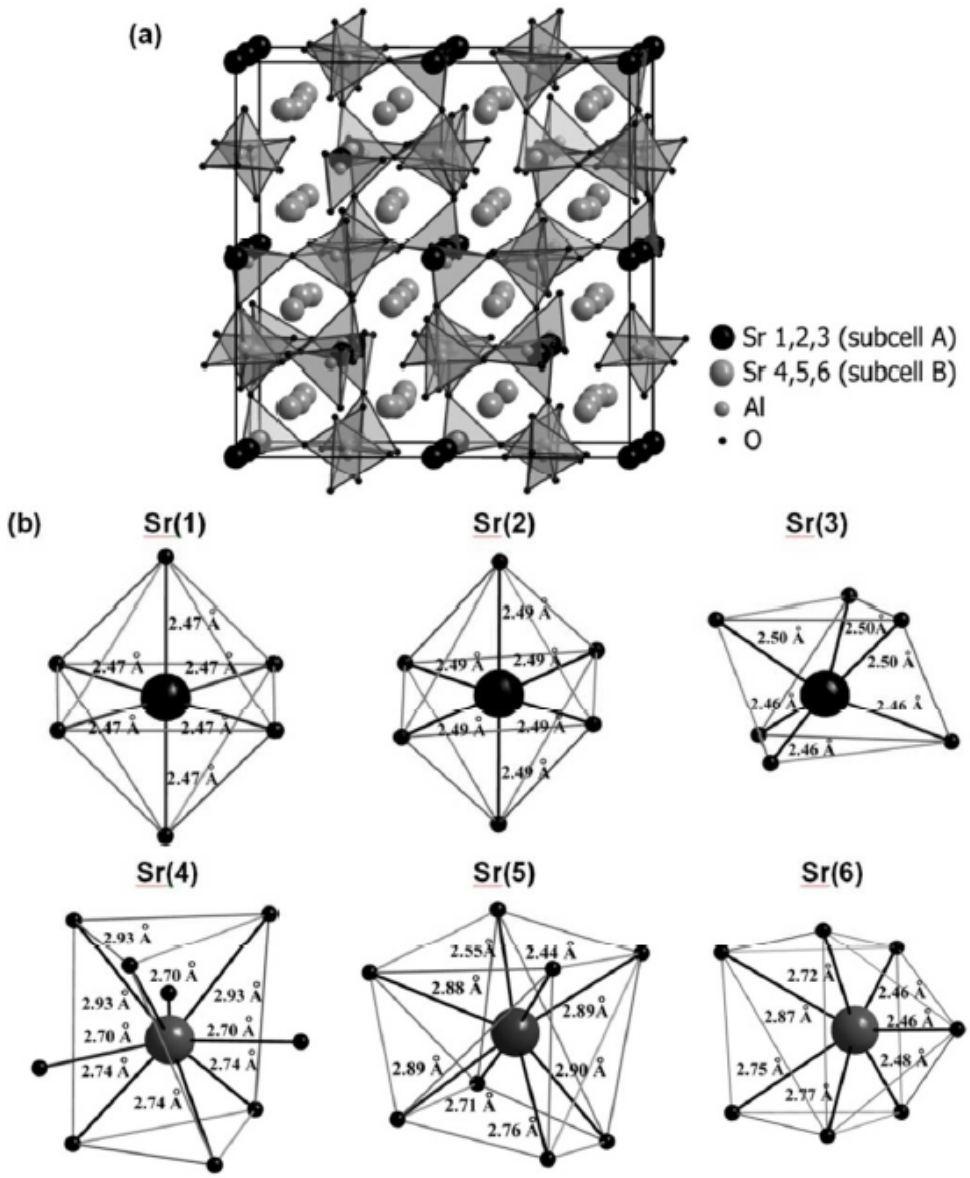

Figure 1.4. (a) Unit cell of $Sr_3Al_2O_6$ (b) Local coordination geometry environment of nonequivalent Sr^{2+} sites [37].

with additional emission of Dy^{3+} peaking at 580, 620 and $700\,\mathrm{nm}$ [74] and no afterglow was observed. On the other hand, there are reports, that Eu^{2+},Dy^{3+}-doped $Sr_3Al_2O_6$ behaves as red light emitting persistent luminescent material with broad band peak at $612\,\mathrm{nm}$ [75, 77, 81, 82], $614.2\,\mathrm{nm}$ [83] or $618\,\mathrm{nm}$ [84, 85]. However, other authors claim that emission of Eu^{2+} in $Sr_3Al_2O_6$ host matrix occurs at $\sim 510\,\mathrm{nm}$ [86, 87, 88, 89, 90]. One possible explanation of these confusing results might be different synthesis routes used [13] – red emission is observed when sol-gel [77, 82, 84, 85], microwave [75, 81] or co-precipitation [79] synthesis routes were used, while green emission is attributed to solid state synthesis [86, 87, 88, 89]. Although, there are exceptions – red emission after solid state synthesis [83] or green emission after sol-gel route [90]. Another explanation might be different oxidation states of europium. As shown by several publications, Eu^{2+} and Eu^{3+} exhibit different photoluminescence – broad band emission at $\sim 512\,\mathrm{nm}$ due $d{-}f$ transitions or sharp peaks at 591 and $610\,\mathrm{nm}$ due $f{-}f$ transitions, respectively [86, 87, 89]. The third explanation might be different excitation wavelengths – usually red emission is reported when excitation is around $472\,\mathrm{nm}$ [75, 77, 81, 84, 85], or lays at $516\,\mathrm{nm}$ under the excitation of $360\,\mathrm{nm}$, and at $612\,\mathrm{nm}$ under the excitation of $468\,\mathrm{nm}$ [82].

Some studies has been carried out with reports of triboluminescence in the $Sr_3Al_2O_6$:Eu,Dy [91, 92]. Different co-dopants has been studied suggesting that Pr^{3+} [93] or Sm^{3+} [94] might enhance luminescence properties. $Sr_3Al_2O_6$:Pr^{3+} system has been reported as potential to be used in UV dosimetry [78]. Also cerium-doped $Sr_3Al_2O_6$ has been reported with emission at around $460\,\mathrm{nm}$ [95], however other study reports emission of same system at $536\,\mathrm{nm}$ [96]. Conflicting results show that more detail research is needed.

1.1.3 $SrAl_{12}O_{19}$

The structure of $SrAl_{12}O_{19}$ was first examined in 1938 by Adelsköld and found to be isomorphic with magnetoplumbite ($PbFe_{12}O_{19}$) [97]. The structure was refined by Lindop *et al.* in 1975 [98]. Later, the "anomalous" tetrahedral Al site was noticed and it was suggested that the coordination (Figure 1.5) of this site is trigonal bipiramidal [99]. This structure was confirmed by another single crystal X-ray diffraction study [100] as well by ^{27}Al NMR study [101]. Moreover, a recent neutron diffraction study reports on finding a "minor" hexagonal phase of close structure [102].

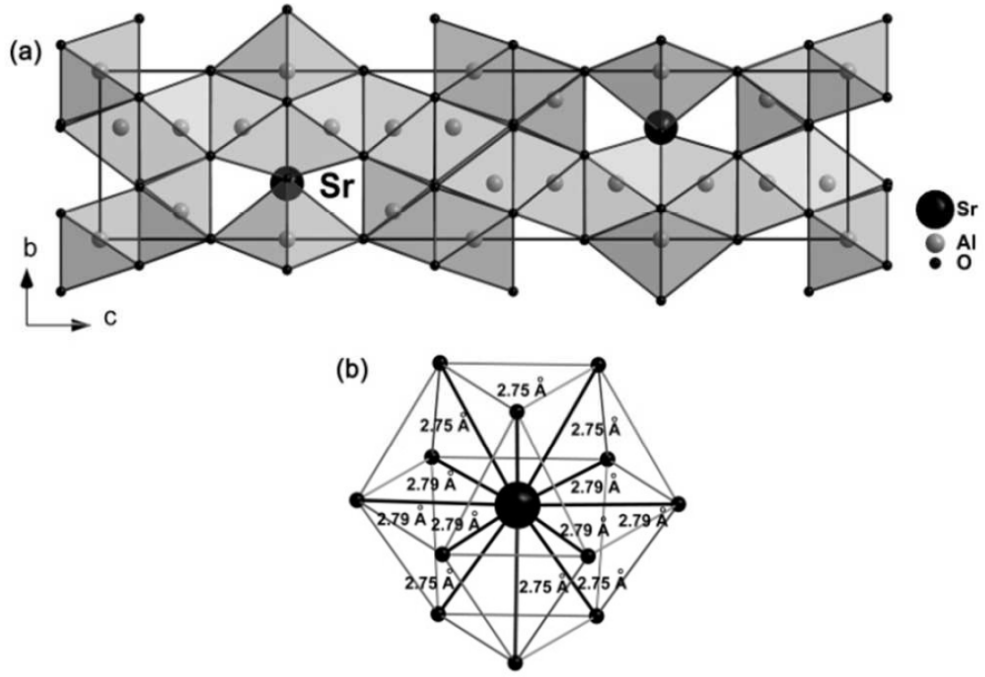

Figure 1.5. (a) Unit cell of $SrAl_{12}O_{19}$ along the a-axis, (b) Local coordination geometry of Sr^{2+} [37].

$SrAl_{12}O_{19}$ has a hexagonal structure of magnetoplumbite with space group $P6_3/mmc$ (№ 194) and cell parameters $a = 5.5666$ and $c = 22.0018$ Å [100]. The unit cell (shown in figure 1.5) is built of two spinel-like blocks containing usual IV-fold and VI-fold Al^{3+} coordinated cations separated by mirror planes which contain Sr^{2+} and Al^{3+} cations. The interspinel layers have rather unusual V-fold sites for smaller (Al^{3+}) cations and also provide XII-fold sites to accommodate large cations of $\sim$1.15 to 1.84 Å radius (for example Sr^{2+} or Eu^{2+}) [103].

Reported synthesis routes for the $SrAl_{12}O_{19}$ include solid state synthesis [104], floating zone technique [105], Czochralski single crystal growth method [98], combustion process [106], laser heated pedestal growth technique [107], sol-gel route [108] and spray-drying technique [109] [101].

Various dopants have been incorporated in $SrAl_{12}O_{19}$ host lattice. Nd^{3+} dopant has been used as potential activator for laser applications [105, 110, 111]. Er^{3+} doped system has also been examined [112, 113]. $SrAl_{12}O_{19}$:Mn^{4+} system has been offered as red phosphor for white LED applications [114] while Sm^{3+}-doped $SrAl_{12}O_{19}$ was successfully used for red laser operation [115]. One of the most popular dopants is europium. If it is in reduced form of Eu^{2+} than the emission is broad peak at around 395 nm [37, 116, 117, 118, 119], while Eu^{3+}, unsurprisingly, result in sharp emission lines in the range of 590–710 nm [120].

When co-doped with cerium, the energy transfer from Ce^{3+} to Eu^{2+} has been observed [106], while co-doped with chromium, the energy transfer from Eu^{2+} to Cr^{3+} is reported [121].

Unlike other strontium aluminates, the most studied dopant in $SrAl_{12}O_{19}$ is praseodymium. Since coordination number of Sr site is quite high, it results in low crystal field strength on Pr^{3+} [122]. Quantum efficiencies measured for $SrAl_{12}O_{19}$:Pr^{3+} (usually, Mg^{+} is used for charge compensation) are close to unity [123], but moreover, it was observed that in such system photon cascade emission (or quantum splitting) occurs [107, 124, 125, 126]. A mechanism involving valence hole trapping and energy transfer from excitonic states to Pr^{3+} was proposed [127]. New studies are still being performed for Pr doped $SrAl_{12}O_{19}$ system used in laser operation [128, 129, 130, 131].

1.1.4 $Sr_4Al_{14}O_{25}$

Unlike previously described phases, the documented studies on the structure of $Sr_4Al_{14}O_{25}$ are relatively new – first report on structural research is from 1976 [132]. Refined structural data was published by Wang *et al.* in 1999 [133]. Additionally, the local structure was characterized by ^{27}Al NMR technique [134]. Since the discovery of persistent luminescence in Eu^{2+} doped and Dy^{3+} co-doped $Sr_4Al_{14}O_{25}$ [135], studies with the goal of improvement of afterglow properties are still carried out [136, 137].

The crystal structure of $Sr_4Al_{14}O_{25}$ has been determined as a orthorhombic $Pmma$ (№ 51) space group with $a = 24.7451$, $b = 8.4735$ and $c = 4.8808$ Å [133]. The structure consists of layers made up of AlO_6 octahedra chains interconnected by a double layer of AlO_4 tetrahedra chains (Figure 1.6) [134]. The octahedra are connected together by sharing one edge, whereas the tetrahedra are connected by corner sharing, two by two or three by three, resulting in the presence of tricoordinated oxygen atoms and tetrahedra triclusters. There are six different crystallographic sites for the aluminum atoms in the structure: three AlO_6 octahedral sites and three AlO_4 tetrahedral sites. Also there are two different strontium sites with coordination numbers 10 and 7 (Figure 1.6(b)) [37].

Capron *et al.* showed that this phase forms at $1134\,^{\circ}\mathrm{C}$ and is stable up to $1500\,^{\circ}\mathrm{C}$ [134] (Figure 1.7). The whole process of formation-decomposition was summarized:

1) $923\,^{\circ}\mathrm{C}$, crystallization into $SrAl_2O_4$ (hexagonal) and γ-Al_2O_3 solid solu-

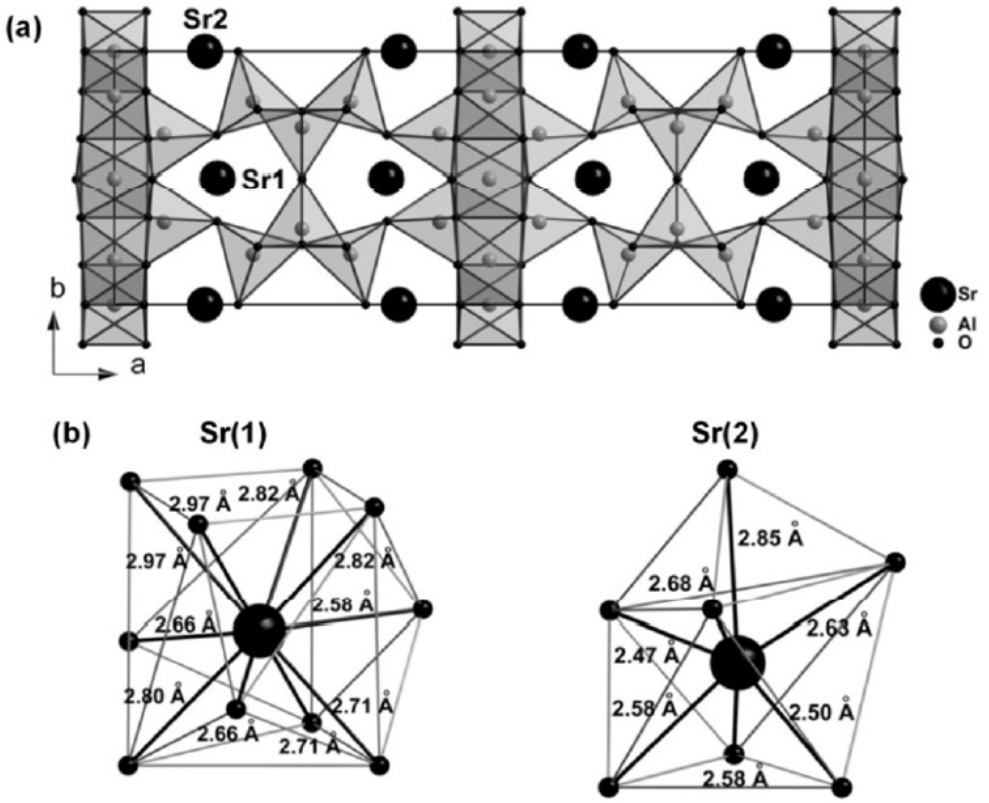

Figure 1.6. (a) Unit cell of $Sr_4Al_{14}O_{25}$ along the c-axis, (b) Local coordination geometry environment of nonequivalent Sr^{2+} sites [37].

tions;

2) $1134\,^{\circ}\mathrm{C}$, formation of $Sr_4Al_{14}O_{25}$ by combination of two solid solutions;

3) up to $1500\,^{\circ}\mathrm{C}$, $Sr_4Al_{14}O_{25}$ is stable;

4) $1600\,^{\circ}\mathrm{C}$, decomposition into $SrAl_2O_4$ and $SrAl_4O_7$.

It is reported that a single-phase compound of $Sr_4Al_{14}O_{25}$ is very difficult to obtain without flux [138]. Nagamani *et al.* claims, that several flux materials such as calcium fluoride (CaF_2), ammonium chloride (NH_4Cl), ammonium fluoride (NH_4F), and boric acid (H_3BO_3) results in formation of the single-phase $Sr_4Al_{14}O_{25}$ compound in all the samples, but boric acid gives maximum photoluminescence emission [138]. Reported hydrothermal [132, 139], solid-state [29], spray-drying [134], sol-gel [140], combustion [141], spark plasma [142] and microemulsion [47] synthesis routes of $Sr_4Al_{14}O_{25}$.

$Sr_4Al_{14}O_{25}$:Eu^{2+},Dy^{3+} is another (in addition to $SrAl_2O_4$:Eu^{2+},Dy^{3+}) strontium aluminate that is widely used and has gained commercial success [10].

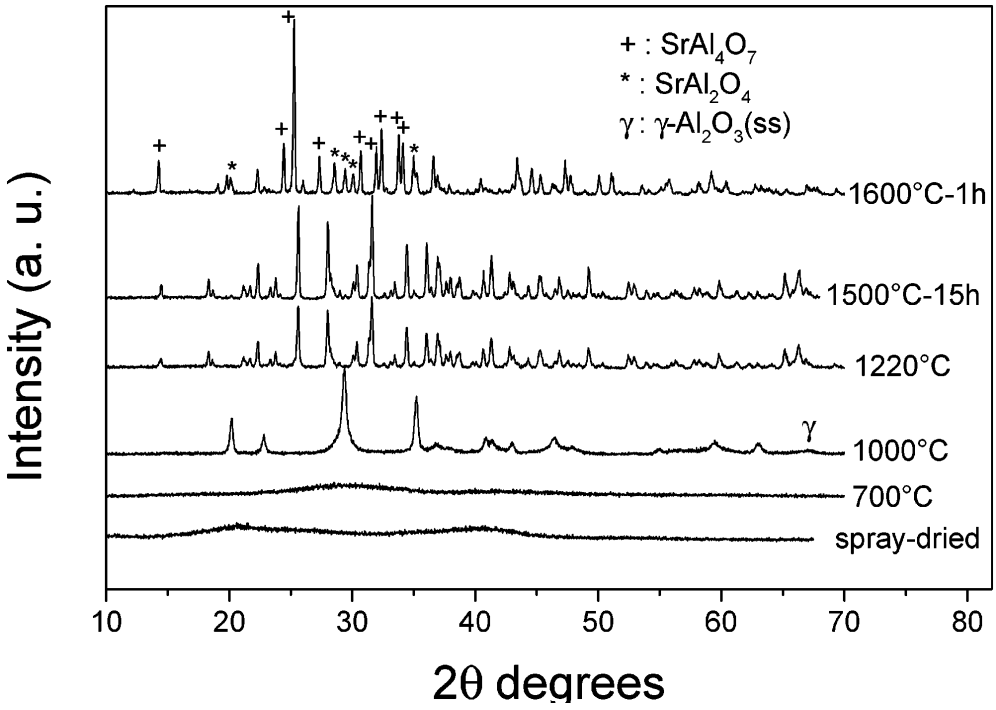

Figure 1.7. XRD patterns showing the formation of $Sr_4Al_{14}O_{25}$ phase via $SrAl_2O_4$ and γ-Al_2O_3 solid solutions and its decomposition at higher temperature [126].

Research on $Sr_4Al_{14}O_{25}$ as a host matrix for luminescent materials started in late 1980s [29], but escalated after work by Lin *et al.* who showed that Eu^{2+} and Dy^{3+}-doped $Sr_4Al_{14}O_{25}$ is blue ($\sim 490\,\mathrm{nm}$) emitting persistent luminescent material with afterglow times reaching $20\,\mathrm{h}$[135, 8]. Since then a lot of effort has been taken in order to improve luminescence properties, for example by using different synthesis routes [140, 141, 142, 143, 144, 145, 146, 147, 148, 149], varying composition [150, 151, 152, 153], adding co-dopants [154, 155] or using charge-compensation [137]. Other dopants used in $Sr_4Al_{14}O_{25}$ host include cerium [156, 157, 158], samarium [159, 160] and manganese [161, 162, 163].

1.1.5 $SrAl_4O_7$

A few publications on $SrAl_4O_7$ phase is published so far. The structure was first described in 1937 [68] and later refined in 1972 [164]. Moreover, high-pressure phase (called β-$SrAl_4O_7$) was discovered and described by Machida *et al.* [165]. At a usual heating rate of $5\,^{\circ}\mathrm{C/min}$ $Sr_4Al_{14}O_{25}$ is easily formed at 1100–$1150\,^{\circ}\mathrm{C}$, however, it is decomposed at temperatures higher than $1500\,^{\circ}\mathrm{C}$ [5]. On the other hand $SrAl_4O_7$, having a slow kinetics of formation, may be crystallized directly at 900–$1000\,^{\circ}\mathrm{C}$ by slow heating [18].

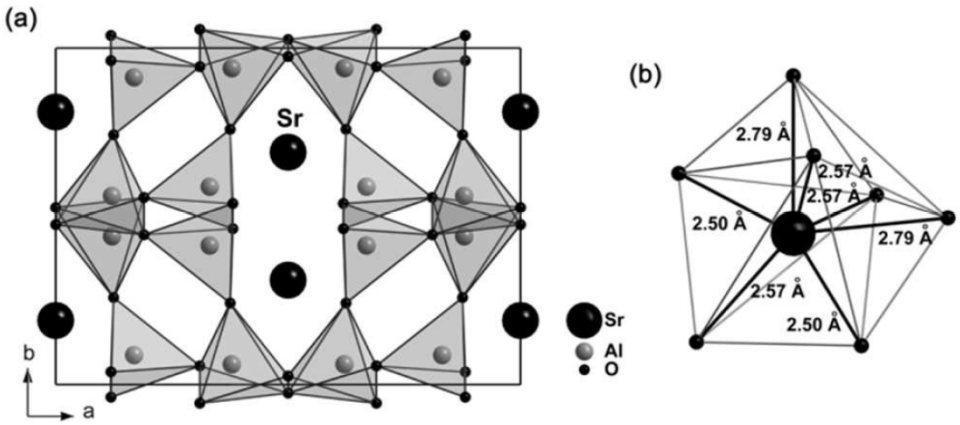

Figure 1.8. (a) Unit cell of $SrAl_4O_7$ along the c-axis, (b) Local coordination geometry environment of Sr^{2+} [37].

The $SrAl_4O_7$ has a monoclinic crystal structure with space group $C12/c1$ (№ 15) and unit cell parameters $a = 13.0389$, $b = 9.0113$, $c = 5.5358\,\text{Å}$ and $\beta = 106.12°$ [164]. The lattice consists of corner sharing AlO_4 tetrahedra and strontium ions occupying one possible crystallographic site (Figure 1.8).

Synthesis routes used for the preparation of $SrAl_4O_7$ include solidification from high-temperature liquid state [68], Czochralski [164], floating-zone [74], laser-heated pedestal growth [166], spray-drying [18], combustion [167, 168, 169], sol-gel [76, 170], solvothermal [171] techniques. It should be noted, that conventional solid-state synthesis route, to our knowledge, has not been reported for this phase and is claimed that such attempts result in a mixture of phases [18, 37].

$SrAl_4O_7$ as a host for Eu^{2+} shows broad emission band peaking somewhere between 470 and $510\,\text{nm}$ [37, 74, 167, 169, 172, 173, 174, 175]. The afterglow times are a bit contradictory ranging from several minutes [172, 176] to more than $1\,\text{h}$ [74] for Eu^{2+} co-doped samples, and from milliseconds [167] to few minutes [172] only for Eu^{2+} doped specimens. Such results indicates that more investigation of this system is required.

Additionally, other activators has been incorporated in $SrAl_4O_7$ host. Pr^{3+} doped system showed the emission profile usual to praseodymium, but quantum efficiencies achieved were less than $10\,\%$ [166, 177]. Study on $SrAl_4O_7$:Tm/Yb system revealed that it is capable to undergo downconversion as well as upconversion depending on the excitation wavelength [168]. Copper doped aluminate is claimed to exhibit bright-green luminescence and might be suitable for LED

applications [178]. Also, Dy^{3+} doped system has been studied and emission peaks at 395, 510 and $800\,\mathrm{nm}$ has been observed [179, 180]. Another study has found bright orange red emission at $598\,\mathrm{nm}$ in the $SrAl_4O_7:Sm^{3+}$ system [181]. A study on $SrAl_4O_7:Pb^{2+}$ and $SrAl_4O_7:Ce^{3+}$ systems revealed emissions at 313 and $331\,\mathrm{nm}$, respectively [182].

1.2 Inorganic phosphors

The strontium aluminates are known as persistent inorganic phosphors. In the current chapter, the fundamental introduction to the phenomenon of luminescence concentrating on photoluminescence and persistent luminescence will be given.

1.2.1 Luminescence

In general, *luminescence* is emission of light by a substance, as a result of radiative transition from excited to ground (relaxed) state. Thus, it can be considered a cold-body radiation, as opposed to *incandescence* which is a case of thermal radiation – emission of electromagnetic waves from matter due to conversion of thermal energy (kinetic energy of particles in matter) to electromagnetic energy.

The process of luminescence begins with excitation – absorption of energy which raises luminescent center from relaxed to excited state. Luminescence is usually divided in to different types depending on how it was excited:

- *chemiluminescence* – excitation results from chemical reaction (or in the case of *electrochemiluminescence* – from electrochemical reaction);
- *bioluminescence* – from biochemical reactions in living organism;
- *electroluminescence* – from electric current passing through the substance;
- *cathodoluminescence* – from interaction with electron beam;
- *radioluminescence* – from interaction with ionizing radiation;
- *mechanoluminescence* – from mechanical action on material. It can be divided to subtypes of *triboluminescence* (when that material is scratched,

crushed, or rubbed), *fractoluminescence* (when it is fractured), *piezoluminescence* (when pressure is applied) and *sonoluminescence* (interaction with sound waves);

- *photoluminescence* – excitation results from absorption of photons;
- *thermoluminescence* – a special type of luminescence, when previously absorbed energy is re-emitted as light upon heating of the material (the phenomenon is distinct from that of black body radiation).

The following step in the process of luminescence is relaxation – return from excited state to ground state by emission of radiation. Not every ion and material shows luminescence, because there are two possibilities to return from excited state – via radiative process or non-radiative process (the energy of the excited state is used to excite the vibrations of the substance, i.e. to heat it). In order to create efficient luminescent materials it is necessary to suppress this non-radiative process [1].

In general, material that exhibits the phenomenon of luminescence is called *phosphor* (not to be confused with the chemical element phosphorus). In the case of inorganic phosphors, the system consists of a *host* matrix and a luminescent center, often called an *activator*. Usually, activator is an ion, but in some cases crystal defects can play the role of luminescence center.

1.2.2 Photoluminescence

Photoluminescence is, quite often, divided to fluorescence and phosphorescence. *Fluorescence* is luminescence which occurs essentially only during the irradiation of a substance by electromagnetic radiation, while the term *phosphorescence* is used to describe long-lived luminescence [183]. The decay times associated are "fast" (10^{-9} to 10^{-3} s) and "slow" (10^{-3} to 100 s), respectively [184]. And the mechanisms involved are quantum-mechanically allowed for fluorescence and quantum-mechanically forbidden (involving change in spin multiplicity, typically from triplet to singlet or vice versa [183]) for phosphorescence [1].

The term fluorescence was coined in 1852, when it was experimentally demonstrated that certain substances absorb light of a narrow spectral region (e.g., blue light) and instantaneously emit light in another spectral region not present in the incident light (e.g., yellow light) and that this emission ceases at once when the irradiation of the material comes to the end. The name fluorescence was derived

from the mineral fluorspar, which exhibits a violet short-duration luminescence on irradiation by ultraviolet light [185].

The term phosphorescence originally derives from chemical element phosphorus, which emits a faint glow (white phosphorus allotrope), although later it was realized that white phosphorus glows because the oxidation reaction occurs (chemiluminescence) and not photoluminescence process [186].

The segregation of photoluminescence to fluorescence and phosphorescence according to spin-allowed and spin-forbidden transition might be true with organic molecules, but in case of inorganic phosphors it is much more complex [1]. For example, in $CaAl_2O_4$:Ce^{3+} emission occurs due $5f \Longrightarrow 4d$ transition, which is allowed, so it should be fluorescence with short emission time, but actually such system exhibit afterglow time up to $10\,\mathrm{h}$ [187]. To avoid such confusions it was proposed to use a single term ***luminescence*** instead of – usually theoretically inaccurate – fluorescence and phosphorescence [188] although some confusion in terminology still exist.

Mechanisms of photoluminescence

In many cases, the process of photoluminescence is not as simple as absorption and emission of an activator (figure 1.9 a). For example, another ion (called *sensitizer*) can absorb energy and become excited and then transfer this energy to the activator (such process is called *energy transfer*, as shown in figure 1.9 b). A special case of energy transfer is *cross-relaxation* (Fig. 1.9 c), where the original system loses the energy by obtaining the lower state A_2^* (which may also be the ground state) and another system acquires the energy by going to a higher state $A_2'^*$. Cross-relaxation may take place between the same ion (being a major mechanism for quenching at higher concentration in a given material) or between two differing elements, which happen to have two pairs of energy levels separated by the same amount [189].

When relaxation from excited state occurs through several steps (of which more than one is radiative transition) multiple photons of lower energy get emitted (Fig. 1.9 d) through a process called *quantum splitting*. Such process enables luminescence center to yield efficiency more than $100\,\%$ (for example, if one photon is absorbed and two photons are emitted). Opposite process is *upconversion* – when more than one photon gets absorbed and one photon with higher energy is released (Fig. 1.9 e).

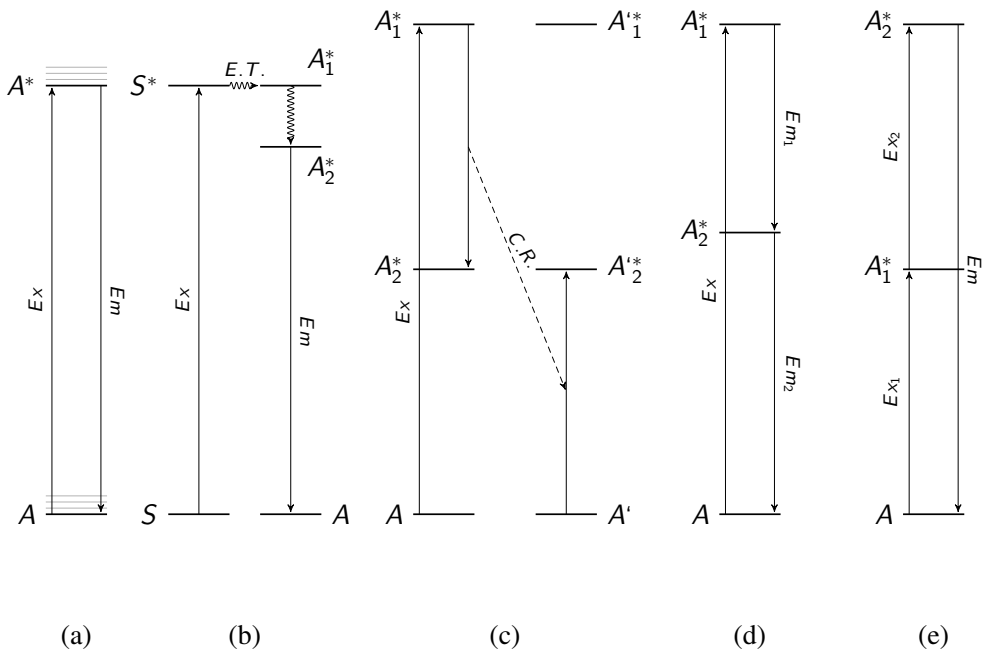

Figure 1.9. Simplified representation of some photoluminescence mechanisms. a) Excitation and emission of activator; b) energy transfer; c) cross-relaxation; d) downconversion; e) upconversion. A denotes activator energy levels (black horizontal lines), S – sensitizer, Ex – excitation energy transition (straight arrow – radiative transition), Em – emission, $E.T.$ – energy transfer (squiggly arrow – non-radiative transition), $C.R.$ – cross-relaxation, asterix ($*$) indicates excited state.

1.2.3 Persistent luminescence

A special case of luminescence is called *persistent luminescence*, and it can be defined as emission obtained after the removal of an excitation source. In scientific literature the phenomenon is also called phosphorescence, afterglow, or LLP (short for Long Lasting Phosphorescence) [13]. The terminology sometimes can be confusing and the usage of a single term – persistent luminescence has been suggested [10].

The property of conserving light has been known for millennium, as there are some records about paintings which remained visible during the night. The better documented case is the "Bologna stone" discovered in the 17^{th} century by an alchemist [13, 10]. Recently, it was showed, that the afterglow in Bologna stone originated from Cu^{+} impurities in BaS [190].

During the 20^{th} century ZnS (doped with copper and later co-doped with cobalt) was the most widely used persistent phosphor, and several other sulphides were well known. Most famous products include luminous watch dials, paint and glow-in-dark toys. But the extreme sensitivity to the moisture and the

fact, that large concentrations of phosphors are required to yield sufficient light, meant limited interest in such materials [13, 10].

In 1996 Matsuzawa *et al.* published an article on $SrAl_2O_4$:Eu^{2+},Dy^{3+} persistent phosphor capable of emitting light up to 10 h after excitation light source has been removed [11]. Soon another system of $CaAl_2O_4$:Eu^{2+},Nd^{3+} was described [191]. Few years later a new silicate based persistent luminescent material $Sr_2MgSi_2O_7$:Eu^{2+},Dy^{3+} was discovered [192] and then followed $Sr_4Al_{14}O_{25}$ doped with Eu^{2+} and Dy^{3+} [135]. Since then a vast variety of persistent luminescent materials has been reported with different emission wavelengths and afterglow durations. These persistent phosphors can be divided by an activator ion (mostly Eu^{2+} based materials [13], but also other activators exist, including Ce^{3+}, Tb^{3+}, Pr^{3+}, Dy^{3+}, Mn^{2+}, Cr^{3+}, Cu^{+} and other [14]), or by host material, with largest groups being aluminates and silicates also including smaller groups of sulfides, phosphates and nitrides [9].

The field of persistent luminescence is being more and more studied. However, many questions and problems related to the topic are still open. One of the major uncertainties is the exact mechanism of the phenomenon (which will be discussed later). Another problem is the lack of persistent luminescent materials emitting in longer wavelengths, which is mainly caused by two reasons: 1) it is difficult to obtain large enough crystal field in oxides to shift emission of Eu^{2+} to the red region of the visible spectrum (or by using other hosts/activators, stability is lost); 2) the sensitivity of human eye for red light is much weaker than for green or even blue, so the intensity of emission has to be much higher [13, 10, 14].

Mechanism of persistent luminescence

When Matsuzawa *et al.* published his article on $SrAl_2O_4$:Eu^{2+},Dy^{3+}, the possible mechanism of the process was also suggested [11]. The proposed model quickly became popular and was used (and sometimes, still is used) to explain afterglow in newly discovered compounds, although there was lack of evidence to confirm such model and it involves highly improbable Eu^{+} species (formation would require huge amounts of energy) [10]. Later, in 2003 Aitasalo *et al.* suggested new model, based on excitation of host material and energy transfer to europium [193]. Dorenbos was not convinced of such models and in 2005 has presented modified version of Matsuzawa's mechanism, without requiring exis-

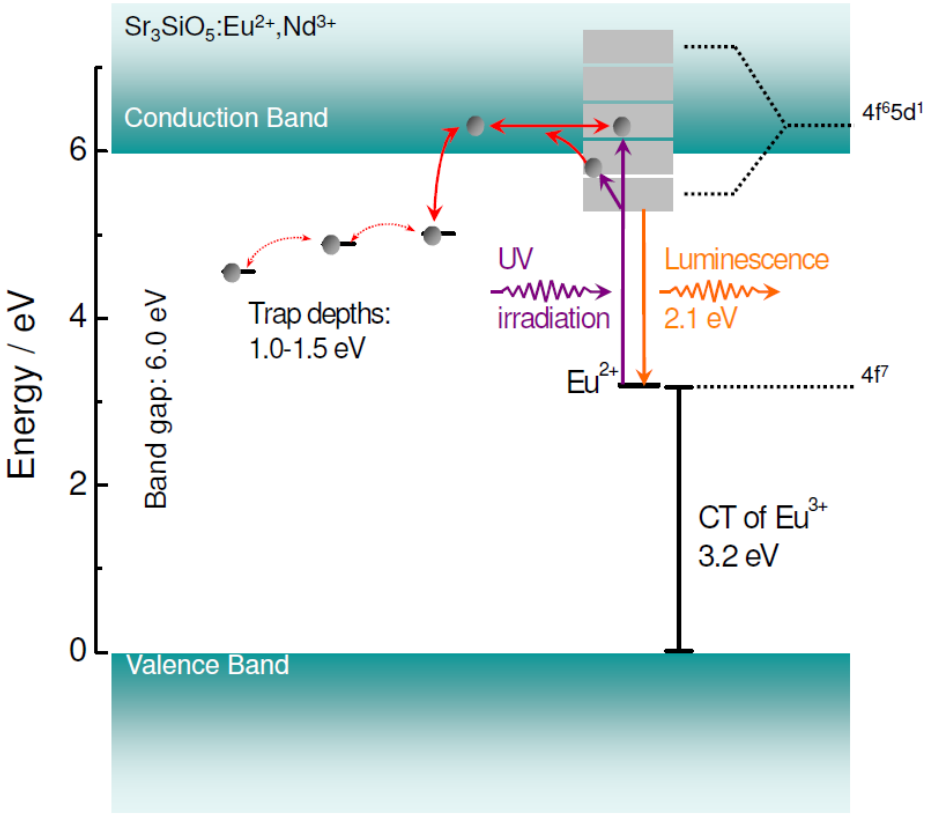

Figure 1.10. The model mechanism of persistent luminescence for the Eu^{2+} doped materials: $Sr_3SiO_5:Eu^{2+},Nd^{3+}$ [200].

tence of Eu^{+} [194], although it is incapable to explain persistent luminescence in non-co-doped meterials. Around the same time similar mechanism was proposed by Clabau *et al.* but differing by two important aspects: 1) transport of electrons between the traps and the luminescent centers happens through direct transfer, not by migration through conduction band; 2) the nature of the traps is oxygen vacancies, but not codopant ions [12]. In 2006, Aitasalo *et al.* combined suggestions from Dorenbos and Clabau models and described new model, but the exact nature of the traps was not specified [195].

The exact mechanisms governing persistent luminescence in materials have yet to be clarified [13]. An example of the model mechanism is given in figure 1.10. Although the mechanism is convincing, it lacks explanation on exact nature of the traps and also it is not entirely quantitative since the energies of the processes are only estimates because the values are based on data consisting of broad band emission, excitation and absorption [10]. However, this model has been used to describe persistent luminescence of Tb^{3+} [196, 197], Ti^{3+} [198], Cr^{3+} [199] and Cu^{+} [190].

The process starts with excitation of an electron from the $4f^7(^8S_{7/2})$ ground state to the excited $4f^65d^1(^2D)$ states of Eu^{2+}. Due to the proximity of the host's conduction band, some electrons can easily escape from the excited $4f^65d^1$ levels, directly or aided by thermal energy (kT), to the conduction band of Sr_3SiO_5. The relatively long lifetime of the $4f^65d^1(2D) \Longrightarrow 4f^7(^8S_{7/2})$ emission of Eu^{2+} ($\sim 1\,\mu s$) facilitates this charge transfer. The electrons then move further quite freely in the conduction band until they meet a defect and are trapped. The reverse process is initiated by the absorption of thermal energy allowing the trapped electrons to escape back to the conduction band and populate the $4f^65d^1(^2D)$ levels of Eu^{2+} (partially overlapping conduction band of Sr_3SiO_5). The non-radiative (within the $4f^65d^1$ states) and finally the radiative relaxation of Eu^{2+} (from the lowest $4f^65d^1$ state) takes care of producing the persistent luminescence. Alternatively, retrapping of the electrons can occur in every step of the process still lengthening the persistent luminescence [10].

The band gap value (for Sr_3SiO_5:Eu^{2+}: $6.0\,eV$) is easily found from the synchrotron (or other VUV) excitation spectrum of Eu^{2+}, as well as is the charge (electron) transfer ($e^-[O(2\,p)] + Eu^{3+} \longrightarrow Eu^{2+}$) transition energy ($3.2\,eV$) from the excitation spectrum of Eu^{3+}, used to estimate the Eu^{2+} $^8S_{7/2}$ ground state position. The excitation and emission energies can be obtained from the elementary photoluminescence studies. Finally, the trap energies are acquired from the straightforward deconvolution of the thermoluminescence glow curves [10].

1.3 Rietveld refinement

Rietveld refinement method as a tool for precise analysis of X-ray diffraction (XRD) measurement data was used in this work. Current chapter will provide brief introduction to this method. In 1969, Hugo Rietveld suggested method of profile fitting for nuclear and magnetic structures. This method does not use integrated intensities, but directly employs the profile intensities obtained from step-scanning measurements of the powder diagram [201, 202]. Full profile refinement is computationally intense and employs the nonlinear least squares method, which requires a reasonable initial approximation of many free variables. Some unknowns, like background, scale factor, etc. may be simply guessed at the beginning and then effectively refined as the least squares fit converges to a global minimum [203].

1.3.1 Origin of the powder diffraction patterns

XRD analysis is relatively simple and powerful tool suitable for the characterization of crystalline materials. Crystalline materials can be defined as being in solid state of matter and having atoms or molecules arranged in (theoretically infinitely) regular, periodic manner. Such periodic structure of crystalline materials when illuminated by electromagnetic radiation (of wavelength similar to interplanar distances, i.e. X-ray radiation) causes elastic scattering and (since the structure is periodically regular) diffraction is observed. In powder XRD measurements typically intensity as a function of an angle of diffracted beam is recorded producing diffraction pattern. A powder diffraction pattern can be considered as a set of discrete *diffraction peaks* superimposed over a continuous *background* [203]. The diffraction peaks may be described by the following components: *position*, *intensity* and *shape*.

Position of peaks in powder diffraction patterns

Position of a peak in diffraction pattern can be described by Bragg's law:

$$2d \sin\theta = n\lambda \tag{1.1}$$

where d is interplanar distance between crystallographic planes, θ is the scattering angle, n is a positive integer and λ is the wavelength of incident wave [204].

The unit cell dimensions and the wavelength are the two major factors that determine Bragg angles for the same combination of Miller indices. But in reality, various instrumental and specimen features may affect the observed positions of Bragg peaks. These factors are often known as systematic aberrations (distortions), and they are usually assembled into a single correction parameter, $\Delta 2\theta$. For the most commonly used Bragg-Brentano focusing geometry $\Delta 2\theta$ consist of several factors, namely *axial divergence*, *in-plane divergence*, *effective linear absorption*, *specimen displacement* and *zero-shift error* [203].

Intensity of peaks in powder diffraction patterns

The measured profile of a single powder diffraction peak is dependent on the neutron or X-ray spectral distribution, the monochromator mosaic distribution, the transmission functions of the Soller slits, and the sample shape and crystallinity [201]. Considering all these factors, the integrated intensity in powder

diffraction can be expressed as:

$$I_{hkl} = K \times p_{hkl} \times L_\theta \times P_\theta \times A_\theta \times T_{hkl} \times E_{hkl} \times |F_{hkl}|^2 \qquad (1.2)$$

where

K the *scale factor*. It is a multiplier required to normalize experimentally observed integrated intensities with absolute calculated intensities. Scale factor is a constant for a given phase and it is determined by the number, spatial distribution and the states of the atoms in the unit cell;

p_{hkl} the *multiplicity factor*. It is number of symmetrically equivalent reflections;

L_θ the *Lorentz multiplier*, which is defined by the geometry of diffraction;

P_θ the *polarization factor*. It is a multiplier, which accounts for a partial polarization of the scattered electromagnetic wave;

A_θ the *absorption multiplier*, which accounts for absorption of both the incident and diffracted beams and nonzero porosity of the powdered specimen;

T_{hkl} the *preferred orientation factor*. It is a multiplier, which accounts for possible deviations from complete randomness in the distribution of grain orientations;

E_{hkl} the *extinction multiplier*, which accounts for deviations from kinematical diffraction model. In powders, these are quite small and the extinction factor is nearly always neglected;

F_{hkl} the *structure factor*, which is defined by the details of the crystal structure of the material: coordinates and types of atoms, their distribution among different lattice sites and thermal motion [203].

In Eq. (1.2) intensity for a given Bragg peak I_{hkl} is not an absolute maximum value of the peak, but actually an integrated area under the peak and can be determined from numerical integration as:

$$I_{hkl} = \sum_{i=1}^{j} \left(Y_i^{obs} - b_i \right) \qquad (1.3)$$

where I_{hkl} is integrated intensity of a peak, i is the total number of data points measured within the range of the peak, Y_i^{obs} is absolute value of intensity observed at point i and b_i is the background value at point i [203].

The structure factor, F_{hkl}, from equation (1.2) includes multiple contributions, which are determined by the distribution of atoms in the unit cell and other structural features and can be expressed as:

$$F_{hkl} = \sum_{i=1}^{n} g^j t^j(s) f^j(s) \exp[2\pi \mathrm{i}(hx^j + ky^j + lz^j)] \tag{1.4}$$

where

n the total number of atoms in the unit cell and it includes all symmetrically equivalent atoms;

s $\sin\theta_{hkl}/\lambda$

g^j the population (or occupation) factor of the jth atom ($g^j = 1$ for a fully occupied site);

t^j the temperature factor, which describes thermal motions of the jth atom;

$f^j(s)$ the atomic scattering factor describing interaction of the incident wave with a specific type of an atom as a function of $\sin\theta/\lambda$ for X-rays or electrons;

i $\mathrm{i} = \sqrt{-1}$;

h, k, l are the Miller indices and x^j, y^j, z^j are the coordinates of atoms in unit cell [203].

Shapes of peaks in powder diffraction patterns

Peaks in measured diffraction patterns are not narrow vertical bars of different intensities at given Bragg reflections (like in database), but are broadened and having specific shape. The observed peak shapes are best described by the so-called peak-shape function (PSF), which is a convolution of three different functions: instrumental broadening, Ω, wavelength dispersion, Λ, and specimen function, Ψ. Thus, PSF can be represented as follows:

$$PSF(\theta) = \Omega(\theta) \otimes \Lambda(\theta) \otimes \Psi(\theta) + b(\theta) \tag{1.5}$$

where b is the background function.

In general, three different approaches to the description of peak shapes can be used:

1) *empirical* peak-shape functions, which fit the profile without attempting to associate their parameters with physical quantities;

2) *semi-empirical approach* that describes instrumental and wavelength dispersion functions using empirical functions, while specimen properties are modeled using realistic physical parameters;

3) *fundamental parameters* approach, all three components of the peak-shape function (1.5) are modeled using rational physical quantities [205].

Fundamental parameters approach synthesizes line shape of a peak using precise initial parameters such as receiving-slit width, the receiving-slit length, the X-ray source size, the angle of divergence of the incident beam, the X-ray attenuation coefficient of the specimen and the crystallite size [205]. Such calculations are computationally intense, but with increasing available power of personal computers, this method is becoming more popular.

Nevertheless, empirical approach to fit peak-shapes is probably most commonly used, and the used functions are Gaussian, Lorentzian and pseudo-Voigt.

Gaussian function:

$$y(x) = G(x) = \frac{2}{H}\sqrt{\frac{\ln 2}{\pi}}\exp\left(-\frac{4\ln 2}{H^2}x^2\right) \tag{1.6}$$

where H is full width of a peak at its half maximum (FWHM).

Lorentzian function:

$$y(x) = L(x) = \frac{\frac{2}{\pi H}}{1+\frac{4}{H^2}x^2} \tag{1.7}$$

And the pseudo-Voigt function:

$$y(x) = pV(x) = \eta L(x) + (1-\eta)G(x) \tag{1.8}$$

where η is the $pV(x)$ function mixing parameter (fractional contribution of function into mixture of two functions, $0 < \eta < 1$). Pseudo-Voigt function is the linear combination of Lorentzian and Gaussian of the same FWHM, so there are two parameters characterizing the peak shape: $pV(x) = pV(x, \eta, H)$ [206].

Besides, more functions or modifications of previously mentioned functions exist, such like Pearson-VII [207], Thompson-Cox-Hastings modified pseudo-Voigt function [208] and other. More information from such improved functions can be extracted, like crystallite size and microstrain [203].

The peak broadening (H or FWHM) as a function of angle θ is described so-called Caglioti formula [209]:

$$H = \sqrt{U \tan^2 \theta + V \tan \theta + W} \tag{1.9}$$

where U, V and W are the free variables.

Background in powder diffraction patterns

Background is unavoidable in powder diffraction and each pattern has a different background level, which originates from inelastic scattering, scattering from air, sample holder and particle surfaces, X-ray fluorescence, incomplete monochromatization, detector noise, etc [203]. In order to successfully carry out precise analysis, background should always be accounted for.

During structural analysis the background can be handled manually (user selects points where definitely there are no Bragg peaks) or automatically (mathematical functions are used to approximate background). Manual selection of background is slower, but generally yields a more accurate background approximation [203]. However mathematic algorithm is much faster and easier thus functions like polynomial function (or modified versions, like Chebyshev polynomial) are commonly used:

$$b_i = \sum_{m=0 or -1}^{N} B_m (2\theta_i)^m \tag{1.10}$$

where B_m, are background parameters that can be refined and N is the order of the polynomial.

1.3.2 Structural refinement

In order to perform structural refinement, at least approximate structure of material should be known. How to deal with totally unknown crystal structures is beyond the subject of this review.

As seen from previous sections, diffraction patterns can be "synthesized" relatively easily. Assuming that you have known crystal structure, all the crystallographic planes with distances between (d-spacing) them can be calculated. Having known d-spacing it is easy to tell where the peak in the pattern will be from Bragg's law (equation (1.1)). Employing equation (1.2) relative intensities of these peaks can be estimated. Then the peak broadening can be achieved using one of the peak shape functions. And finally, add some background and you have a diffraction pattern similar to measured one. Comparing the measured and calculated patterns and achieving best fit by adjusting starting model of crystal structure allows precise crystallographic parameters to be determined.

The commonly used methods of full pattern decomposition include Pawley [210], Le Bail [211] and Rietveld [201, 202] methods. The main difference in these methods is how the values of integrated intensities are treated – as free least squares variables (Pawley), determined iteratively after each refinement cycle (Le Bail) or included into all calculations as functions of relevant geometrical, specimen and structural parameters (Rietveld) [203].

The main idea of Rietveld method is that experimental powder diffraction data are utilized without extraction of the individual integrated intensities and all structural and instrumental parameters are refined by fitting a calculated profile to the observed data [203]. Fitting is performed using nonlinear least squares minimization of the differences between the calculated and measured patterns.

The simplest form of the function minimized in the Rietveld method is:

$$M = \sum_{i=1}^{n} w_i \left(Y_i^{obs} - Y_i^{calc}\right)^2 \tag{1.11}$$

Taking into account multiple Bragg reflection overlaps and dual wavelength ($K\alpha_1 + K\alpha_2$), the expanded form of equation (1.11) becomes:

$$M = \sum_{i=1}^{n} w_i \left(Y_i^{obs} - \left[b_i + K \sum_{j=1}^{m} I_j \left\{y_j(x_j) + 0.5y_j + \Delta x_j\right\}\right]\right)^2 \tag{1.12}$$

where b_i is the background at the ith data point, K is the phase scale factor, m is the number of Bragg reflections contributing to the intensity of the ith data point, I_j is the integrated intensity of the jth Bragg reflection, $y_j(x_j)$ is the peak-shape function, Δx_j is the difference in positions of $K\alpha_1$ and $K\alpha_2$ components in the doublet, $x_j = 2\theta_j^{calc} - 2\theta_i$ and w_i is the weight assigned to the ith data point.

In the absence of a background and assuming that the measured intensity is only affected by statistical errors, the weight can be given as:

$$w_i = \left[Y_i^{obs}\right]^{-1} \tag{1.13}$$

In practice, the weight is usually calculated without subtracting the background, which yet again emphasizes the importance to have it at practical minimum [201, 202, 203, 206].

Sequence of the refinement

The parameters to be refined are usually selected by the user. Automatic computer algorithms exist, but grate care should be taken when using such since the outcome might be far from realistic. Moreover, refining all parameters at once also might lead to trouble due to the complexity of the problem and many possibilities for an out-of-control least squares.

One of the most common problems encountered during refinement (not including software related problems like crashing program) is converging to false minimum. When minimizing the function like in equation (1.11), several minima might exist and obtained answer might be not the global minimum (see figure 1.11).

To avoid such case (or reduce the risk), it is recommended to vary the starting model in significant ways and see if the same minimum is reached [212]. Also, the refinable parameters should be "swiched-on" in sequence, which depends on many variables, such as data quality, accuracy of the starting model, knowledge of instrumental contributions, etc. Here the experience of the crystallographer steps in. However, "textbook" guidelines of the sequence are as follows [212]:

- scale factor;
- specimen displacement or zero shift error;
- linear background (first background parameter);
- crystal lattice parameters;
- more background parameters;
- W parameter of the FWHM (see equation (1.9));

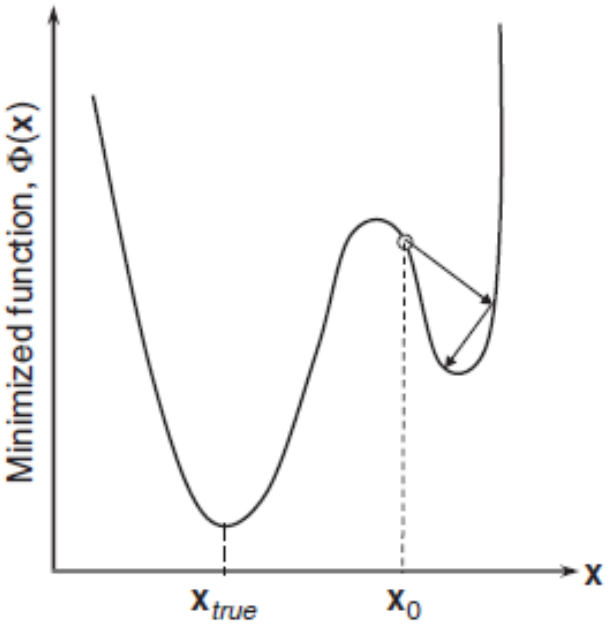

Figure 1.11. Nonlinear least squares minimization, when the initial approximation (x_0) is located near a false minimum. The arrows represent the possible outcomes of two least squares cycles and x_{true} marks true solution (global minimum) [203].

- atomic coordinates x, y, z;
- preferred orientation;
- population (site occupancies) and isotropic displacement (B) parameters;
- other peak shape parameters (like U and V);
- anisotropic displacements.

Quality of the refinement

While solving the crystal structure using Rietveld (or other) method you always end up with the answer, but you can never be certain if this answer is correct. To assess the obtained results, first of all the refined parameters should be verified if they make physical sense. Another important factor is how well calculated pattern fits experimental results. The quality of the fit is quantified using various figures of merit, but none of them is a substitute for the plots of calculated and measured diffraction patterns plotted using the same scale and supplemented with the difference (observed minus calculated intensities) plot.

Nevertheless, statistical figures of merit are provided with the refinement data and the most common of them are profile residual, R_p, weighted profile residual R_{wp}, Bragg residual, R_B, expected residual R_{exp}, and goodness of fit, χ^2 (*chi-squared*).

The profile residual (or reliability) factor:

$$R_p = \frac{\sum_{i=1}^{n} \left| Y_i^{obs} - Y_i^{calc} \right|}{\sum_{i=1}^{n} Y_i^{obs}} \times 100\,\% \tag{1.14}$$

Weighted profile residual:

$$R_{wp} = \left[\frac{\sum_{i=1}^{n} w_i \left(Y_i^{obs} - Y_i^{calc} \right)^2}{\sum_{i=1}^{n} w_i \left(Y_i^{obs} \right)} \right]^{1/2} \times 100\,\% \tag{1.15}$$

Expected weight profile residual:

$$R_{exp} = \left[\frac{n-p}{\sum_{i=1}^{n} w_i \left(Y_i^{obs} \right)} \right]^{1/2} \times 100\,\% \tag{1.16}$$

Bragg residual:

$$R_B = \frac{\sum_{j=1}^{n} \left| I_j^{obs} - I_j^{calc} \right|}{\sum_{j=1}^{n} I_j^{obs}} \times 100\,\% \tag{1.17}$$

Goodness of fit (chi-squared):

$$\chi^2 = \frac{\sum_{i=1}^{n} w_i \left(Y_i^{obs} - Y_i^{calc} \right)^2}{n-p} = \left[\frac{R_{wp}}{R_{exp}} \right]^2 \tag{1.18}$$

In equations (1.14)–(1.18) (adapted from [203, 206]), the following notations have been used:

n the total number of points measured in the powder diffraction pattern;

Y_i^{obs} the observed intensity of the ith data point;

Y_i^{calc} the calculated intensity of the ith data point;

w_i the weight of the ith data point;

$n - p$ is the number of degrees of freedom, where p is the number of refined parameters;

I_j^{obs} the "observed" integrated intensity of the jth Bragg peak, which has been calculated after Y_i^{obs} have been partitioned according to the calculated intensities of the contributing Bragg peaks;

I_j^{calc} the calculated intensity of the jth Bragg peak.

As noted earlier, care should be taken when comparing residuals. The paradox is that the better quality of data the higher χ^2 or R_{wp} is obtained (refinement is "worse"), since larger dataset is more complicated to be fitted perfectly, even though the model obtained from that data should be of higher quality [213]. Thus, the most important way to determine the quality of a Rietveld fit is by viewing the observed and calculated patterns graphically and to ensure that the model is chemically plausible [213].

2 Experimental

2.1 Materials and reagents

The used materials were strontium nitrate, $Sr(NO_3)_2$ (99 %, Aldrich), strontium carbonate, $SrCO_3$ (97.5 %, AlfaAesar), strontium acetate, $Sr(CH_3COO)_2$ (98 %, Aldrich), aluminium oxide, Al_2O_3 (99.5 % NanoDur™, AlfaAesar), aluminium nitrate nonahydrate, $Al(NO_3)_3 \cdot 9\,H_2O$ (98 %, Aldrich), calcium carbonate, $CaCO_3$ (99 %, CarlRoth), barium carbonate, $BaCO_3$ (98.5 %, Aldrich), boric acid, H_3BO_3 (99.8 %, CarlRoth), cerium oxide, CeO_2 (99.9 %, Aldrich), cerium nitrate hexahydrate, $Ce(NO_3)_3 \cdot 6\,H_2O$ (99 %, Merck), europium oxide, Eu_2O_3 (99.99 %, Tailorlux), dysprosium oxide, Dy_2O_3 (99.9 %, CarlRoth), acetone, $(CH_3)_2CO$ (98 %, Eurochemicals), glycerol, $HOCH_2CHOHCH_2OH$ (99 %, Standard), ethane-1,2-diol, $HOCH_2CH_2OH$ (99 %, Aldrich), acetic acid, CH_3COOH (98 %, Lachema) and distilled water.

2.2 Synthesis methods

An aqueous sol-gel synthesis method was used in order to obtain undoped and cerium-doped various strontium aluminates, namely $SrAl_2O_4$, $Sr_3Al_2O_6$, $SrAl_{12}O_{19}$ and $Sr_4Al_{14}O_{25}$. Also, conventional solid-state synthesis was used for the preparation of $Sr_{(4-x)}M_xAl_{14}O_{25}$ (where M = Ca or Ba) and $SrAl_4O_7$ samples.

2.2.1 Sol-gel

The $Sr-Al-O$ and $Sr-Ce-Al-O$ precursor gels were prepared via aqueous sol-gel synthesis route. Stoichiometric amounts of metal salts (i.e. $Sr(NO_3)_2$, $Al(NO_3)_3 \cdot 9\,H_2O$ and $Ce(NO_3)_3 \cdot 6\,H_2O$) were dissolved in 0.2 M acetic acid solution and complexing agent (1,2-ethanediol or glycerol) was added. The beakers were closed with a glass lid and solution was stirred at ∼60 °C for 1 h.

After removing a lid the clear solution was slowly evaporated at the same temperature. A viscous sol and then yellowish gel have formed during the sol-gel processing. The gels were dried at $\sim$120 °C in the drying oven overnight, thoroughly ground in agate mortar and initially heated for 8 h at 800 °C in air. The obtained white powders were thoroughly ground in agate mortar. In case of $Sr_4Al_{14}O_{25}$, additional amount of fluxing agent (boric acid) was mixed in. Then the samples were annealed in the furnace at 900–1600 °C for 10 h.

2.2.2 Solid-state

The $Sr_4Al_{14}O_{25}$, $Sr_{(4-x)}Ca_xAl_{14}O_{25}$, $Sr_{(4-x)}Ba_xAl_{14}O_{25}$ and $SrAl_4O_7$ samples were prepared using conventional solid-state reaction synthesis. Stoichiometric amounts of starting materials ($SrCO_3$, $BaCO_3$ or $CaCO_3$ and nanosized Al_2O_3) with additional amount of fluxing agent (H_3BO_3) were mixed in agate mortar (using small amount of acetone as mixing medium). In the case of $Sr_4Al_{14}O_{25}$ phase and its related compounds, the obtained precursor blends were annealed twice – first time at 1000 °C for 4 h and second time at 1300 °C for 8 h with additional grinding in agate mortar after each heat treatment. In the case of $SrAl_4O_7$ phase, the precursor blends were sintered in a furnace using step heating program. First, temperature was raised to 550 °C with heating rate of 10 °/min. Then the temperature was raised to 950 °C with heating of 0.5 °/min. After heating for 4 h at the same temperature, the samples were cooled slowly (1 °/min) to 800 °C. Finally, the heating furnace program ended and samples cooled down to room temperature.

2.3 Instrumentation and characterization techniques

2.3.1 Powder X-ray diffraction analysis

Powder X-ray diffraction (XRD) measurements were performed at room temperature on four diffractometers:

- *DS Bruker AXS* diffractometer (Cu $K\alpha$ radiation: λ = 1.5418 Å);
- *Rigaku SmartLab* diffractometer working in parallel beam ($\theta/2\theta$) geometry, using 2.5° Soller slits and Cu $K\alpha$ radiation. Samples were spun at

$30\,\mathrm{rpm}$, measurements were taken at step of $0.02°$ and at speed of $4\,\mathrm{s/step}$;

- *Rigaku MiniFlex II* diffractometer working in Bragg-Brentano ($\theta/2\theta$) geometry, the data were collected at a step of $0.01°$ and at speed of $0.06\,\mathrm{s/step}$ using Cu K_α radiation;
- *Bruker D8 Advance* diffractometer, the data were collected at a step of $0.01°$ and at speed of $0.06\,\mathrm{s/step}$ using Cu $K\alpha$ radiation.

Rietveld refinement was performed on the data using the software *FullProf* or *TOPAS* software package provided with the Bruker instrument. The refined parameters are as follows:

- Scale factor
- Sample displacement
- Background
- Lattice parameters
- Peak shape parameters
- Atomic coordinates
- Preferred orientation
- Atomic displacement parameters
- Asymmetry
- Site occupancies (for Ca or Ba substituted $Sr_4Al_{14}O_{25}$)

2.3.2 Scanning electron microscopy

The scanning electron microscopy (SEM) analysis was performed under vacuum in the specimen chamber of EVO 50 XVP or Hitachi SU-70 scanning electron microscopes.

2.3.3 Infrared spectrscopy

The infrared spectra in the range of 4000–$400\,\mathrm{cm}^{-1}$ were recorded on Perkin-Elmer FT-IR Spectrum BX II FTIR spectrometer. Samples were prepared as KBr pellets ($1.5\,\%$). The infrared spectra in the range of 2500–$500\,\mathrm{cm}^{-1}$ were recorded on PerkinElmer Frontier FT–NIR/MIR spectrometer with GladiATR attachment for Attenuated Total Reflection (ATR) sampling.

2.3.4 UV-Visible Spectroscropy

The UV-Vis diffuse reflectance spectra were recorded on PerkinElmer Lambda 35 UV-Vis spectrophotometer with an integrated $50\,\mathrm{mm}$ sphere attachment or on Shimadzu UV-3600 spectrophotometer equipped with integration sphere. $BaSO_4$ was used as a reflectance standard.

2.3.5 Photoluminescence measurements

Excitation and emission spectra were recorded on PerkinElmer LS-55 fluorescence spectrometer equipped with Hamamatsu R928 photomultiplier.

2.3.6 Thermogravimetric analysis

Thermogravimetric analysis (TG) was performed with PerkinElmer STA6000 apparatus. Measurements were collected by heating from $30.0\,^{\circ}\mathrm{C}$ to $995.0\,^{\circ}\mathrm{C}$ at heating rate of $10\,^{\circ}\mathrm{C}/\mathrm{min}$ under flow of synthetic air ($20\,\mathrm{mL}/\mathrm{min}$).

3 Results and Discussion

3.1 Sol-gel synthesis of undoped and Ce-doped $SrAl_2O_4$

The XRD patterns of the $Sr-Al-O$ acetate-nitrate-glycolate gels which correspond to the nominal chemical composition of $SrAl_2O_4$ and heated from 700 to $1200\,^{\circ}\mathrm{C}$ for $10\,\mathrm{h}$ are shown in figure 3.1. The diffraction pattern of the obtained powder at $700\,^{\circ}\mathrm{C}$ were of lower intensity due to partial crystallization of precursors gel. However, the formation of few crystalline phases ($Sr_3Al_2O_6$ and $SrCO_3$) could be detected from the XRD pattern. The phase composition of the samples obtained at 800–$1200\,^{\circ}\mathrm{C}$ were qualitatively the same regardless the annealing temperature. The formation of spinel crystal structure strontium aluminate starts at $800\,^{\circ}\mathrm{C}$. The XRD pattern of the sample heated at $1100\,^{\circ}\mathrm{C}$ shows the formation $SrAl_2O_4$ and $Sr_3Al_2O_6$ crystalline phases. According to XRD analysis, synthesis performed at $1200\,^{\circ}\mathrm{C}$ yields monophasic crystalline monoclinic $SrAl_2O_4$ sample.

Monophasic $SrAl_2O_4$ sample was characterized by high resolution powder X-ray diffraction analysis and obtained data were analyzed employing Rietveld refinement method. The original crystallographic data of $SrAl_2O_4$ (ICSD#160296) were used as a starting model. Rietveld analysis results are shown in figure 3.2. The refinement smoothly converged to the structure close to the starting model based on X-ray powder diffraction data. Calculated unit cell parameters ($a = 8.439\,24(46)$ Å, $b = 8.821\,58(46)$ Å, $c = 5.151\,40(28)$ Å and $\beta = 93.3769(13)°$) are close to ones published in literature [36]. The obtained results evidently confirmed that sol-gel derived $SrAl_2O_4$ sample obtained at $1200\,^{\circ}\mathrm{C}$ is monophasic.

FTIR analysis of synthesized samples is important both for the control of the reaction process and the properties of materials obtained. Figure 3.3 shows the FTIR spectra of $SrAl_2O_4$ ceramics obtained at 800 and $1200\,^{\circ}\mathrm{C}$. The synthesized ceramics show several intense broad bands. Strong absorption bands aris-

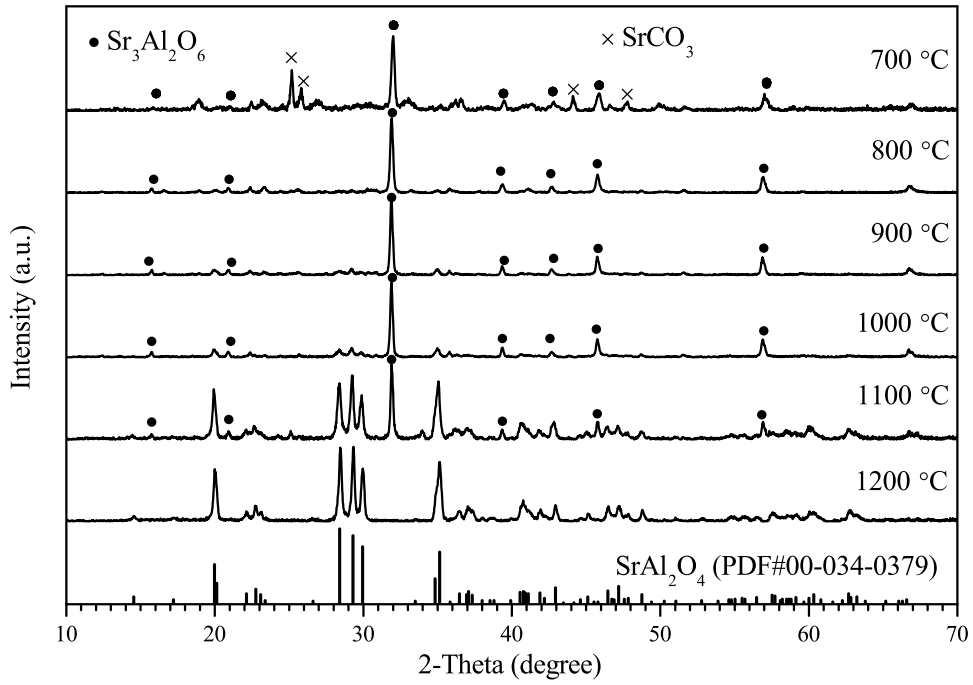

Figure 3.1. XRD patterns of sol-gel derived $SrAl_2O_4$ synthesized at different temperatures.

ing from O – H stretching and bending vibration of water due to the exposure of the samples to the atmosphere occur at $\sim$3500–3400 and $\sim 1600\,\mathrm{cm}^{-1}$, respectively [214]. Importantly, in the 1000–$500\,\mathrm{cm}^{-1}$ fingerprint region, several sharp bands are typical metal–oxygen absorptions (Sr – O and Al – O stretching frequencies), probably characteristic for the spinel-type compounds [215]. The spectra of strontium aluminate samples show the strong peaks at $\sim 1500\,\mathrm{cm}^{-1}$. The exact origin of this peak, however, is not very clear. It is known, that typical carbonate vibrations are $\sim$1470–$1390\,\mathrm{cm}^{-1}$ (triply degenerated stretching mode) and $\sim$880–$850\,\mathrm{cm}^{-1}$ (doubly degenerated stretching mode) [216]. So, the bands located at $\sim 1500\,\mathrm{cm}^{-1}$ could not be assigned to the metal carbonates formed as intermediates during high-temperature treatments. It is well known that aluminum and strontium carbonates ($Al_2(CO_3)_3$ and $SrCO_3$) decomposes at lower temperatures [217, 218, 219].

The SEM images of $SrAl_2O_4$ ceramics calcined at 800 and $1200\,^{\circ}\mathrm{C}$ are shown in figure 3.4. The particles obtained at $800\,^{\circ}\mathrm{C}$ seem to be micro-sized solids with particle size about $\sim$10–$15\,\mu\mathrm{m}$ and they are partially fused to form hard agglomerates ($\sim$30–$50\,\mu\mathrm{m}$ in size). With increasing temperature up to $1200\,^{\circ}\mathrm{C}$ the formation of spherical crystals with regular size is evident, i.e. the SEM images revealed agglomerated grains of different size ranging from $1\,\mu\mathrm{m}$ to $2\,\mu\mathrm{m}$.

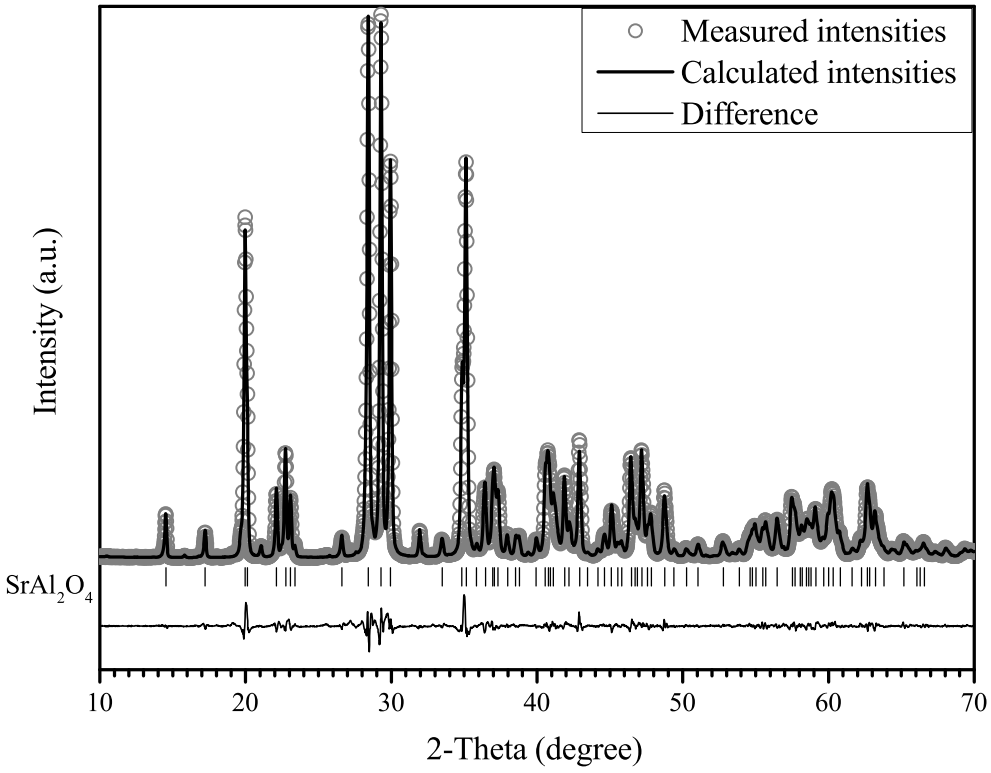

Figure 3.2. The observed (circles) and calculated (solid line) powder XRD patterns of sol-gel derived $SrAl_2O_4$ sample after Rietveld refinement. The vertical bars located just below the background level indicate calculated positions of Bragg peaks for $K_{\alpha 1}$. The curve the bottom part of the plot represents the difference between observed and calculated intensities. Goodness of fit indicators: $\chi^2 = 0.45$; $R_{wp} = 7.05$.

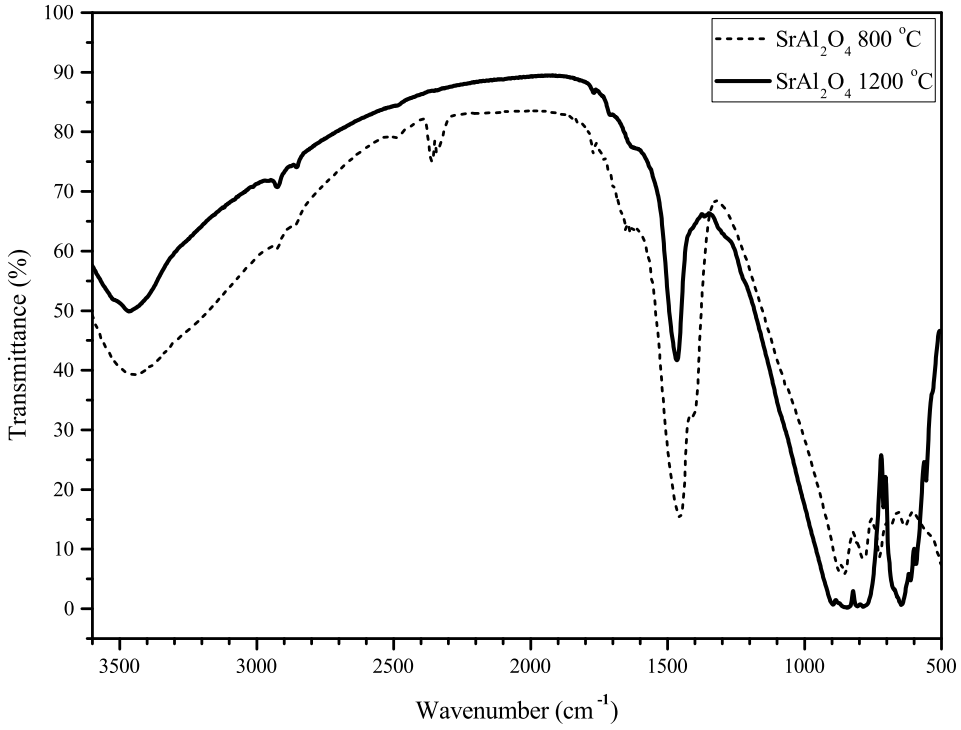

Figure 3.3. FTIR spectra of $SrAl_2O_4$ synthesized at different temperatures.

The particle size does not change and no progressive change in morphology was observed with changing chemical composition or crystal structure of sol-gel derived strontium aluminates.

The XRD patterns of the $SrAl_2O_4$:Ce_x specimens annealed at $1200\,^{\circ}\mathrm{C}$ temperature for $10\,\mathrm{h}$ are shown in figure 3.5. As seen, in all cases the $SrAl_2O_4$:Ce_x phase is dominating and only minor amount of impurity phases has formed. The XRD patterns of $SrAl_2O_4$:Ce_x samples with smaller concentrations of cerium (0.25–$1.00\,\mathrm{mol}\%$) contained additional peak located at approximately $2\theta \approx 32°$. However we were not able to attribute this peak to any crystalline phase. Interestingly, this peak disappeared with further increasing concentration of cerium in $SrAl_2O_4$:Ce_x. On the other hand, the XRD patterns of $SrAl_2O_4$:Ce_x samples with higher concentrations of cerium (2.00–$3.00\,\mathrm{mol}\%$) showed the negligible formation of CeO_2 phase. The small diffraction peaks attributable to ceria phase are visible at $2\theta \approx 33°$.

Figure 3.6 demonstrates the reflection spectra of $SrAl_2O_4$:Ce_x ceramic powders produced by sol-gel method. As seen, the reflection spectra qualitatively are almost identical regardless the substitutional level of cerium. In UV range the strontium aluminate samples show a significant increase of reflection up to

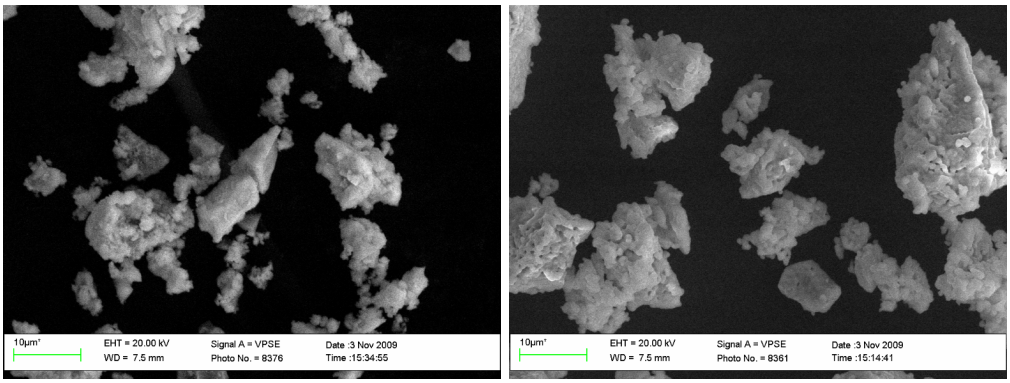

Figure 3.4. SEM micrographs of $SrAl_2O_4$ ceramics annealed at $800\,^{\circ}\mathrm{C}$ (left) and $1200\,^{\circ}\mathrm{C}$ (right).

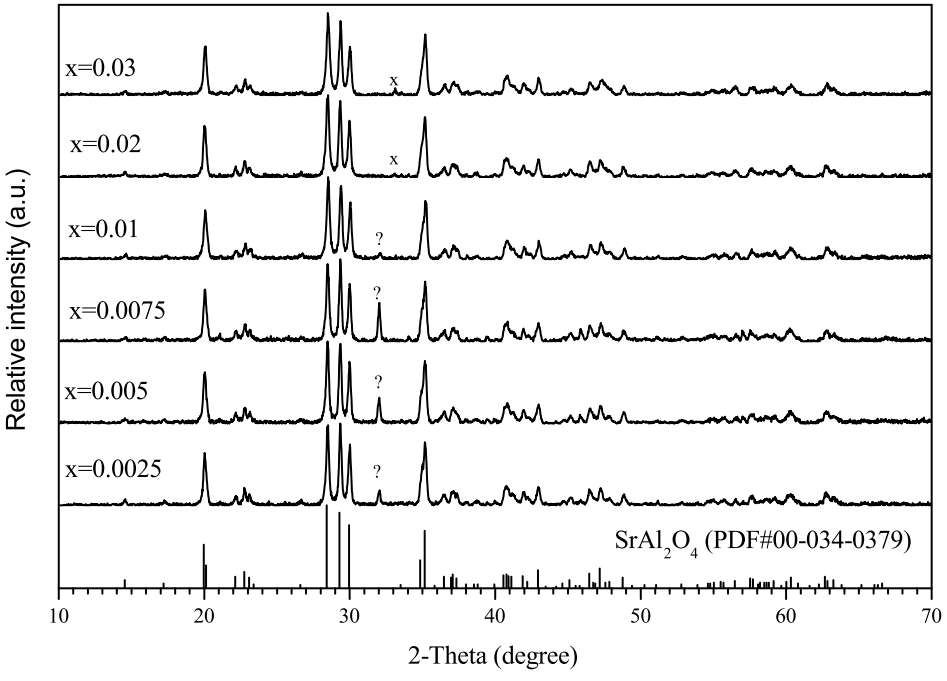

Figure 3.5. XRD patterns of $SrAl_2O_4$:Ce_x ceramic samples synthesized at $1200\,^{\circ}\mathrm{C}$. The concentration of cerium from bottom to the top is $x_{Ce} = 0.25$, 0.50, 0.75, 1.00, 2.00 and $3.00\,\mathrm{mol}\%$. Impurity phases: (?) unknown; (x) CeO_2.

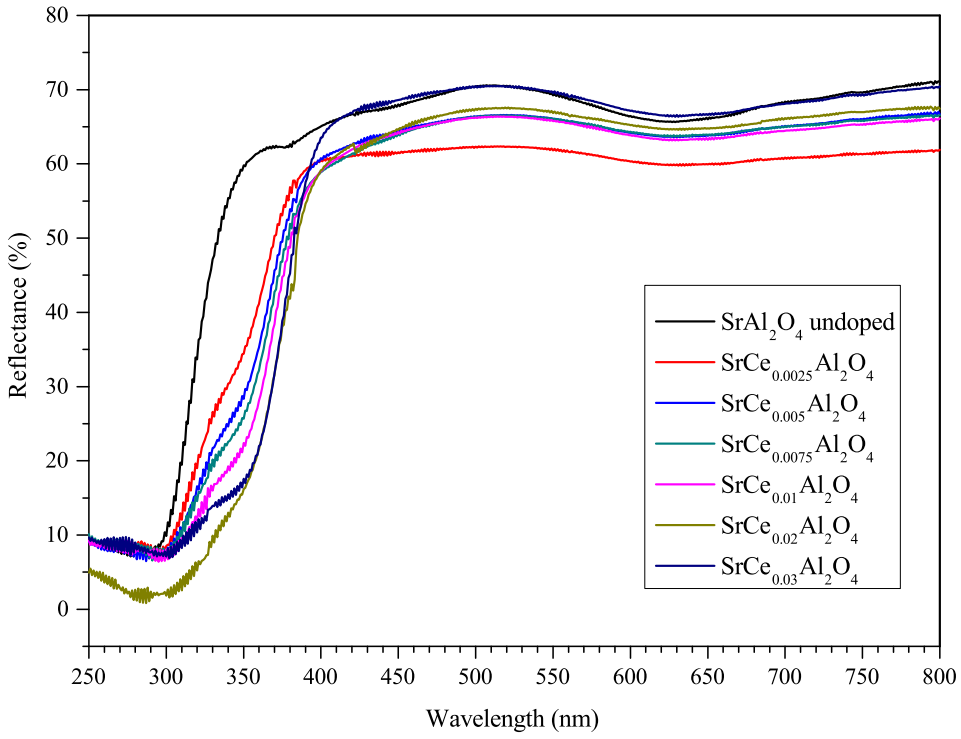

Figure 3.6. Reflection spectra of $SrAl_2O_4$:Ce_x samples as a function of Ce concentration.

400 nm. From this point the reflection is almost constant, i.e. not wavelength dependent. However, broad absorption bands could be detected between 575 nm and 700 nm. These results clearly show that optical properties of $SrAl_2O_4$:Ce_x are quite different from the Ce-doped garnet samples [24,66,67]. In the case of garnet materials, from 400 nm the reflection abruptly decreases and again increases starting from 455 nm. And only in the higher wavelength region (from $\sim$545 nm) the reflection is almost constant.

Attempts to measure photoluminescence of $SrAl_2O_4$:Ce_x were unsuccessful.

3.2 Sol-gel synthesis of undoped and Ce-doped $Sr_3Al_2O_6$

The XRD patterns of Sr−Al−O precursor powders which correspond to the nominal chemical composition of $Sr_3Al_2O_6$ and sintered from 700 to 1200 °C for 10 h are shown in figure 3.7. According to the XRD analysis, the formation of $Sr_3Al_2O_6$ along with $SrCO_3$ has started already at 700 °C. Fully crystallized single-phase oxide $Sr_3Al_2O_6$ with well pronounced cubic crystal structure has

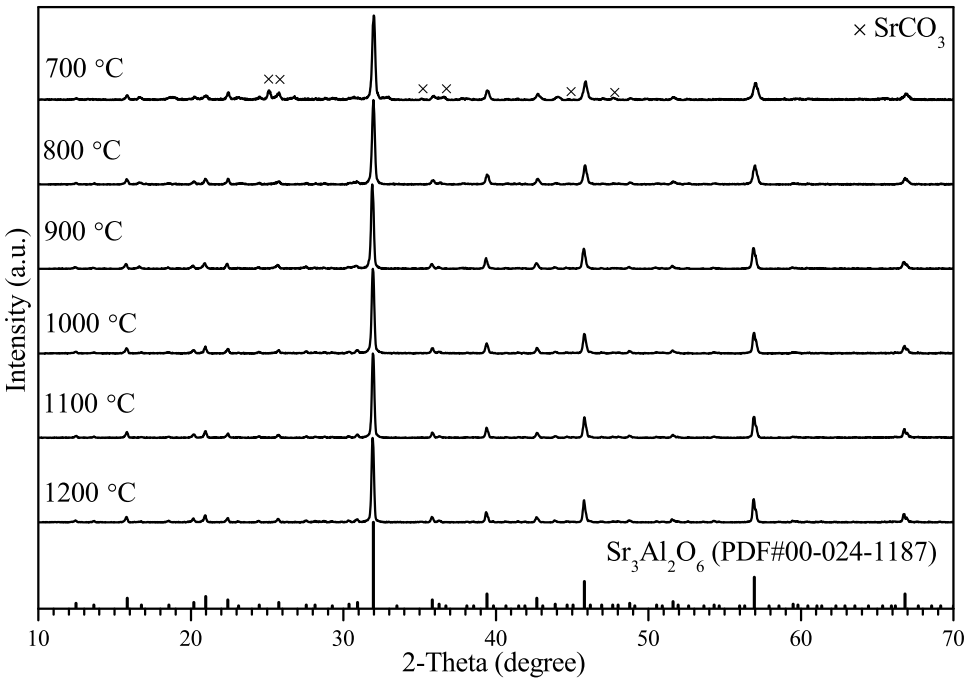

Figure 3.7. XRD patterns of sol-gel derived $Sr_3Al_2O_6$ synthesized at different temperatures.

formed already at $800\,^{\circ}\mathrm{C}$ (PDF#00-024-1187). The initial studies of XRD patterns of these samples calcined in the temperature range of 800–$1200\,^{\circ}\mathrm{C}$ suggested $Sr_3Al_2O_6$ to be the only one crystalline component.

In order to prove monophasicity, the $Sr_3Al_2O_6$ sample was characterized by high resolution powder X-ray diffraction analysis and obtained data were analysed employing Rietveld refinement method. The original crystallographic data of $Sr_3Al_2O_6$ (ICSD#71860) was used as a starting model. Rietveld analysis results are shown in figure 3.8. During structure refinement it was noticed, that not all diffraction peaks observed in the XRD pattern are covered. Therefore, two additional phases, namely $SrAl_2O_4$ (ICSD#160296) and $SrAl_4O_7$ (ICSD#2817) were added to the starting model. The refinement smoothly converged to the structure close to the starting model based on X-ray powder diffraction data. Therefore, it was determined that the phase of interest ($Sr_3Al_2O_6$) makes only about $60\,\%$ of the specimen. This was impossible to determine without Rietveld refinement, because cubic $Sr_3Al_2O_6$ structure gives very intensive reflection at $2\theta = 31.9°$ and it becomes difficult to separate low intensity peaks from background noise.

The FTIR spectra of $Sr_3Al_2O_6$ samples synthesized at different temperatures are shown in figure 3.9. The envelope of three broad absorption bands in the

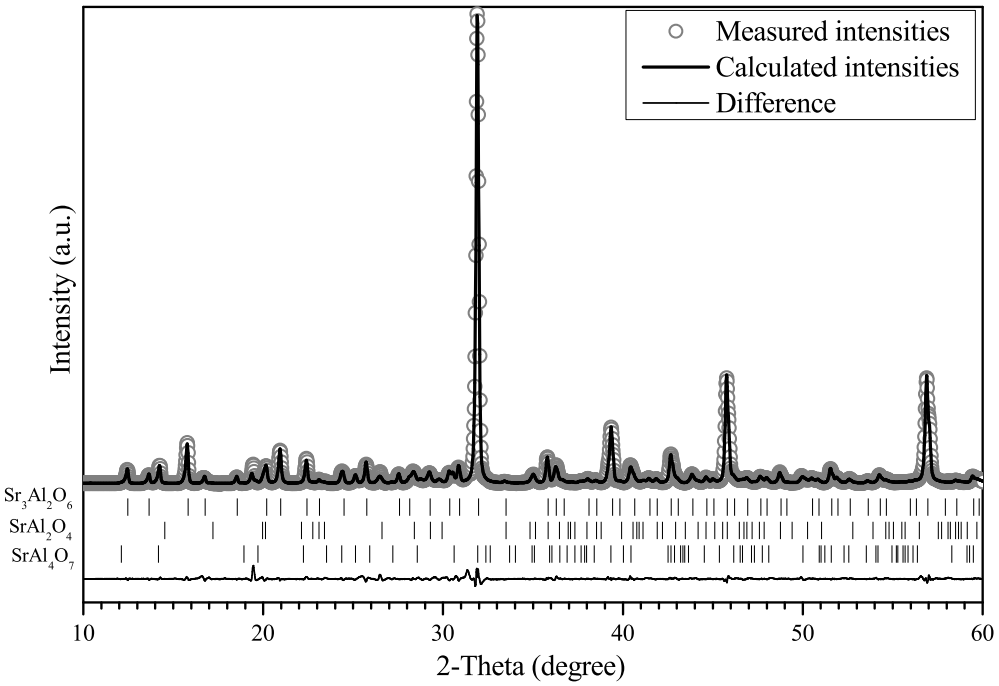

Figure 3.8. The observed (circles) and calculated (solid line) powder XRD patterns of sol-gel derived $Sr_3Al_2O_6$ sample after Rietveld refinement. The vertical bars located just below the background level indicate calculated positions of Bragg peaks for $K_{\alpha 1}$. The curve the bottom part of the plot represents the difference between observed and calculated intensities. Goodness of fit indicators: $\chi^2 = 0.40$; $R_{wp} = 10.81$.

region of 1000–$500\,\mathrm{cm}^{-1}$ presented in Fig. 3.9 is well resolved. The both FTIR spectra of $Sr_3Al_2O_6$ samples are almost identical. Besides, they are very similar to FTIR spectra of $SrAl_2O_4$ ceramics (Figure 3.3). The spectra of $Sr_3Al_2O_6$ samples also show the strong peaks at $\sim 1500\,\mathrm{cm}^{-1}$. However, the existence of non-decomposed metal carbonates in the product synthesized at $1200\,^{\circ}\mathrm{C}$ temperature is very unlikely. Therefore, the origin of this absorption band is not clear.

Figure 3.10 show the surface features of the $Sr_3Al_2O_6$ powders calcined at different temperatures. From these SEM images it is evident that $Sr_3Al_2O_6$ powders are also composed of plate-like crystallites having a similar size and the tendency to form agglomerates. The SEM micrographs of the samples annealed at higher temperature exhibit clustered grains made up of several tiny crystallites with a defined microstructure.

The XRD patterns of $Sr_3Al_2O_6$:Ce_x powders sintered at $850\,^{\circ}\mathrm{C}$ for $10\,\mathrm{h}$ are shown in figure 3.11. As seen. the main crystalline phase is cerium-doped strontium aluminate $Sr_3Al_2O_6$ without the formation of any impurity phases (without

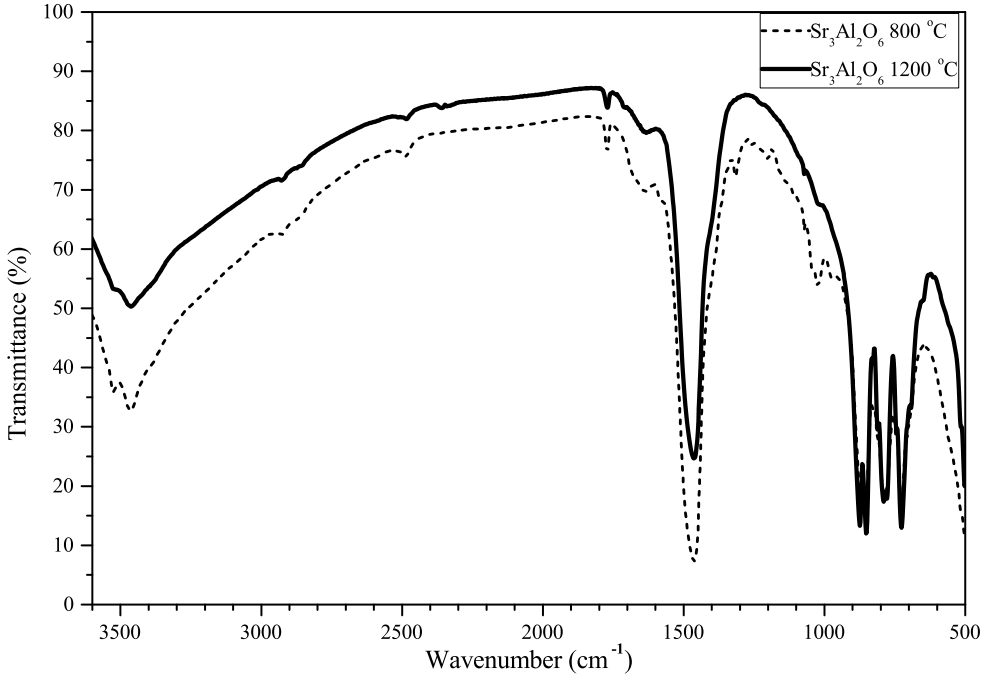

Figure 3.9. FTIR spectra of $Sr_3Al_2O_6$ synthesized at different temperatures.

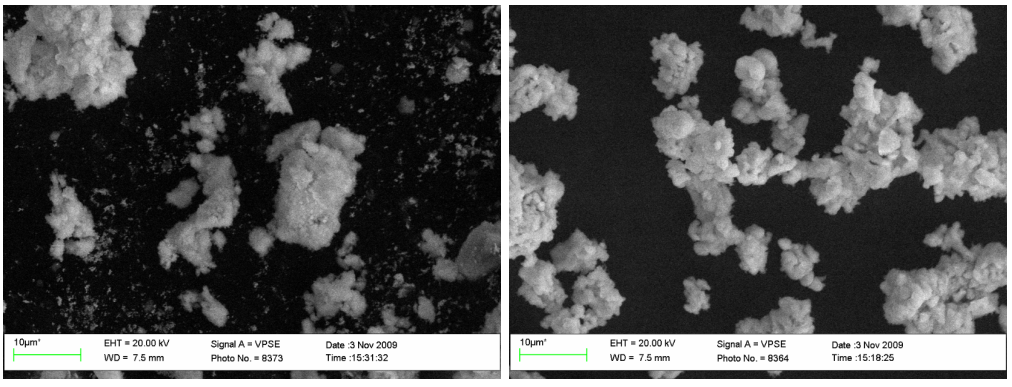

Figure 3.10. SEM micrographs of $Sr_3Al_2O_6$ ceramics annealed at 800 °C (left) and 1200 °C (right).

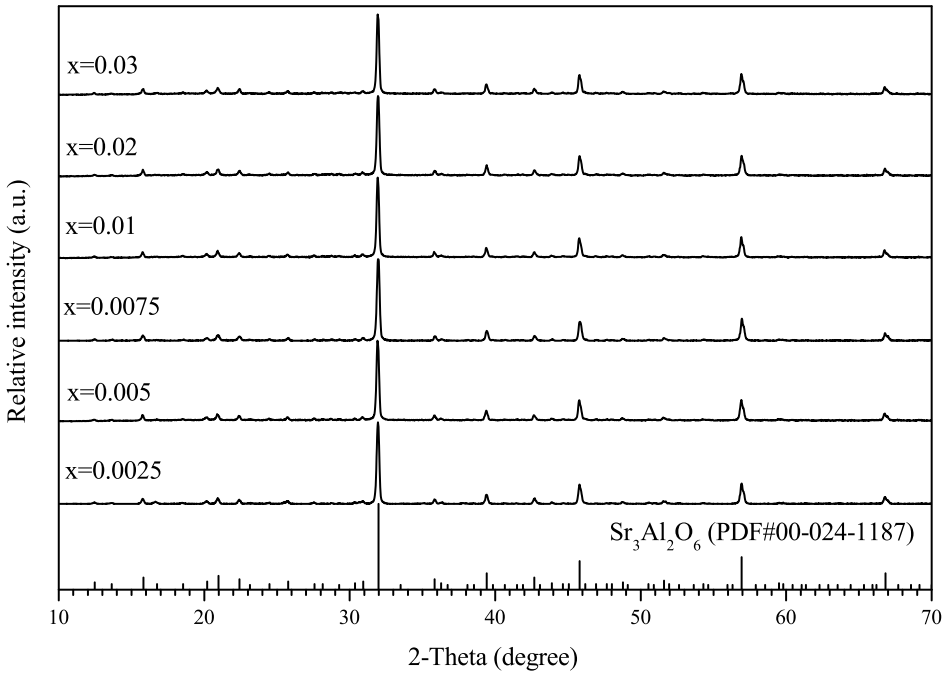

Figure 3.11. XRD patterns of $Sr_3Al_2O_6$:Ce_x ceramic samples synthesized at $850\,^{\circ}\mathrm{C}$. The concentration of cerium from bottom to the top is $x_{Ce} = 0.25$, 0.50, 0.75, 1.00, 2.00 and $3.00\,\mathrm{mol}\%$.

measuring on high-resolution equipment).

Figure 3.12 shows UV-Vis reflection and photoluminescence measurements data of undoped ($Sr_3Al_2O_6$) and Ce^{3+}-doped strontium aluminate ($Sr_3Al_2O_6$:Ce) samples having different concentration of cerium. The difference in the optical properties of doped and undoped samples is clearly visible. From the reflection spectra we can see that cerium ions increase absorption in the region of around $300\,\mathrm{nm}$. Excitation spectra of sol-gel derived strontium aluminates shows maximum at $268\,\mathrm{nm}$. As seen, the intensity of excitation bands increases monotonically with increasing concentration of cerium.

The measured emission spectra show a broad emission band peaked at $480\,\mathrm{nm}$. Again, the measured emission intensity increases with increasing amount of Ce^{3+} in the series of samples up to $3\,\%$ of cerium. The obtained results are in a good agreement with the study of $Sr_3Al_2O_6$:Ce compounds, synthesized using solid state reaction [95].

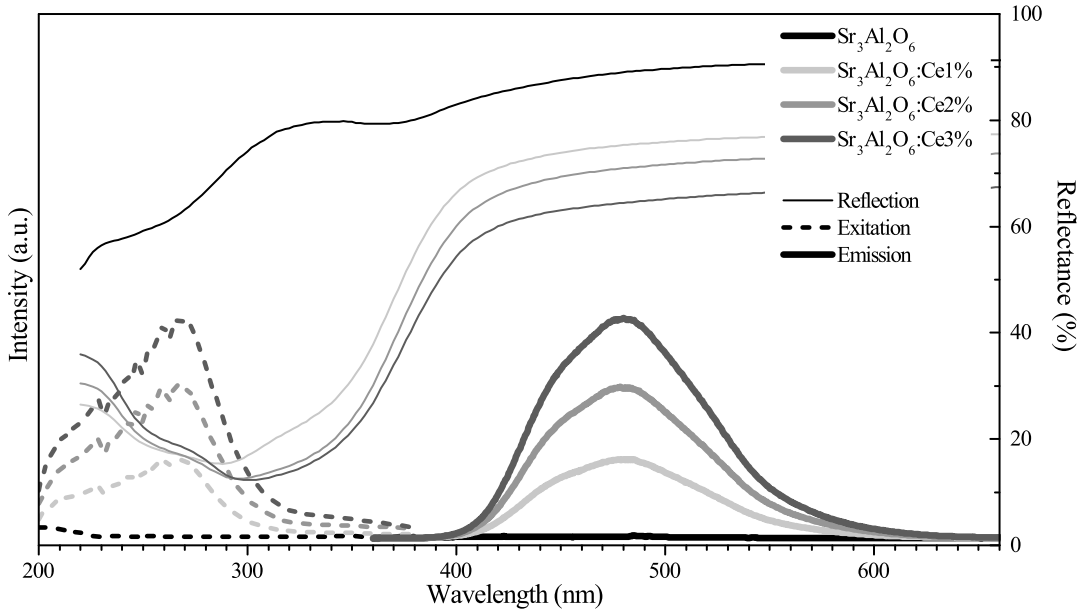

Figure 3.12. Reflection, excitation ($\lambda_{em} = 480\,nm$) and emission ($\lambda_{ex} = 268\,nm$) spectra of $Sr_3Al_2O_6$ and $Sr_3Al_2O_6$:Ce samples.

3.3 Sol-gel synthesis of undoped and Ce-doped $SrAl_{12}O_{19}$

The formation of $SrAl_{12}O_{19}$ phase in the temperature range of 700–1200 °C was initially found to be very problematic. In order to determine suitable parameters of the preparation of $SrAl_{12}O_{19}$ aluminate, a series of Sr – Al – O precursor gels were annealed at high temperatures ranging from 1200 to 1600 °C. The XRD patterns of calcined at different temperatures Sr – Al – O precursor samples are shown in figure 3.13.

As seen from figure 3.13, the samples annealed at highest temperatures (1500–1600 °C) are single phase $SrAl_{12}O_{19}$ compounds. The synthesis products obtained in the temperature range of 1200–1400 °C contained $SrAl_{12}O_{19}$ as the main phase, but also impurity phases, such as $SrAl_2O_4$ and Al_2O_3. To prove the formation of monophasic $SrAl_{12}O_{19}$ at 1500 °C, this sample was analyzed more precisely. The high resolution X-ray diffraction data were collected and refined using Rietveld technique. The original crystallographic data of $SrAl_{12}O_{19}$ (ICSD#43155) were used as a starting model. Results of the Rietveld refinement are shown in figure 3.14.

During refinement it was noticed, that not all diffraction peaks presented in the XRD pattern are covered. Therefore, crystallographic data of $SrAl_2O_4$ phase

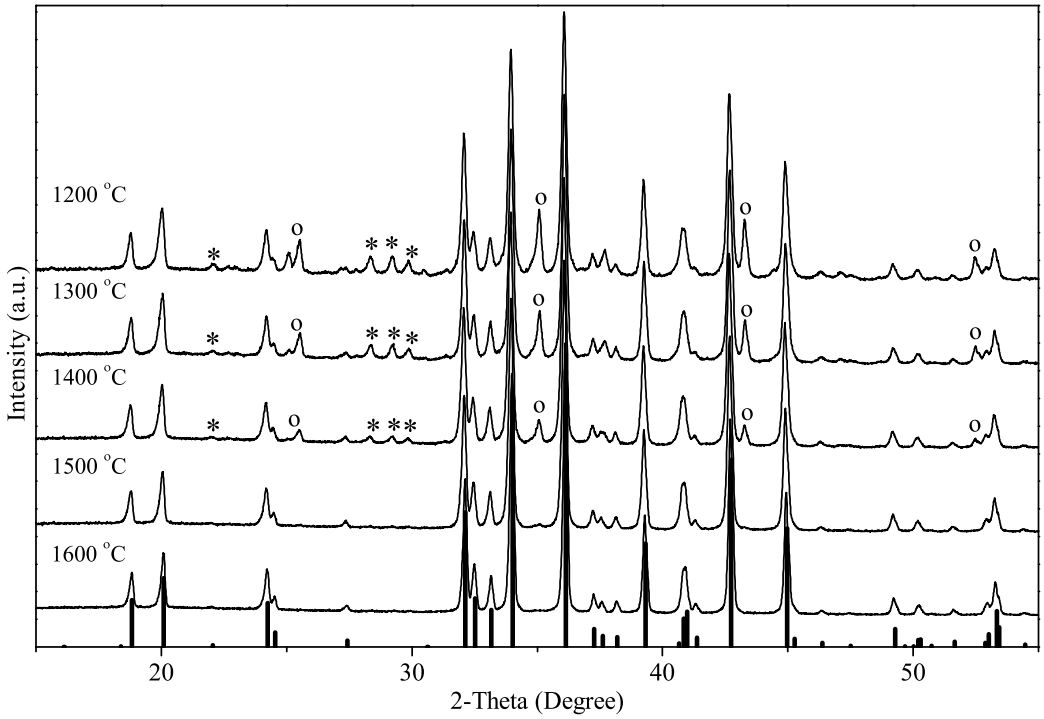

Figure 3.13. XRD patterns of $SrAl_{12}O_{19}$ samples annealed at different temperatures. Solid lines at the bottom of figure represent $SrAl_{12}O_{19}$ (PDF#00-080-1195). The side phases are marked: $*$ – $SrAl_2O_4$ (PDF#00-046-1212) and $\circ$ – Al_2O_3 (PDF#00-088-0826).

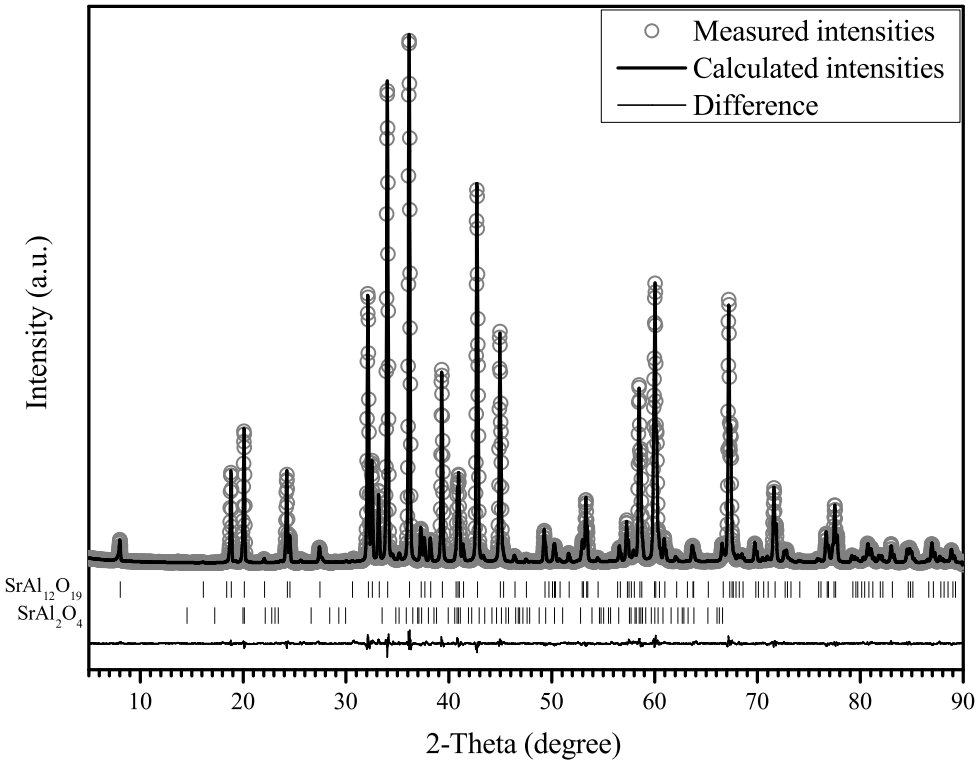

Figure 3.14. The observed (circles) and calculated (solid line) powder XRD patterns of sol-gel derived $SrAl_{12}O_{19}$ sample after Rietveld refinement. The vertical bars located just below the background level indicate calculated positions of Bragg peaks for $K_{\alpha 1}$. The curve the bottom part of the plot represents the difference between observed and calculated intensities. Goodness of fit indicators: $\chi^2 = 0.30$; $R_{wp} = 5.58$.

(ICSD#160296) were added to the starting model. The refinement smoothly converged to the structure close to the starting model based on X-ray powder diffraction data. It was determined that the second phase makes up only traces (less than $1\,\%$). Thus, the sol-gel derived $SrAl_{12}O_{19}$ sample can be considered as monophasic.

Figure 3.15 shows UV-Vis reflection and photoluminescence measurements data of undoped and Ce^{3+} doped strontium aluminate $SrAl_{12}O_{19}$ samples having different concentration of cerium. In the reflection spectra it is visible that Ce^{3+} ions originate absorption peaks at around $\sim 226\,\mathrm{nm}$, $\sim 244\,\mathrm{nm}$ and $\sim 274\,\mathrm{nm}$. Excitation and emission maximum of $SrAl_{12}O_{19}$:Ce samples are clearly visible at $260\,\mathrm{nm}$ and $317\,\mathrm{nm}$, respectively. These results are similar to the luminescence measurements of $Sr_{0.95}Ce_{0.05}Mg_{0.05}Al_{11.95}O_{19}$ [104]. Interestingly, the photoluminescence spectra of $SrAl_{12}O_{19}$:Ce samples shows, that the highest intensity was observed when cerium concentration reaches $2\,\%$. With increasing concentration of cerium the decreasing of the emission intensity is observed due to the concentration quenching [220].

In comparison with luminescent properties of $Sr_3Al_2O_6$:Ce samples (emission peaked at $480\,\mathrm{nm}$), the emission band of $SrAl_{12}O_{19}$:Ce samples is shifted to the blue-UV region ($317\,\mathrm{nm}$).

3.4 Sol-gel synthesis of undoped and Ce-doped $Sr_4Al_{14}O_{25}$

In order to study the behaviour of $Sr-Al-O$ gels during thermal decomposition, thermogravimetric measurements were firstly recorded. The TG curves of starting materials and corresponding gels are shown in figure 3.16. As we can see from Fig. 3.16, the $Sr-Al-O$ gels with and without boric acid (flux) decompose almost at the same rate up to $180\,^{\circ}\mathrm{C}$. The main decomposition of the gels occurs in the temperature range of 180–$350\,^{\circ}\mathrm{C}$. As seen, both gels undergo the same mass loss in this range, although addition of flux causes more rapid process. Moreover, starting from temperature of $350\,^{\circ}\mathrm{C}$ different mass loss of two gels clearly is visible. The weight loss for the gel with flux is approximately $6\,\%$ greater than for the gel without flux. Although after decomposition of strontium nitrate in the temperature range of about 600 to $700\,^{\circ}\mathrm{C}$ the difference between mass loss of two gels lowers to approximately $3\,\%$, it is still higher than theo-

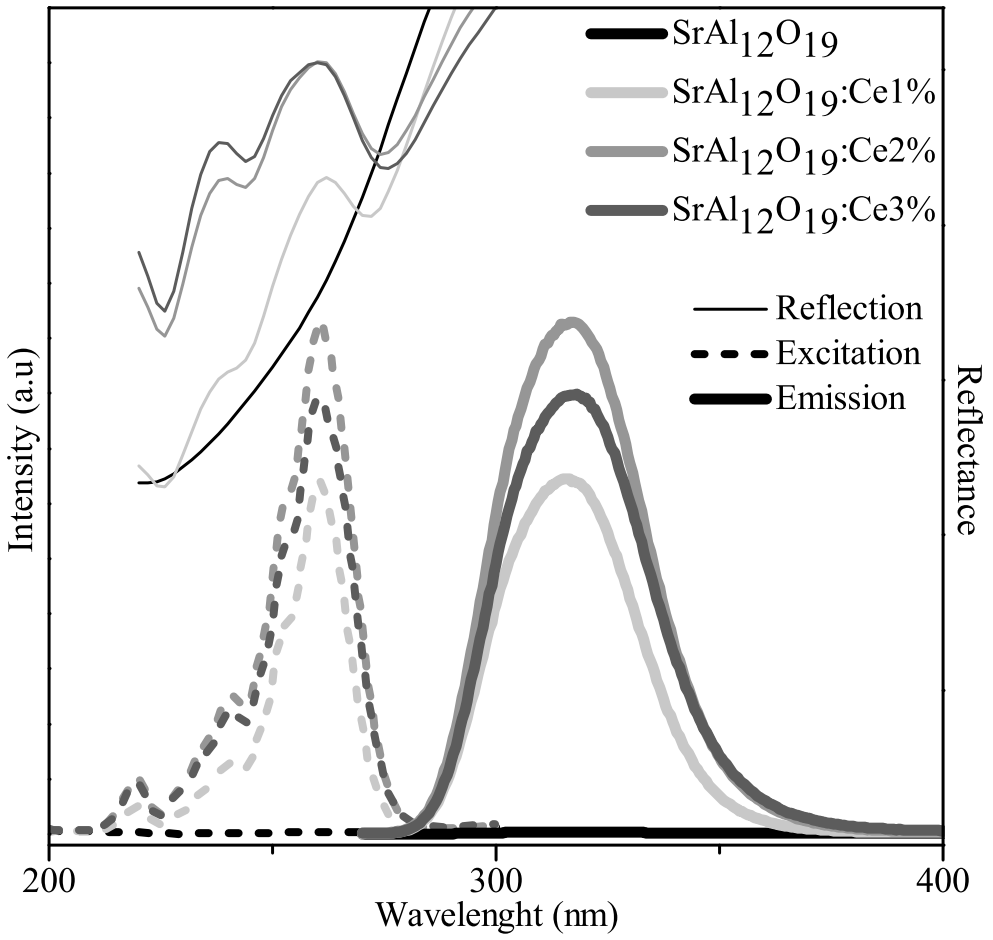

Figure 3.15. Reflection, excitation ($\lambda_{em} = 317\,nm$) and emission ($\lambda_{ex} = 260\,nm$) spectra of $SrAl_{12}O_{19}$ and $SrAl_{12}O_{19}$:Ce samples.

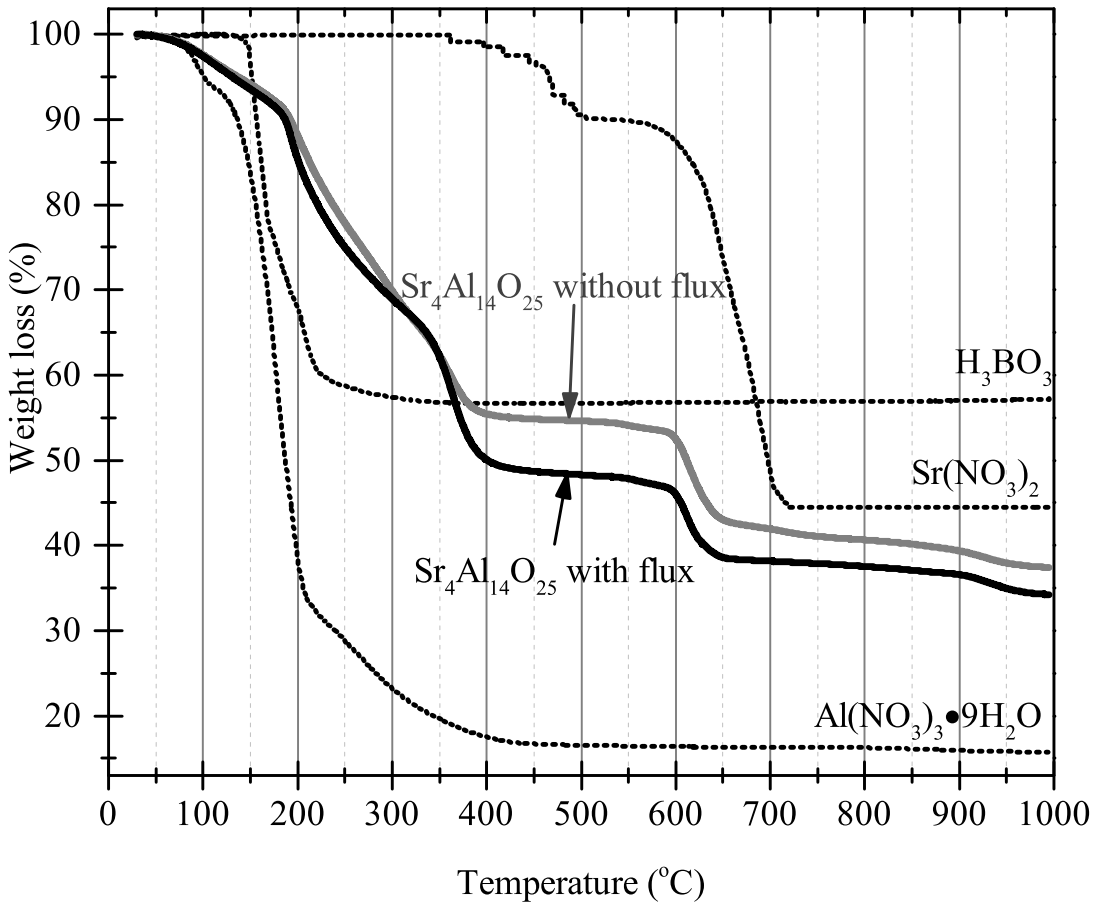

Figure 3.16. TG curves recorded for starting materials (dotted lines) and $Sr_4Al_{14}O_{25}$ gels prepared with and without flux (solid lines).

retical weight loss caused only by decomposition of additional boric acid, which is approximately $1\,\%$ ($2.5\,\%$ by weight added to the gel, which on its own undergoes $\sim 45\,\%$ weight loss). Therefore, the TG analysis data confirm that boric acid is involved in the process of formation of strontium aluminate. Also, from TG curves the temperature of final annealing of Sr – Al – O gels could be selected higher than $900\,^{\circ}\mathrm{C}$.

For the fabrication of $Sr_4Al_{14}O_{25}$ phase, Sr – Al – O precursor gels were heated at different temperatures in the range of 1000–$1600\,^{\circ}\mathrm{C}$. FTIR spectra of the $Sr_4Al_{14}O_{25}$ powders obtained after annealing of Sr – Al – O gels obtained with and without boric acid at different temperatures are shown in figure 3.17. Apparently, all FTIR spectra are very similar. The most important feature is that several intensive absorption bands are determined in the regions of 2400–$2200\,\mathrm{cm}^{-1}$ and 900–$500\,\mathrm{cm}^{-1}$. Bands at ca. $2350\,\mathrm{cm}^{-1}$ belong to carbon dioxide from atmosphere [214]. The last ones may be attributed to the stretching modes of the

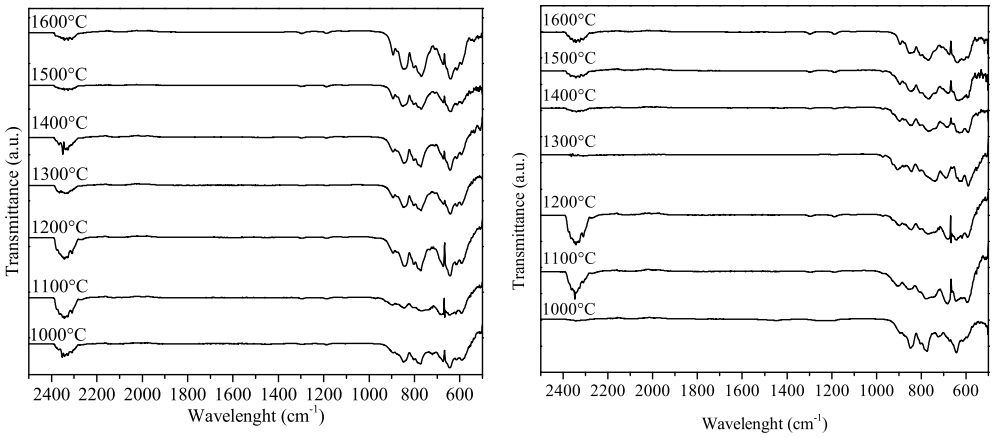

Figure 3.17. FTIR spectra of Sr – Al – O gels prepared without boric acid (at left) and with boric acid (at right) and annealed at different temperatures.

Sr – O and/or Al – O vibrations. Moreover, the FTIR spectra of all specimens do not exhibit the band at $\sim 1405\,\mathrm{cm}^{-1}$, assignable to ionic carbonates. Thus, the observed M – O vibrations in the FTIR spectra let us to conclude that crystallization process was rather similar for the both studied systems independent on the annealing temperature.

For comparison, the FTIR spectra of two $Sr_4Al_{14}O_{25}$ samples obtained at $1200\,^{\circ}\mathrm{C}$ without flux and using boric acid in the synthesis procedure are shown in figure 3.18.

The intensity of absorption lines located in the region of 900–$500\,\mathrm{cm}^{-1}$ is different for two samples prepared by two slightly different synthesis routes. This might be associated with existence of different similar aluminate phases in the samples. The clear answers should be received after characterization of the samples by XRD analysis.

Scanning electron microscopy measurements revealed that $Sr_4Al_{14}O_{25}$ samples prepared without and with addition of flux show different morphology. The SEM micrographs of sol-gel derived strontium aluminates are presented in figure 3.19.

The solids prepared without boric acid consist of irregular shape and size (from $200\,\mathrm{nm}$ to $1\,\mu\mathrm{m}$) particles. Most of the particles are necked to each other forming small agglomerates. On the other hand, the sample fabricated using boric acid in the synthesis processing consisted of hexagonal platelet shaped crystallites (see Fig. 3.19). Interestingly, the particle size and particle size distribution of both synthesis products are very similar. Nevertheless, the SEM results support above conclusions made analysing FTIR spectroscopy data, that the use

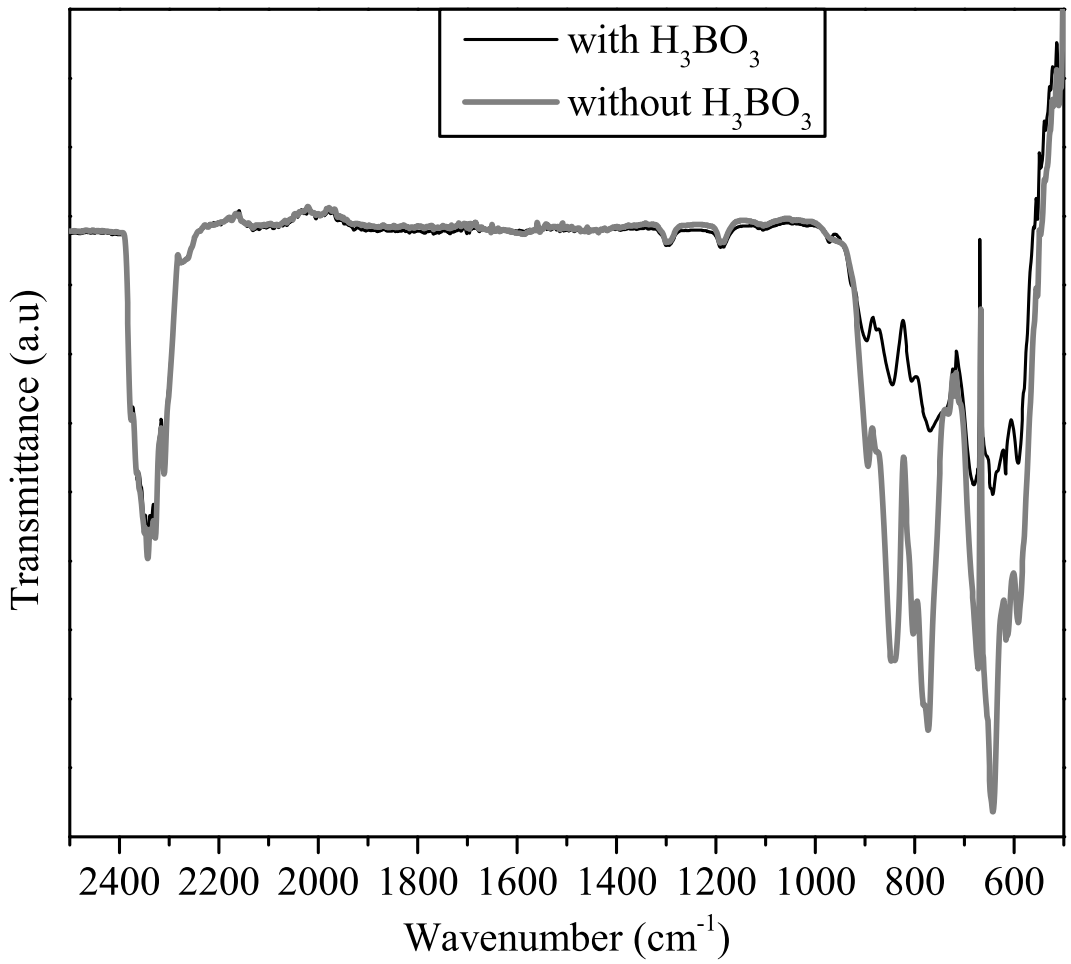

Figure 3.18. FTIR spectra of Sr – Al – O gels prepared without and with boric acid and annealed at 1200 °C.

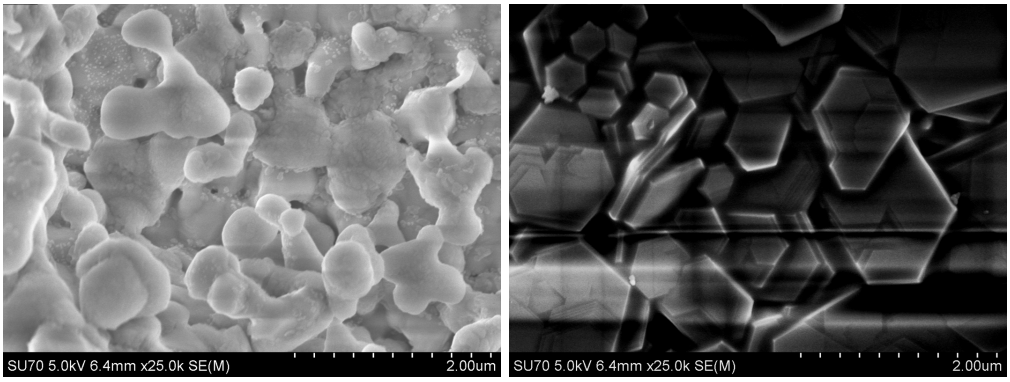

Figure 3.19. SEM micrographs of $Sr_4Al_{14}O_{25}$ strontium aluminate samples prepared without flux (left) and with addition of flux (right) and annealed at 1200 °C.

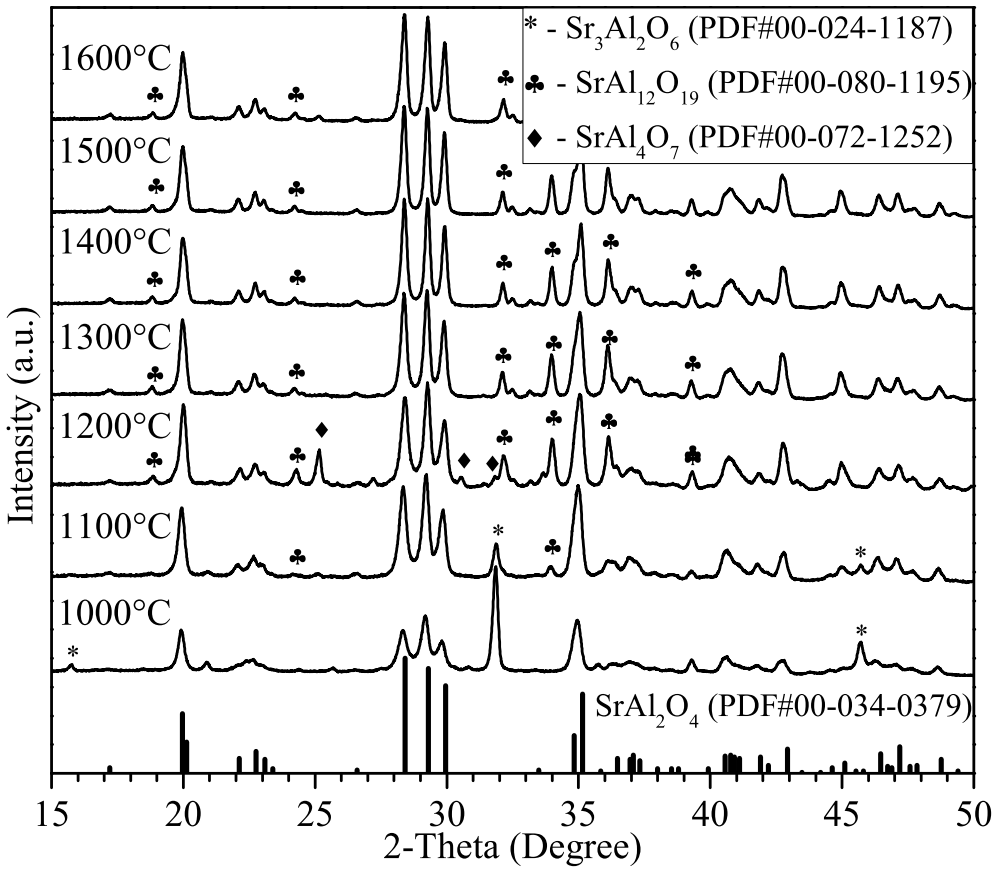

Figure 3.20. XRD patterns of $Sr_4Al_{14}O_{25}$ samples prepared at different temperatures without addition of boric acid. The vertical lines at bottom correspond to standard XRD pattern for $SrAl_2O_4$ phase.

of boric acid as fluxing agent in the sol-gel synthesis of $Sr_4Al_{14}O_{25}$ has an impact on phase composition of the end product.

Results of powder X-ray diffraction analysis of the samples prepared without addition of boric acid as a flux and annealed at different temperatures are shown in figure 3.20.

As we can see, annealing of $Sr-Al-O$ gels at $1000\,^{\circ}C$ did not yield very crystalline sample, and monoclinic $SrAl_2O_4$ and cubic $Sr_3Al_2O_6$ are the dominant crystalline phases. With increasing the annealing temperature up to $1600\,^{\circ}C$ the samples with higher crystallinity have formed. However the dominant phase was $SrAl_2O_4$ at any selected synthesis temperature. Moreover, other strontium aluminate phases, such as $Sr_3Al_2O_6$, $SrAl_{12}O_{19}$ and $SrAl_4O_7$ have formed during annealing the samples at elevated temperatures. Thus, the desired strontium aluminate $Sr_4Al_{14}O_{25}$ phase has not formed in whole temperature range used in these experiments.

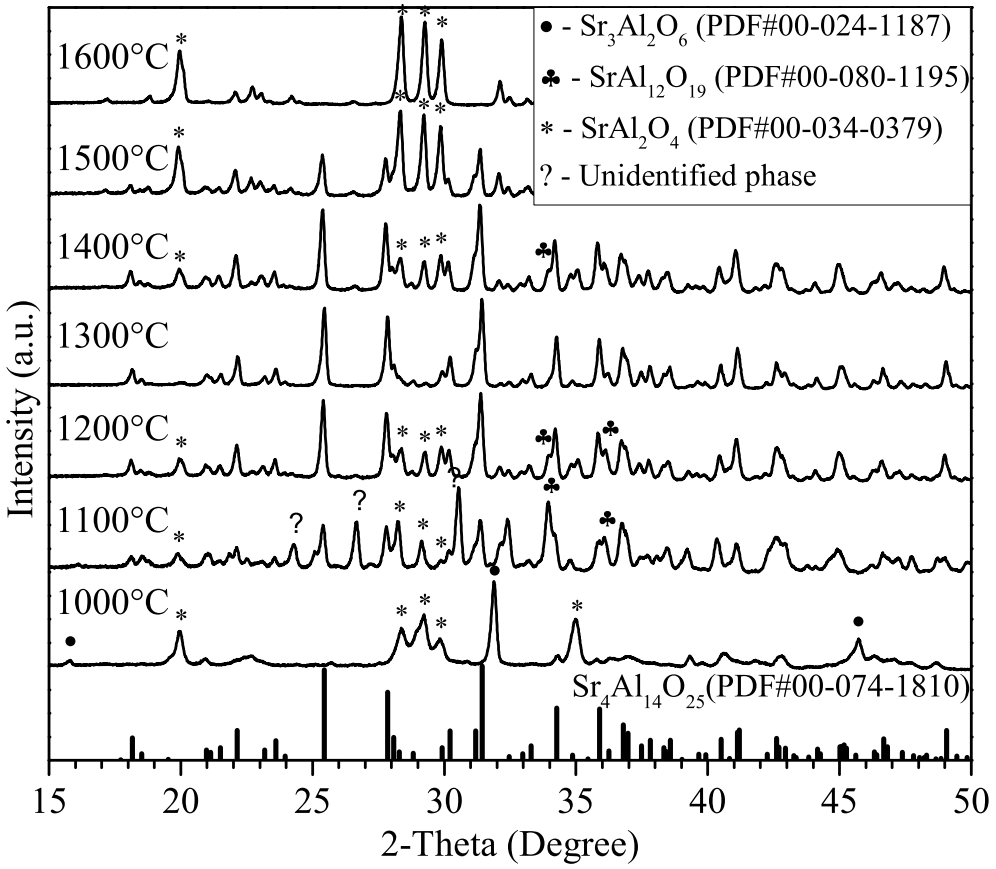

Figure 3.21. XRD patterns of strontium aluminate samples prepared at different temperatures with addition of boric acid. The vertical lines at bottom correspond to standard XRD pattern for $Sr_4Al_{14}O_{25}$ phase.

However, in the case when additional boric acid has been used as a fluxing agent in the synthesis procedure, totally different results have been obtained (Figure 3.21). Again, annealing of the samples at $1000\,^{\circ}\mathrm{C}$ did not yield very crystalline sample and the dominant phase was cubic $Sr_3Al_2O_6$ along with $SrAl_2O_4$. With increasing the temperature up to $1100\,^{\circ}\mathrm{C}$, however, not only crystallinity of the specimen has increased but the diffraction lines of desired $Sr_4Al_{14}O_{25}$ phase became visible in the XRD pattern. Interestingly, the strontium aluminate sample annealed at $1300\,^{\circ}\mathrm{C}$ resulted in monophasic $Sr_4Al_{14}O_{25}$ compound. However, at higher temperatures ($1400\,^{\circ}\mathrm{C}$) the $Sr_4Al_{14}O_{25}$ phase partially decomposed with formation of $SrAl_2O_4$ and $SrAl_{12}O_{19}$ impurity phases. As seen from figure 3.21, the monoclinic $SrAl_2O_4$ is already dominant crystalline phase in the samples obtained at 1500–$1600\,^{\circ}\mathrm{C}$.

To prove that single phase $Sr_4Al_{14}O_{25}$ annealing compound has been synthesized at $1300\,^{\circ}\mathrm{C}$, the XRD studies on this sample were performed in detail.

The XRD data obtained by measuring with high resolution diffractometer were analysed using Rietveld refinement method. The original crystallographic data of Wang *et al*. [133] were used as a starting model for Rietveld refinement of X-ray diffraction data collected at room temperature. The refinement smoothly converged to the structure close to the starting model based on X-ray powder diffraction data. The obtained results evidently confirmed that sol-gel derived $Sr_4Al_{14}O_{25}$ sample obtained at $1300\,^{\circ}\mathrm{C}$ using boric acid as a flux in the processing is monophasic (see Fig. 3.22).

The series of cerium-doped $Sr_4Al_{14}O_{25}$:Ce_x samples having different concentrations of Ce were prepared using the same synthesis method using determined optimal synthesis parameters that yield single phase strontium aluminate $Sr_4Al_{14}O_{25}$. As we can see from figure 3.23, it was possible to prepare monophasic $Sr_4Al_{14}O_{25}$:Ce_x samples up to concentration of cerium reaching $x = 0.05$. With further increasing cerium concentration ($x = 0.1$) the diffraction line attributable to the side phase of cerium oxide (CeO_2) appeared in the XRD pattern of the end product. As seen, the intensity of this diffraction line evidently increases with increasing the cerium amount. As a result, the maximum cerium concentration $x = 0.05$ could be introduced without changing phase composition of synthesized product.

Photoluminescence excitation and emission measurements revealed that all $Sr_{4-x}Al_{14}O_{25}$:Ce_x samples had excitation maximum at $\sim 330\,\mathrm{nm}$ and emission spectra had double peak with maxima at $\sim 360\,\mathrm{nm}$ and $\sim 380\,\mathrm{nm}$ (Figure 3.24).

The broad emission band is attributable to [Xe]$5d^1$ – [Xe]$5f^1$ transition of Ce^{3+} ions. It turned out that emission intensity slightly increases with higher concentrations of cerium what is in line with excitation spectra. The highest PL intensity was determined for the sample with $x = 0.0025$. Higher doping concentrations resulted in lower PL intensities because of the concentration quenching. Moreover, the emission maximum of the prepared phosphors is much blue shifted than conventional YAG:Ce phosphors ($560\,\mathrm{nm}$) [221].

3.5 Solid-state synthesis of $Sr_4Al_{14}O_{25}$

Different temperatures and fluxing agents (H_3BO_3, AlF_3, $SrCl_2$) were tested in order to obtain single phase $Sr_4Al_{14}O_{25}$. Some of the results are presented in figure 3.25. In all samples the $Sr_4Al_{14}O_{25}$ phase was formed, but none of these syn-

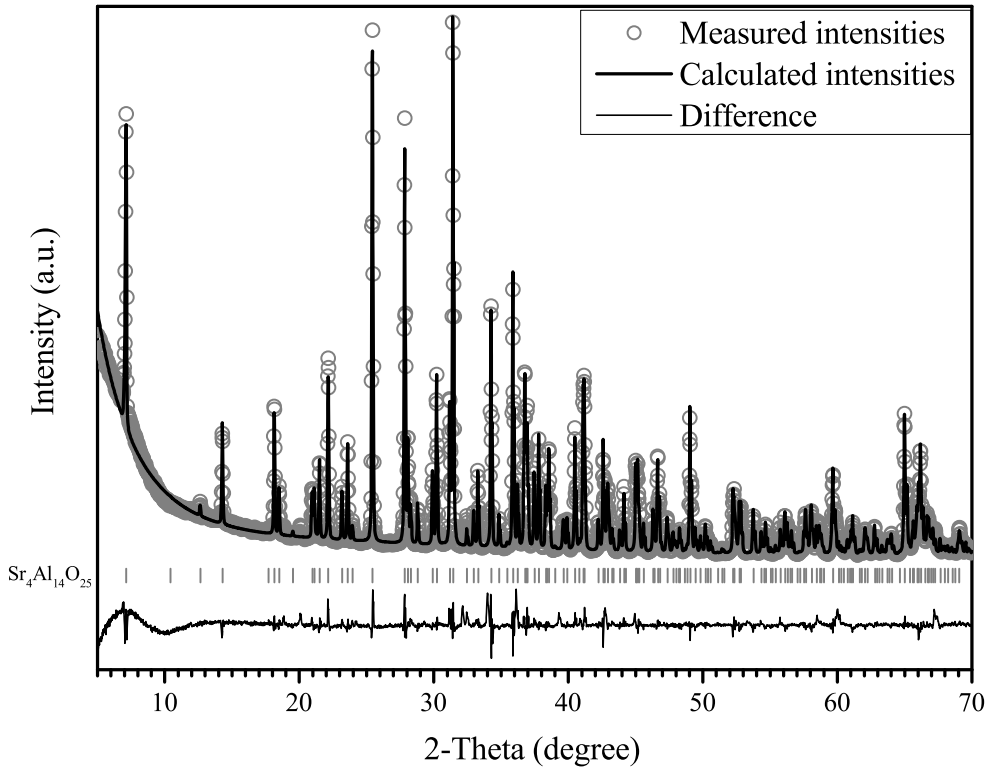

Figure 3.22. The observed (circles) and calculated (solid line) powder XRD patterns of sol-gel derived $Sr_4Al_{14}O_{25}$ sample after Rietveld refinement. The vertical bars located just below the background level indicate calculated positions of Bragg peaks for $K_{\alpha 1}$. The curve the bottom part of the plot represents the difference between observed and calculated intensities. Goodness of fit indicators: $\chi^2 = 3.07$; $R_{wp} = 6.87$.

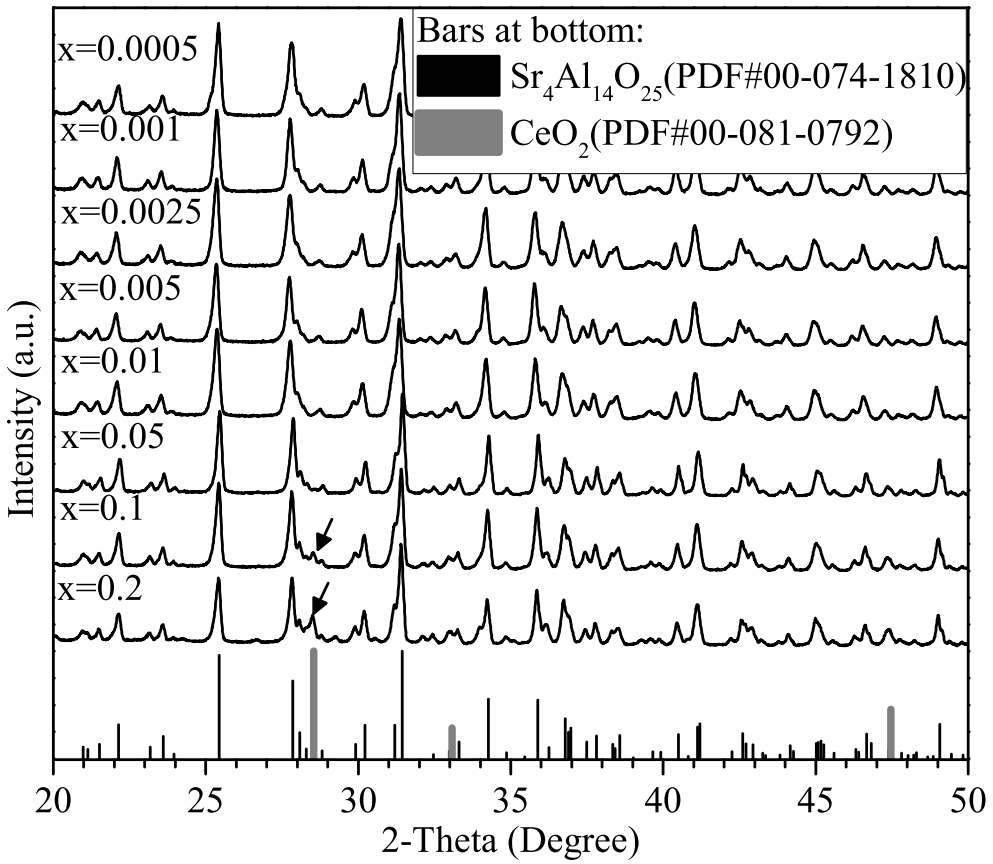

Figure 3.23. XRD patterns of $Sr_{4-x}Al_{14}O_{25}:Ce_x$ samples. The vertical lines at bottom correspond to standard XRD pattern for $Sr_4Al_{14}O_{25}$ and CeO_2 phases.

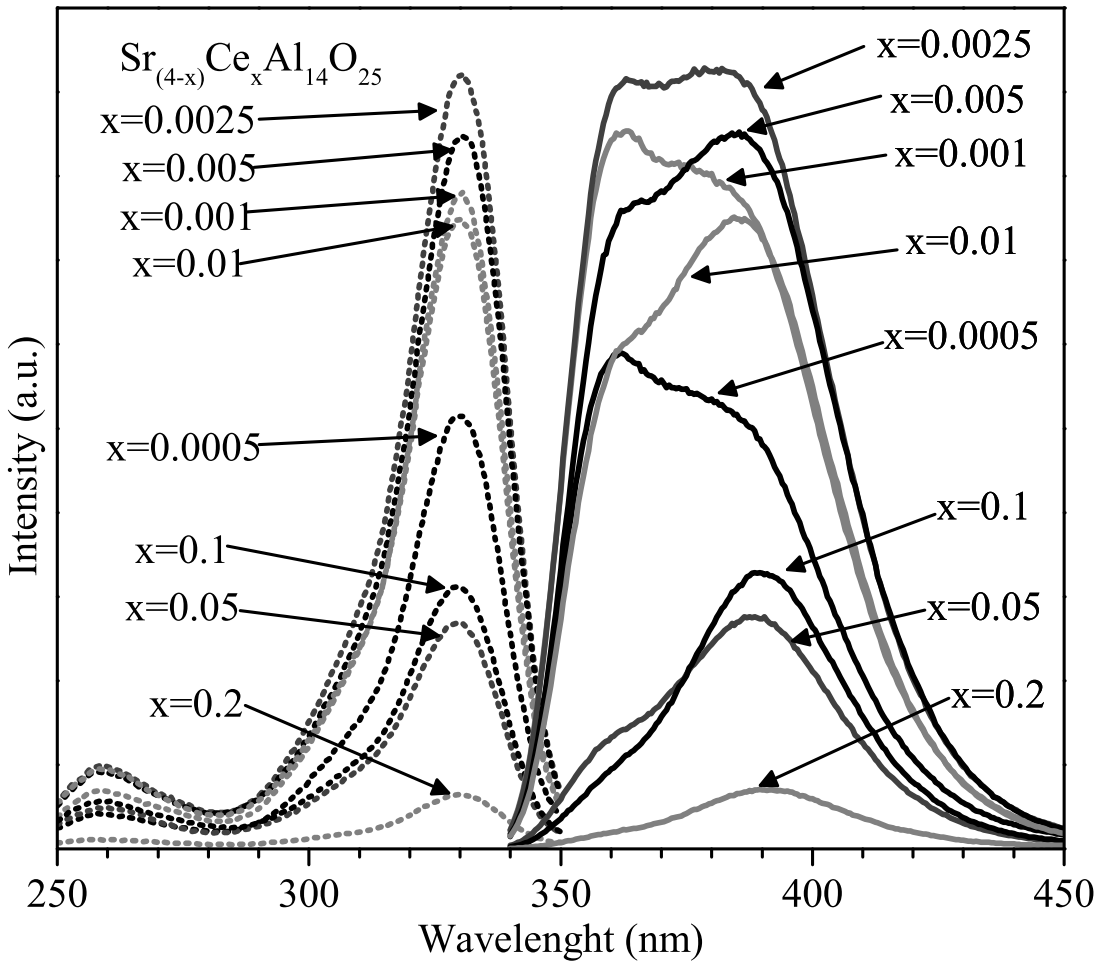

Figure 3.24. Excitation ($\lambda_{em} = 385\,nm$) and emission ($\lambda_{ex} = 330\,nm$) spectra of $Sr_{4-x}Al_{14}O_{25}$:Ce_x samples.

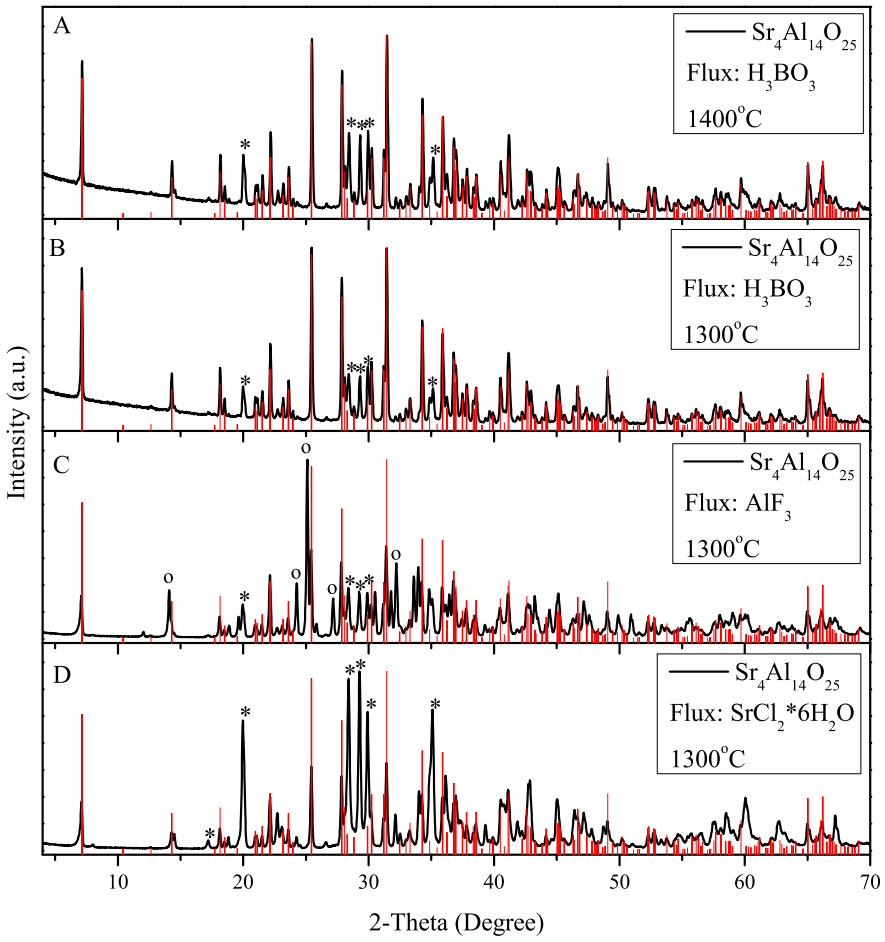

Figure 3.25. XRD patterns of $Sr_4Al_{14}O_{25}$ samples prepared using different fluxing agents: A – 0.1 mol% H_3BO_3 annealed at 1400 °C; B – 0.1 mol% H_3BO_3 annealed at 1300 °C; C – 0.1 mol% AlF_3 annealed at 1300 °C; D – 0.1 mol% $SrCl_2$ annealed at 1300 °C. Vertical bars represents $Sr_4Al_{14}O_{25}$ phase (PDF#01-089-8206); $*$ – represents $SrAl_2O_4$ phase (PDF#04-010-5403); $\circ$ – represents $SrAl_4O_7$ phase (PDF#04-007-5368).

thesis routes produced single phase strontium aluminate $Sr_4Al_{14}O_{25}$. Fig. 3.25 D shows XRD pattern of the sample produced using strontium chloride as a flux. Evidently, that the main crystalline phase in this sample is $SrAl_2O_4$ (most intensive characteristic peaks are marked $*$). The XRD pattern of the sample produced with AlF_3 fluxing agent (Fig. 3.25 C) gives the strongest peaks characteristic to the $SrAl_4O_7$ phase (noted by $\circ$ symbol), but the traces of $SrAl_2O_4$ and $Sr_4Al_{14}O_{25}$ can also be identified.

The syntheses with boric acid used as a fluxing agent produced the best results. However, it was still visible that other phases (mostly $SrAl_2O_4$) were present in

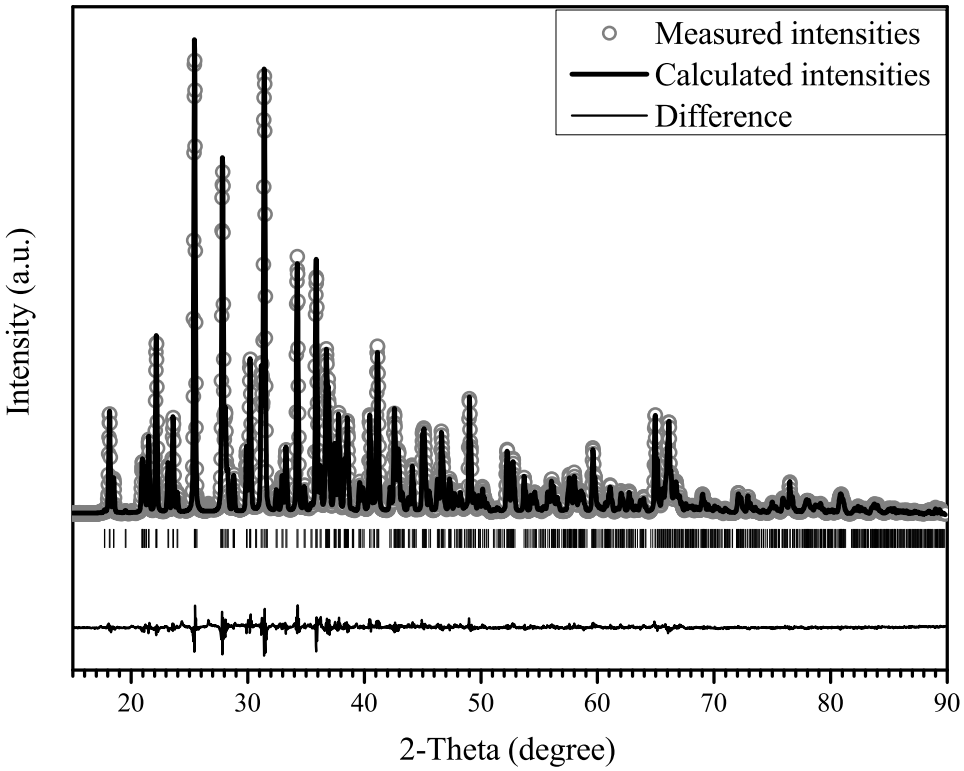

Figure 3.26. X-ray diffraction pattern of $Sr_4Al_{14}O_{25}$ refined employing Rietveld method. Sample prepared using $2.5\,\mathrm{wt}\,\%$ of H_3BO_3 as a fluxing agent.

the synthesis products. With increasing amount of boric acid as a flux ($2.5\,\%$ wt.), the single phase samples have formed. It is evident from figure 3.26 that this sample contains only single phase $Sr_4Al_{14}O_{25}$.

The original crystallographic data of Wang *et al*. [133] was used as a starting model for Rietveld refinement of X-ray diffraction data collected at room temperature employing Rigaku Smartlab diffractometer. The refinement smoothly converged to the structure close to the starting model based on X-ray powder diffraction data. Therefore, it is determined that $Sr_4Al_{14}O_{25}$ phase can be synthesized by the solid state reaction method at $1300\,^{\circ}\mathrm{C}$ for $8\,\mathrm{h}$. The crystallographic details are provided in Table 3.1.

There are several reports that deal with influence of boric acid to luminescence properties [156, 150], and a study on the role of boric acid in the synthesis of calcium aluminate claims that at lower concentrations of H_3BO_3 acts as a fluxing agent, but at higher concentrations it behaves as one of the reactants and produces aluminoborate complexes [222].

Table 3.1. Structural parameters[a] for $Sr_4Al_{14}O_{25}$[b] refined from X-ray powder diffraction data collected at room temperature (orthorhombic space group $Pmma$ (№ 51))

Atom	x	y	z	Biso	Occupancy
Sr1	0.13778(4)	1/2	0.03410(29)	0.653(42)	1/2
Sr2	0.12050(4)	0	0.11412(29)	0.604(39)	1/2
Al1	0.18493(10)	0.19391(32)	0.62819(69)	0.705(85)	1
Al2	0.06618 (9)	0.32226(41)	0.50941(64)	0.258(61)	1
Al3	1/4	0.29568(44)	0.13145(99)	1.004(108)	1/2
Al4	0	0.16716(52)	0	0.325(91)	1/2
Al5	0	0	1/2	0.511(129)	1/4
Al6	0	1/2	0	0.692(145)	1/4
O1	0.04318(17)	0.15995(57)	0.32646(139)	0.178(131)	1
O2	0.13719(19)	0.32013(54)	0.50168(108)	-0.152(114)	1
O3	0.18892(16)	0.23191(63)	-0.02292(96)	0.736(149)	1
O4	1/4	0.23210(81)	0.47352(117)	-0.313(197)	1/2
O5	0.03844(28)	0	0.83407(192)	1.015(211)	1/2
O6	0.05061(25)	1/2	0.33679(174)	0.040(200)	1/2
O7	0.16581(26)	0	0.58172(151)	-0.185(182)	1/2
O8	0.04243(16)	0.33552(57)	0.85534(143)	-0.479(116)	1
O9	1/4	1/2	0.10010	1.100(314)	1/4

.

[a] – Numbers in parentheses are standard deviations of last significant digits. Values with no standard deviation shown were not refined.

[b] – Cell parameters: $a = 24.768\,81(70)$, $b = 8.478\,39(25)$, $c = 4.883\,79(14)$ Å; Figures of merit: $R_p = 5.75\,\%$, $R_wp = 7.46\,\%$, $R_exp = 3.96\,\%$, $\chi^2 = 3.55$

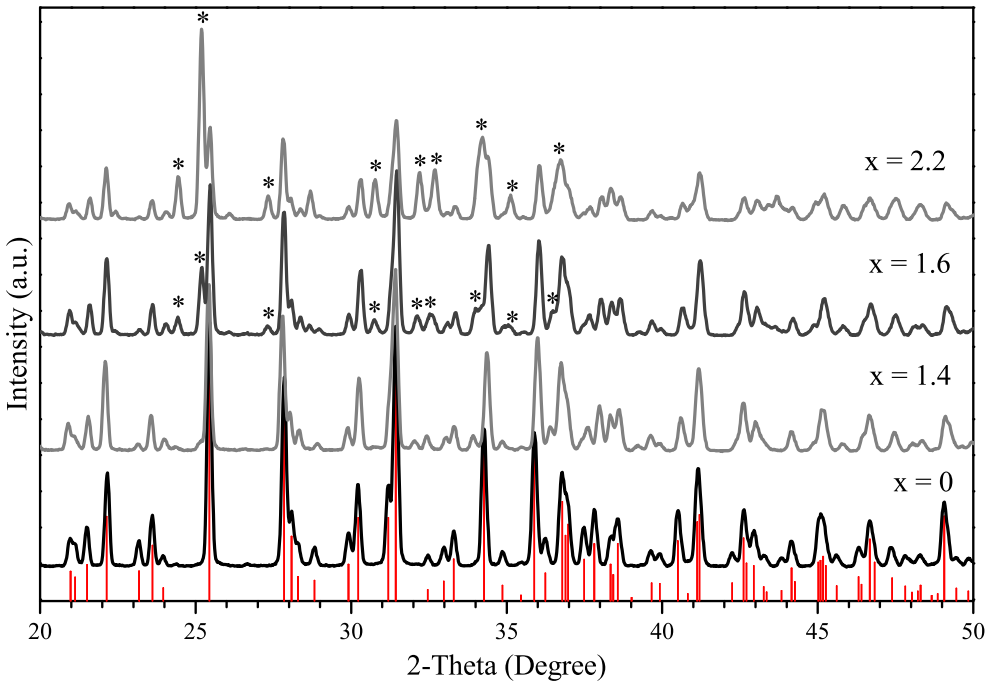

Figure 3.27. XRD patterns of $Sr_{4-x}Ca_xAl_{14}O_{25}$ samples. Vertical bars represents $Sr_4Al_{14}O_{25}$ phase (PDF#01-089-8206).

3.5.1 Partial substitution of Sr^{2+} by Ca^{2+}

To investigate how partial substitution of strontium by calcium alters lattice parameters of $Sr_4Al_{14}O_{25}$, a series of samples $Sr_{4-x}Ca_xAl_{14}O_{25}$ with $x_{Ca} =$ from 0 to 2.2 were prepared. As seen from XRD data (Fig. 3.27), the single phase compounds can be obtained with substitution up to $x_{Ca} = 1.4$. With increasing concentrations of Ca, the secondary phase of $CaAl_4O_7$ is forming.

These results agree with Suriyamurthy et al. study, which claims that at $x_{Ca} = 3.2$ $Sr_4Al_{14}O_{25}$ phase is barely detectable and $CaAl_4O_7$ phase is dominant, also that for $x_{Ca} > 2$, the emission maximum is shifted towards the blue region [150]. This is due to formation of other phases than $Sr_4Al_{14}O_{25}$. (note: x in this report corresponds to $x = \mathrm{Sr}/\mathrm{Ca}$).

Previously refined $Sr_4Al_{14}O_{25}$ data were used as a starting model for Rietveld refinement. The Ca^{2+} ions were introduced to the crystal structure with occupancy of 0 and constrained with Sr^{2+} occupancy of 0.5, by a factor of -1. Crystallographic data of $CaAl_4O_7$ (ICDS#14270) were used for the refinement when second phase was present (samples with $x_{Ca} > 1.4$). Refined lattice parameters a, b, c and cell volume V are summarized in figure 3.28.

As expected, substituting Sr^{2+} with Ca^{2+} (ionic radii 117 and $99\,\mathrm{pm}$, respec-

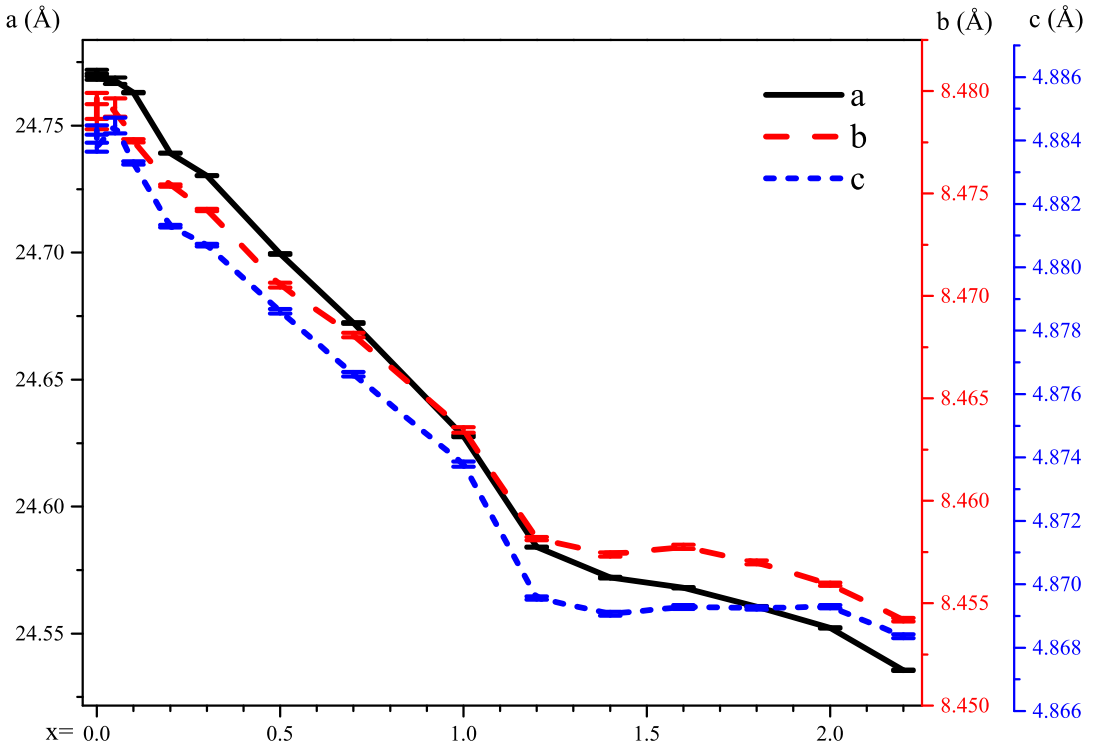

Figure 3.28. Refined structural parameters for $Sr_{4-x}Ca_xAl_{14}O_{25}$, where x = from 0 to 2.2 (presented on x axis in all diagrams).

tively) the unit cell volume and lattice parameters monotonically decreases. The changes slow down when the critical Ca^{2+} concentration is reached and it is not possible to obtain the single phase compounds.

Table 3.2 summarizes refined occupancies of all $Sr_{4-x}Ca_xAl_{14}O_{25}$ samples. Constrains with factor of -1 were used for Sr1–Ca1 and Sr2–Ca2 pairs.

Except for lowest calcium concentrations, Sr2 site is at least two times more likely to be substituted by calcium. As it is visible from Fig. 3.29, Fig. 3.30 and Fig. 3.31, the Sr1 (represented as red circles with squared patterns) sites are surrounded by AlO_4-tetrahedra and the Sr2 (represented as red circles) sites are surrounded by more complex AlO_4-tetrahedra and AlO_6-octahedra system. Sr2 sites are more preferred to be substituted by a smaller Ca^{2+} ion probably because these sites are less spacious than Sr1 sites.

3.5.2 Partial substitution of Sr^{2+} by Ba^{2+}

To investigate how partial substitution of strontium by barium alters lattice parameters of $Sr_4Al_{14}O_{25}$, a series of samples $Sr_{4-x}Ba_xAl_{14}O_{25}$ with x_{Ba} = from 0 to 1 were prepared. As seen from figure 3.32, that barium substitution has much

Table 3.2. Refined[a] occupancies of $Sr_{4-x}Ca_xAl_{14}O_{25}$. (All atoms have multiplicity of 4.)

x=	0	0.05	0.1	0.2	0.3	0.5	0.7
Sr1	0.5	0.468(5)	0.478(4)	0.483(3)	0.473(2)	0.458(4)	0.444(4)
Ca1	0.0	0.032(5)	0.022(4)	0.017(3)	0.027(2)	0.042(4)	0.056(4)
Sr2	0.5	0.487(5)	0.490(4)	0.445(3)	0.436(2)	0.395(4)	0.367(3)
Ca2	0.0	0.013(5)	0.010(4)	0.055(3)	0.064(2)	0.105(4)	0.133(3
x=	1	1.2	1.4	1.6	1.8	2	2.2
Sr1	0.425(5)	0.415(3)	0.405(4)	0.393(3)	0.387(3)	0.370(3)	0.353(5)
Ca1	0.075(5)	0.085(3)	0.095(4)	0.107(3)	0.113(3)	0.130(3)	0.147(5)
Sr2	0.314(4)	0.242(2)	0.238(3)	0.233(3)	0.222(3)	0.220(3)	0.212(4)
Ca2	0.186(4)	0.258(2)	0.262(3)	0.267(3)	0.278(3)	0.280(3)	0.288(4)

[a] – Numbers in parentheses are standard deviations of last significant digits.

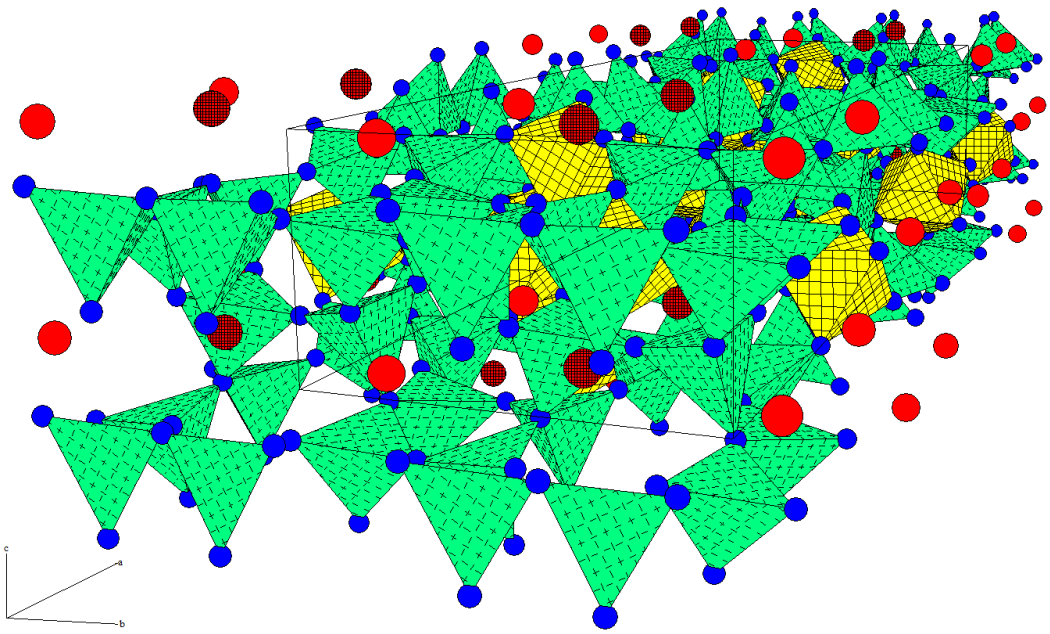

Figure 3.29. Visualization of $Sr_4Al_{14}O_{25}$ crystal structure. Sr1 sites are represented as red circles with squared patterns, Sr2 sites as red circles, oxygen atoms as blue circles, AlO_4 sites as green tetrahedral, AlO_6 sites as yellow octahedral.

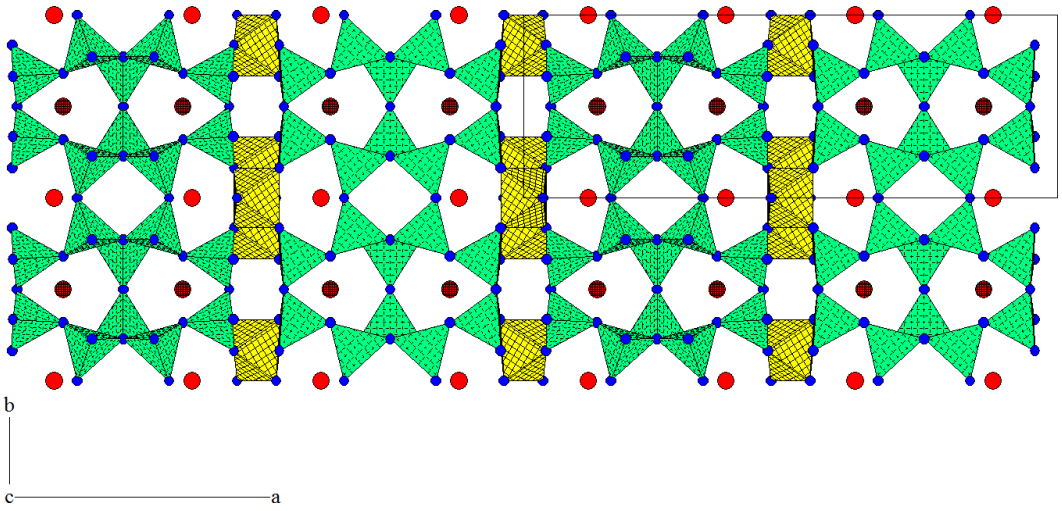

Figure 3.30. Projection of $Sr_4Al_{14}O_{25}$ crystal structure (perpendicular to ab-plane).

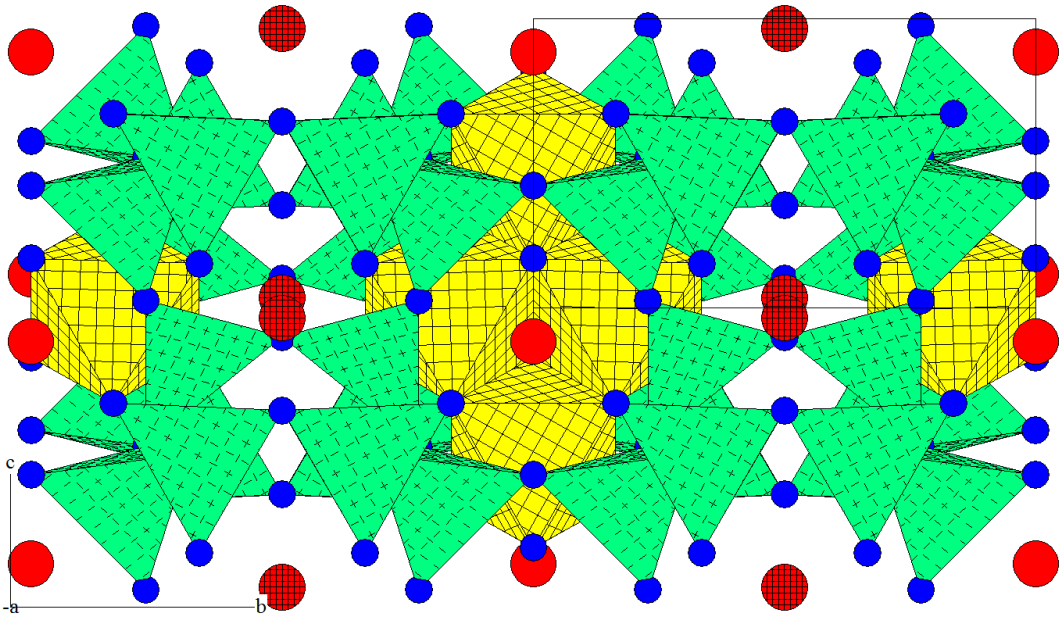

Figure 3.31. Projection of $Sr_4Al_{14}O_{25}$ crystal structure viewed perpendicular to bc-plane.

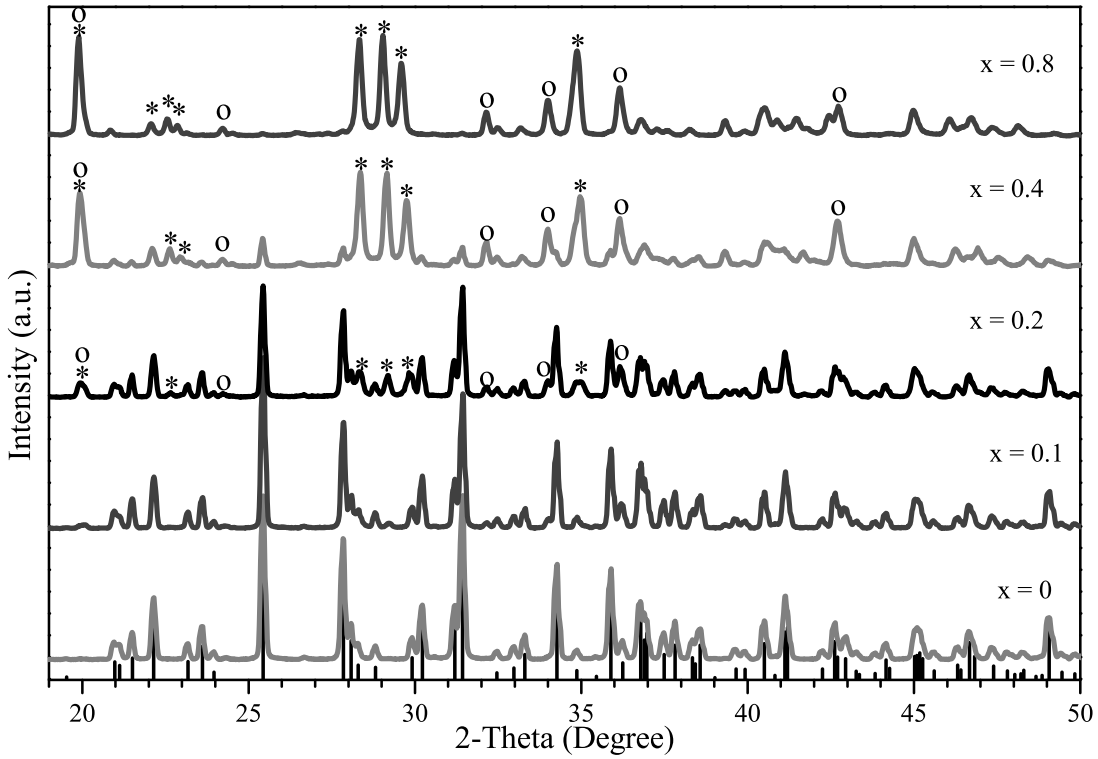

Figure 3.32. XRD patterns of $Sr_{4-x}Ba_xAl_{14}O_{25}$ samples. Vertical bars represents $Sr_4Al_{14}O_{25}$ phase (PDF#01-089-8206).

more expressed effect on the formation of strontium aluminate phase. Much smaller amount of barium in comparison with calcium promotes the formation of side phases. Starting with $x_{\mathrm{Ba}} = 0.2$ the traces of $SrAl_2O_4$ and $SrAl_{12}O_{19}$ are detectable in the XRD patterns. These phases become dominant crystalline phases at higher concentrations of barium substitution. This agrees with previously mentioned study of substitution effects on the luminescence where authors claim that from $x_{\mathrm{Ba}} = 0.4$ to $x_{\mathrm{Ba}} = 1.2$ there are other phases present in addition to $Sr_4Al_{14}O_{25}$ [150].

Previously refined $Sr_4Al_{14}O_{25}$ data were used as a starting model for Rietveld refinement. The Ba^{2+} ions were introduced to crystal structure with occupancy of 0 and constrained with Sr^{2+} occupancy of 0.5, by a factor of -1. Crystallographic data of $SrAl_2O_4$ (ICDS#160296) and $SrAl_{12}O_{19}$ (ICSD#43155) were used for refinement when second phases were present (samples with $x_{\mathrm{Ba}} > 0.1$). The refined lattice parameters are summarized in figure 3.33.

As expected, substituting Sr^{2+} with Ba^{2+} (ionic radii 117 and $135\,\mathrm{pm}$, respectively), the lattice parameters and unit cell volume increase. From the concentration of $x_{\mathrm{Ba}} = 0.4$ and above (not shown) the refinement for $Sr_4Al_{14}O_{25}$ phase

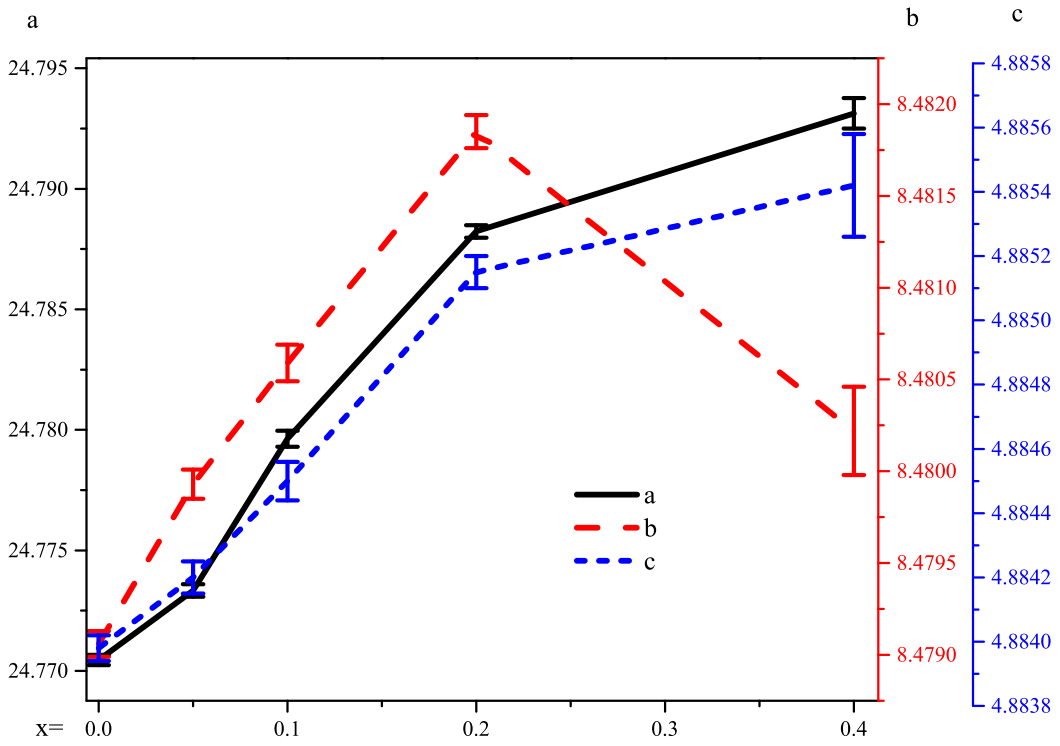

Figure 3.33. Refined structural parameters for $Sr_{4-x}Ba_xAl_{14}O_{25}$, where x = from 0 to 0.4 (presented on x axis in all diagrams).

became very complicated and the uncertainties increased considerably, because the fraction of phase of interest is too small.

Table 3.3 summarizes refined occupancies of $Sr_{4-x}Ba_xAl_{14}O_{25}$ samples. Constrains with factor of -1 were used for Sr1–Ba1 and Sr2–Ba2 pairs.

From this data it seems that Sr1 site is more preferred by barium ions, although more investigation is necessary in order to confirm this assumption. As one can see from Fig. 3.29, Fig. 3.30 and Fig. 3.31, and, Sr1 site is more spacious than Sr2 site, so it seems logical that Ba^{2+}, possessing a larger ionic radius, should

Table 3.3. Refined[a] occupancies of $Sr_{4-x}Ba_xAl_{14}O_{25}$. (All atoms have multiplicity of 4.)

x=	0	0.05	0.1	0.2	0.4
Sr1	0.5	0.488(6)	0.465(7)	0.511(7)	0.424(27)
Ba1	0.0	0.012(6)	0.035(7)	-0.011(7)	0.076(27)
Sr2	0.5	0.510(6)	0.486(7)	0.473(7)	0.523(26)
Ba2	0.0	-0.010(6)	0.014(7)	0.027(7)	-0.023(26)

[a] – Numbers in parentheses are standard deviations of last significant digits.

prefer this site.

3.6 Solid-state and sol-gel synthesis of $SrAl_4O_7$

Different amount of fluxing agent was used during the solid state synthesis of $SrAl_4O_7$. As seen in figure 3.34, the XRD pattern of sample prepared without boric acid consists of broad peaks attributable to $SrAl_2O_4$ phase. The XRD patterns of the samples fabricated with a flux exhibit the formation of $SrAl_4O_7$ as the main crystalline phase. Under closer investigation, it can be seen that the XRD pattern of sample prepared with $2.5\,\%$ of fluxing agent still has distinguishable diffraction peaks belonging to $SrAl_2O_4$ phase (notice the triplet of peaks at $2\theta \approx 30°$). These results suggest that the required amount of boric acid during the synthesis is at least $5\,\%$ by weight.

Moreover, the sol-gel synthesis route was also used in order to prepare the monophasic aluminate samples. In figures 3.35 and 3.36 the XRD patterns of sol-gel derived $SrAl_4O_7$ samples using 1,2-ethandiol or glycerol as complexing agent in the processing and different amount of boric acid are shown. Although the synthesis of $SrAl_4O_7$ using sol-gel route was successful, only one attempt yielded monophasic compound. The monophasic $SrAl_4O_7$ was obtained using glycerol as complexing agent in the sol-gel preparation and adding $1.5\,\%$ of H_3BO_3. Insufficient amount of flux once again resulted in the formation of monoclinic $SrAl_2O_4$ phase. On the other hand, the additional aluminoborate side phase of $SrAl_2B_2O_7$ has formed when an excessive amount of boric acid was used.

It is evident, that the proper amount of fluxing agent is crucial for the formation of monophasic compounds. In the sol-gel synthesis, however, it is difficult to control the gel/flux ratio as the gels might contain different amount of Sr and Al for the same mass of gel since the decomposition of organic part of the gel might differ from sample to sample. Therefore, the solid-state synthesis route was chosen for the future experiments as it yields monophasic compounds more consistently, i.e. the results are reproducible.

Europium-doped samples of $Sr_{0.98}Al_4O_7{:}Eu_{0.02}$ were prepared using solid-state synthesis with different amount of boric acid. Their PL spectra are presented in figure 3.37. Apparently, the photoluminescence of the sample prepared

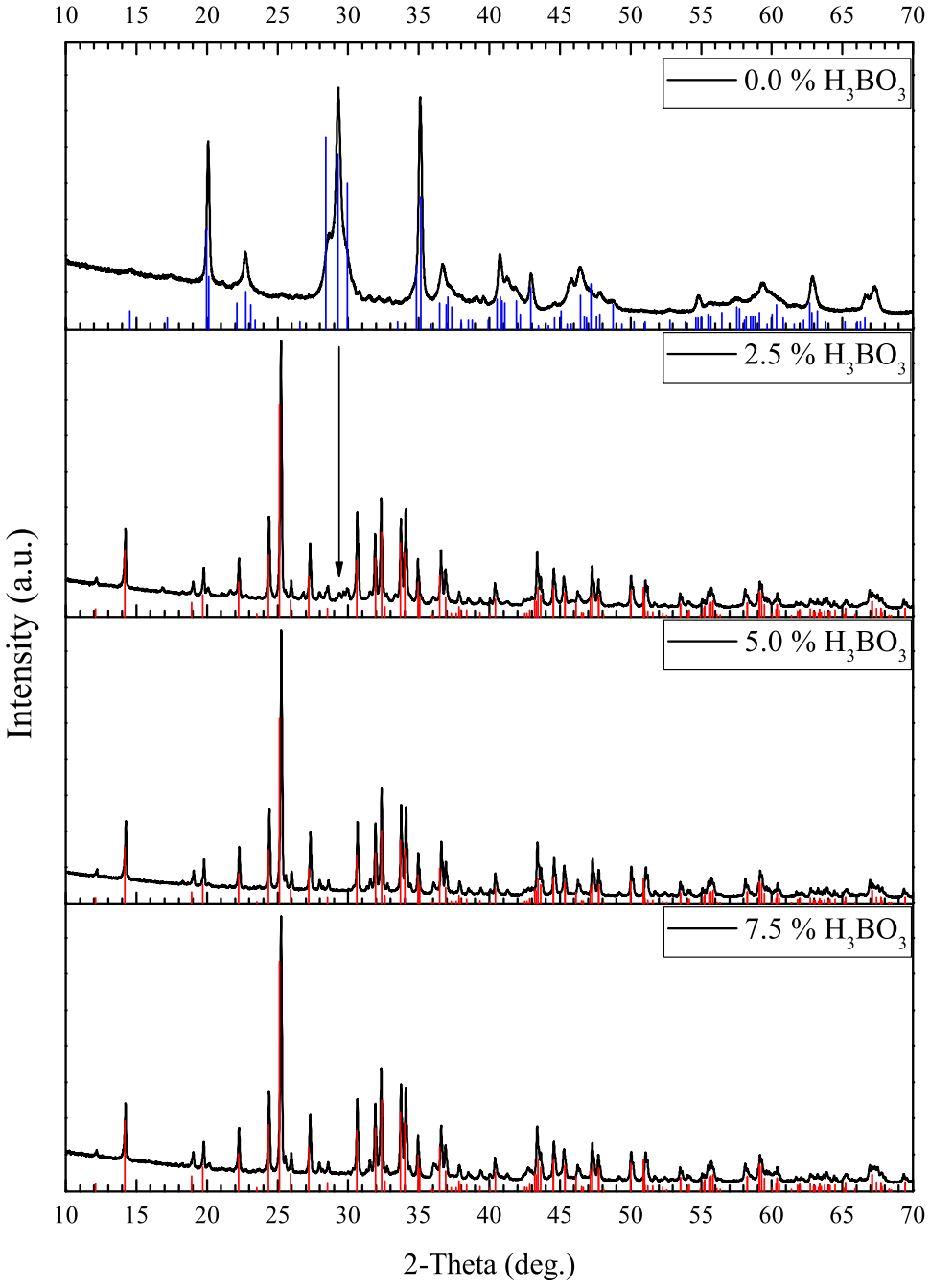

Figure 3.34. XRD patterns of solid state synthesis of $SrAl_4O_7$ samples prepared with different amount of boric acid. Red bars represent $SrAl_4O_7$ (PDF#00-072-1252), blue bars represent $SrAl_2O_4$ (PDF#00-034-0379).

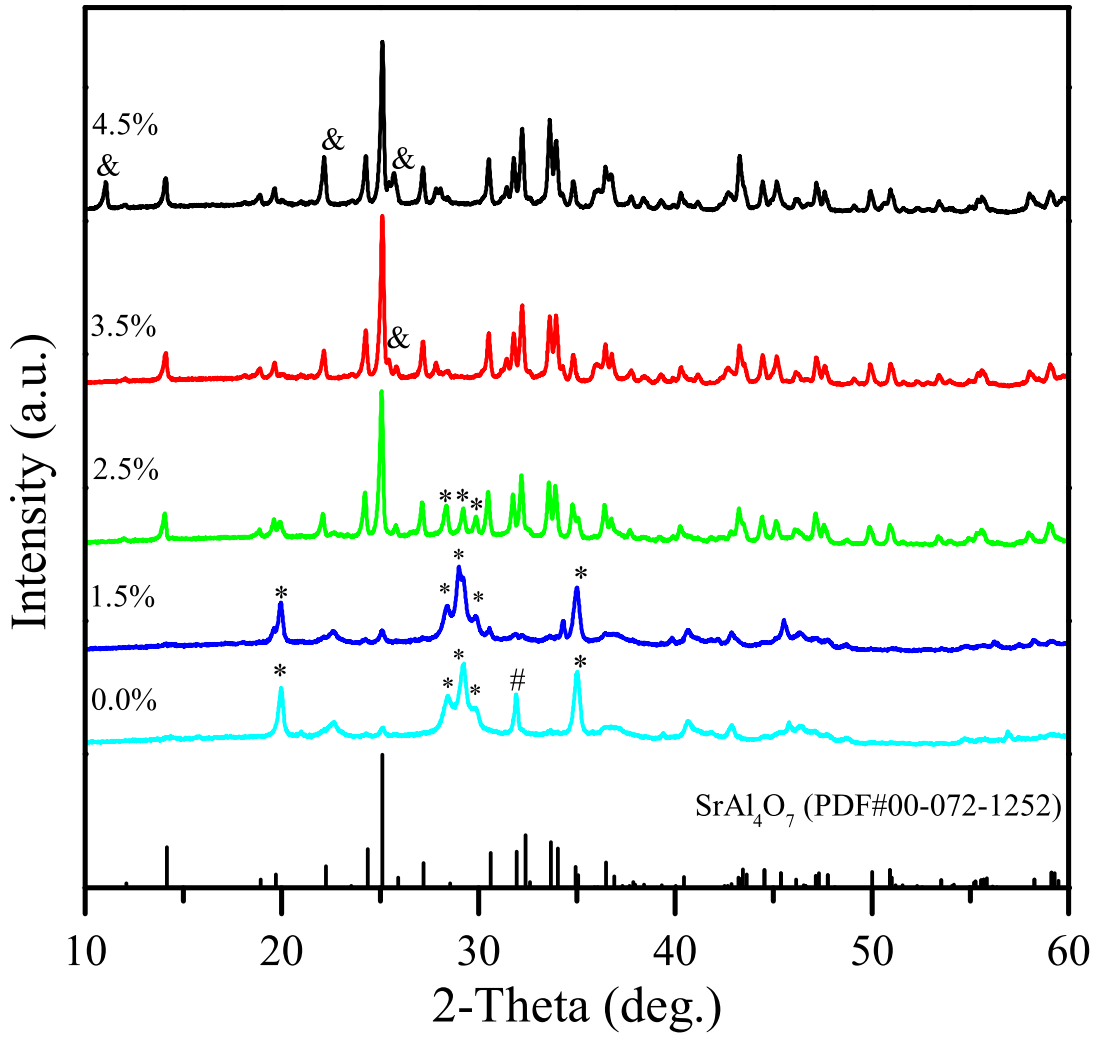

Figure 3.35. XRD patterns of sol-gel derived $SrAl_4O_7$ samples prepared with different amount of boric acid and using 1,2-ethandiol as complexing agent. Black bars represent $SrAl_4O_7$ (PDF#00-072-1252). The crystalline phases are marked: $*$ – $SrAl_2O_4$ (PDF#00-034-0379), & – $SrAl_2B_2O_7$ (PDF#00-047-0182) and # – $Sr_3Al_2O_6$ (PDF#00-024-1187).

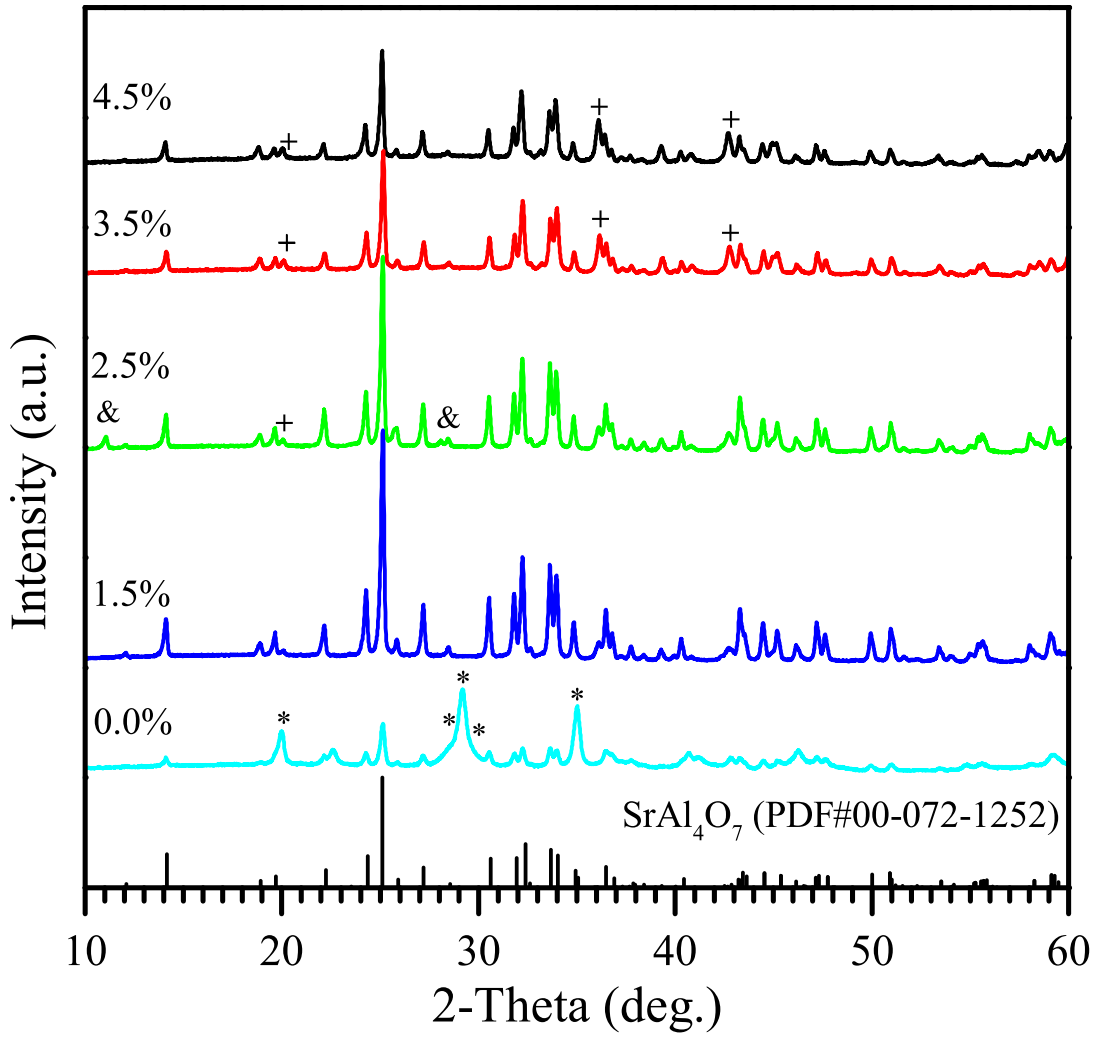

Figure 3.36. XRD patterns of sol-gel derived $SrAl_4O_7$ samples prepared with different amount of boric acid and using glycerol as complexing agent. Black bars represent $SrAl_4O_7$ (PDF#00-072-1252). The crystalline phases are marked: $*$ – $SrAl_2O_4$ (PDF#00-034-0379), & – $SrAl_2B_2O_7$ (PDF#00-047-0182) and $+$ – $SrAl_{12}O_{19}$ (PDF#00-070-0947).

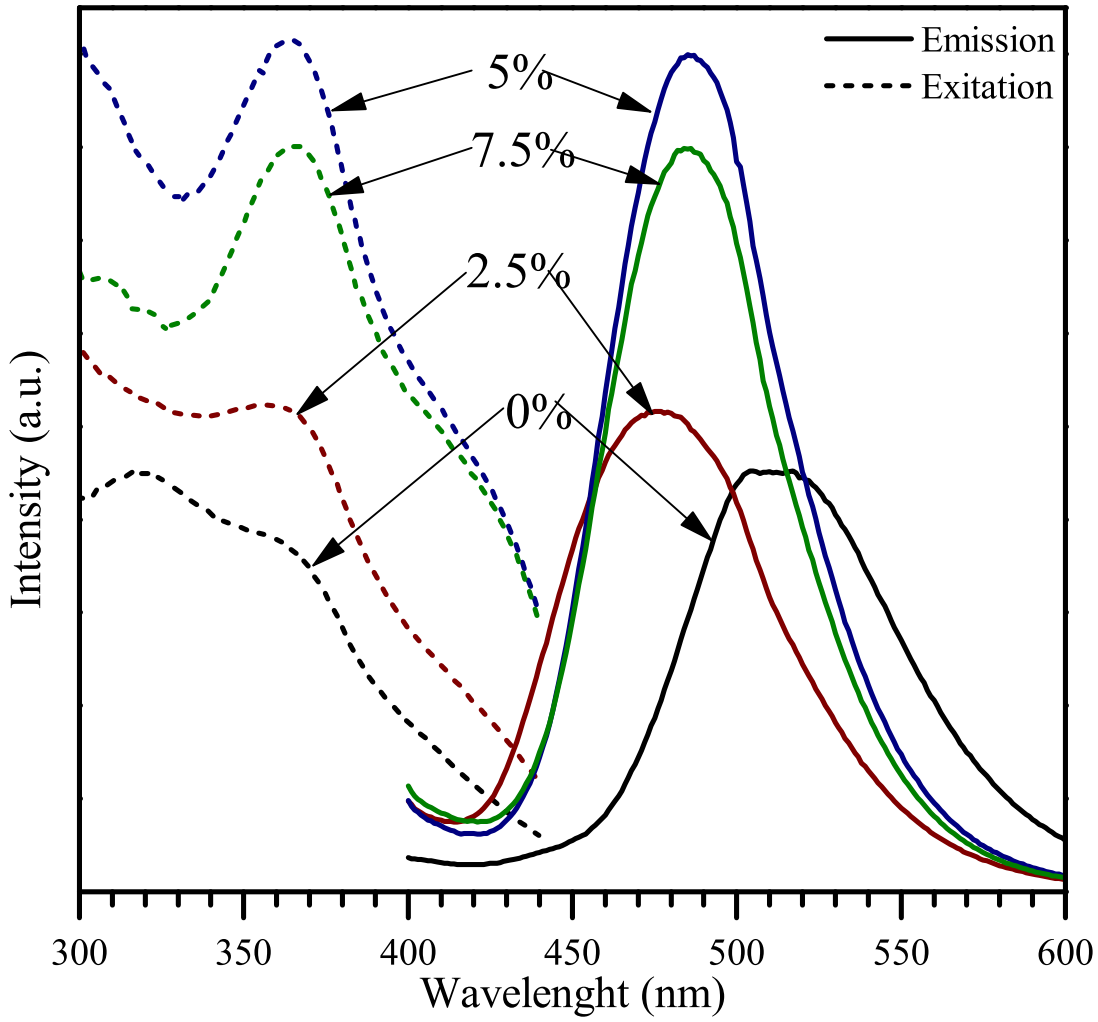

Figure 3.37. Excitation ($\lambda_{em} = 485\,nm$) and emission ($\lambda_{ex} = 370\,nm$) spectra of $SrAl_4O_7$:$Eu_{0.02}$ samples prepared by solid state synthesis using different amount of boric acid.

with $5\,\%$ addition of fluxing agent is the most intensive. As established previously, this amount of boric acid is sufficient for the synthesis of monophasic $SrAl_4O_7$. The PL spectrum of the sample prepared without a flux exhibits emission profile strongly different from the rest because of this synthesis resulted in the formation of $SrAl_2O_4$ compound.

According to the results published on other strontium aluminate phases [11, 137], the co-doping with dysprosium increases the photoluminescence and afterglow of europium. Firstly, the optimal ratio of co-dopants was determined by preparing the samples of $SrAl_4O_7$:Eu,Dy with Eu to Dy ratio of $1:1$, $1:2$ and $1:3$. As seen in figure 3.38, the sample with molar ratio of $\mathrm{Eu}:\mathrm{Dy} = 1:2$ exhibits the most intensive photoluminescence.

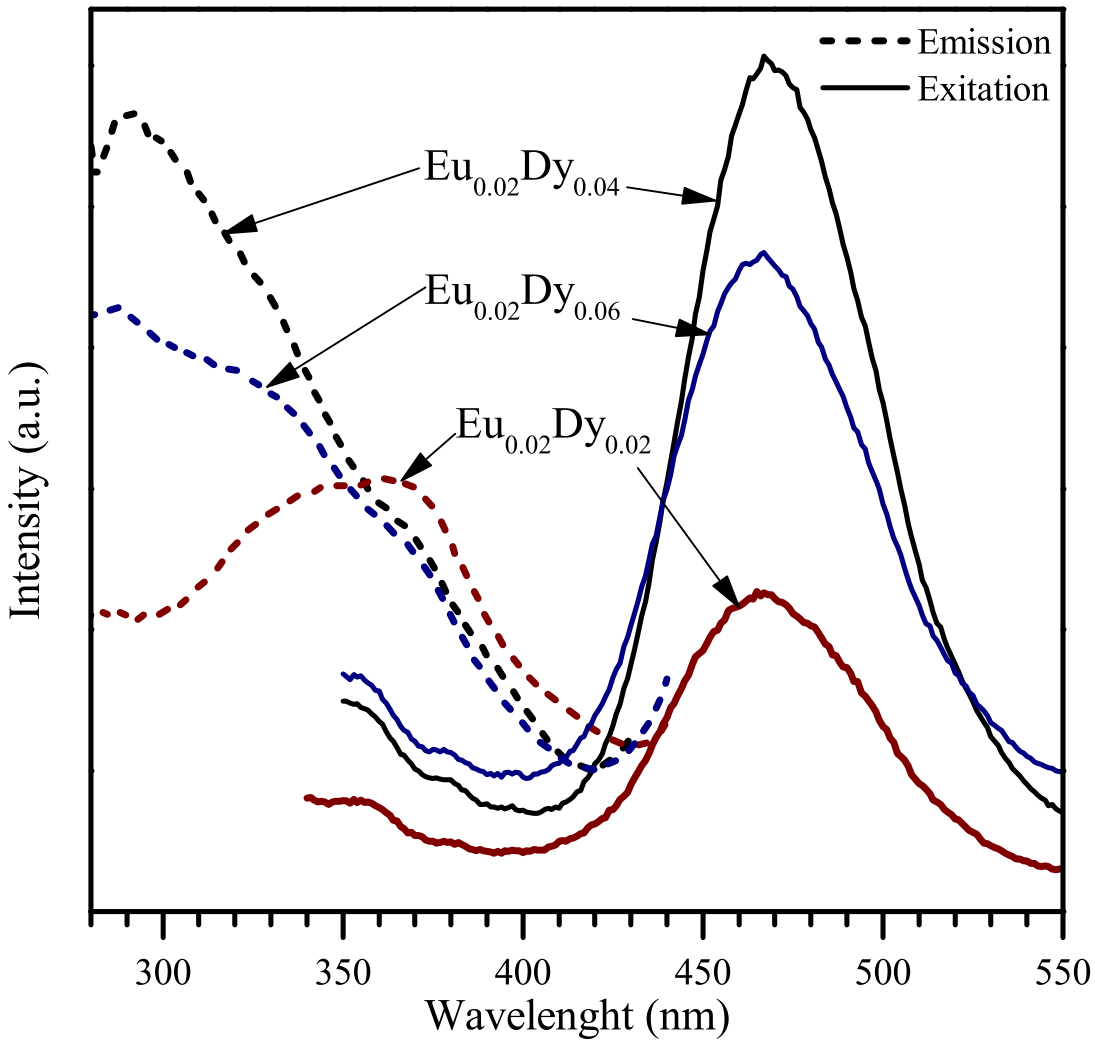

Figure 3.38. Excitation ($\lambda_{em} = 467\,nm$) and emission ($\lambda_{ex} = 291\,nm$) spectra of $SrAl_4O_7$:$Eu_{0.02}$,Dy_x samples prepared by solid state synthesis.

The initial doping of europium was 0.02 parts per mole. This amount was chosen according to the literature on other strontium aluminates [223, 61]. The samples with higher doping concentration of europium while keeping ratio of $Eu : Dy$ fixed to $1 : 2$ were also prepared. The PL spectra of obtained samples are given in figure 3.39. Evidently, with increasing level of Eu^{2+} doping the intensity of photoluminescence decreases due to concentration quenching.

In conclusion, the $SrAl_4O_7$:$Eu_{0.02}$,$Dy_{0.04}$ sample prepared by solid-state synthesis shows the most intensive photoluminescence. Moreover, all Eu-doped and Eu,Dy-co-doped samples exhibit afterglow visible by the naked eye. The measurements of this property are currently under investigation.

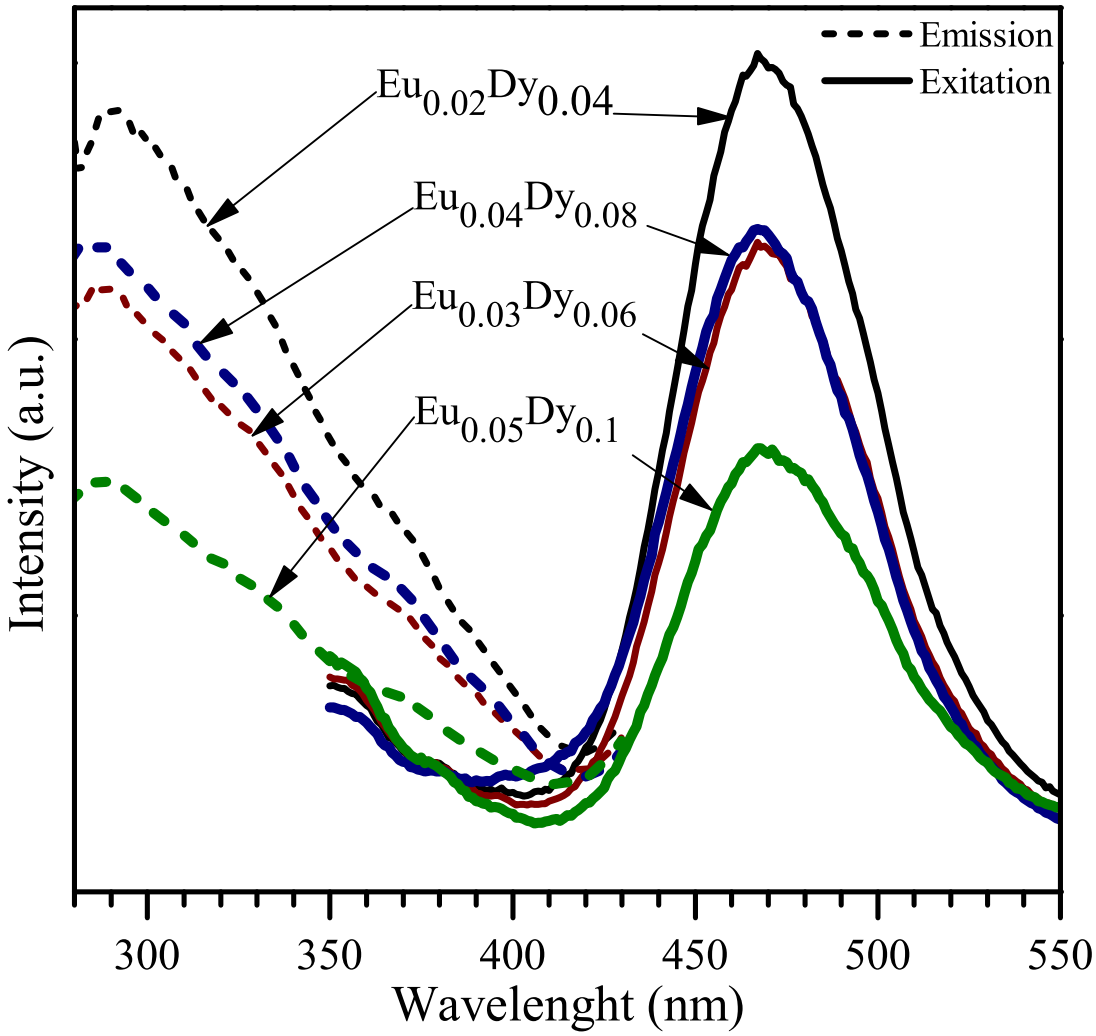

Figure 3.39. Excitation ($\lambda_{em} = 467\,nm$) and emission ($\lambda_{ex} = 291\,nm$) spectra of $SrAl_4O_7$:Eu_x,Dy_y samples prepared by solid state synthesis.

Conclusions

1) Monophasic $SrAl_2O_4$ was successfully synthesized using aqueous sol-gel synthesis route after annealing of Sr – Al – O precursor gel at $1200\,^{\circ}\mathrm{C}$ for $10\,\mathrm{h}$. SEM analysis revealed the formation of plate-like $SrAl_2O_4$ particles.

2) During the sol-gel synthesis of cerium-doped $SrAl_2O_4$ a negligible amount of unknown impurity phases has formed when low concentration of Ce (0.25–$1.00\,\mathrm{mol}\%$) was used, and formation of CeO_2 phase was determined with increasing concentration of Ce (2.00–$3.00\,\mathrm{mol}\%$). The $SrAl_2O_4$:Ce_x samples showed absorption of light in UV region, however, no any photoluminescence was detected.

3) $Sr_3Al_2O_6$ phase was also successfully synthesized using aqueous sol-gel synthesis route. However, the closer XRD analysis employing Rietveld method revealed the formation of additional phases. Ce-doped $Sr_3Al_2O_6$ samples exhibited photoluminescence with broad band emission at around $480\,\mathrm{nm}$ with excitation maxima at $268\,\mathrm{nm}$.

4) Monophasic $SrAl_{12}O_{19}$ samples were successfully synthesized using aqueous sol-gel synthesis route after annealing of Sr – Al – O precursor gel at $1500\,^{\circ}\mathrm{C}$. $SrAl_{12}O_{19}$:Ce specimens showed photoluminescence in UV range with excitation and emission maximums peaking around 260 and $317\,\mathrm{nm}$, respectively.

5) Monophasic $Sr_4Al_{14}O_{25}$ was fabricated by sol-gel synthesis at $1300\,^{\circ}\mathrm{C}$ but only using a flux (boric acid). Monophasic $Sr_4Al_{14}O_{25}$:Ce_x samples with $x = 0.00$–0.05 were also prepared using the same sol-gel synthesis route. At higher concentrations of cerium the side phase of ceria has formed.

6) PL measurements revealed that emission spectra of $Sr_4Al_{14}O_{25}$:Ce_x samples shows double peak with maxima around 360 and $380\,\mathrm{nm}$, while excitation maxima is centred around $330\,\mathrm{nm}$. The highest intensity of emission

was observed at $x = 0.0025$. With increasing amount of cerium, the intensity decreased due to concentration quenching.

7) Monophasic $Sr_4Al_{14}O_{25}$ was prepared via conventional solid state reaction route after annealing starting mixture at $1300\,^{\circ}\mathrm{C}$ for $8\,\mathrm{h}$ and $5\,\mathrm{wt}\,\%$ of boric acid as fluxing agent.

8) Partial substitution of Sr by calcium in $Sr_{4-x}Ca_xAl_{14}O_{25}$ and by barium in $Sr_{4-x}Ba_xAl_{14}O_{25}$ was possible up to $x = 1.4$ and $x = 0.1$, respectively. While at higher concentrations the mixtures of different phases were formed.

9) Structural samples revealed that Sr2 site is more likely to be substituted by Ca than Sr1 site, however, in Ba case the observation was opposite. The unit cell parameters decreased in $Sr_{4-x}Ca_xAl_{14}O_{25}$ and increased in $Sr_{4-x}Ba_xAl_{14}O_{25}$ with increasing the substitutional level.

10) An aqueous sol-gel synthesis of $SrAl_4O_7$ resulted in monophasic compound after annealing of $Sr-Al-O$ precursor gel at $950\,^{\circ}\mathrm{C}$. In the sol-gel processing glycerol was used as complexing agent and $1.5\,\%$ of boric acid was added as fluxing agent. The monophasic $SrAl_4O_7$ was prepared at the same temperature and by solid state synthesis when slow heating rate ($0.5\,^{\circ}\mathrm{C}/\mathrm{min}$) and $5\,\mathrm{wt}\,\%$ of boric acid were used.

11) Eu^{2+}-doped and Eu^{2+},Dy^{3+}-co-doped $SrAl_4O_7$ samples prepared via solid state synthesis route were annealed in reducing CO atmosphere. Photoluminescence measurements showed emission maxima at around $470\,\mathrm{nm}$. The highest intensity was achieved when concentration of Eu was 0.02 molar parts and Eu:Dy ratio was $1:2$.

Author's Publications

Author's publications on subject of thesis

1) **M. Misevicius**, O. Scit, I. Grigoraviciute-Puroniene, G. Degutis, I. Bogdanoviciene, A. Kareiva, Sol-gel synthesis and investigation of un-doped and Ce-doped strontium aluminates, *Ceramics International* **38** (2012), p. 5915–5924.
DOI:10.1016/j.ceramint.2012.04.042

2) **M. Misevicius**, J.-E. Jorgensen, A. Kareiva. Sol-Gel Synthesis, Structural and Optical Properties of Cerium-Doped Strontium Aluminates, $Sr_3Al_2O_6$ and $SrAl_{12}O_{19}$. *Materials science (Medžiagotyra)* **19** (2013) p. 438–442.
DOI:http://dx.doi.org/10.5755/j01.ms.19.4.2670

3) **M. Misevicius**, M. Kilmanas, S. Culunlu, S. Sakirzanovas, A.U. Morkan, A. Beganskiene, A. Kareiva, On the sol-gel fabrication and characterization of undoped and cerium-doped $Sr_4Al_{14}O_{25}$. *Journal of Alloys and Compounds*, **614** (2014) p. 44–48.
DOI: 10.1016/j.jallcom.2014.06.037

Contributed publications not included in thesis

1) I. Bogdanoviciene, **M. Misevicius**, A. Kareiva, K.A. Gross, T.C.K. Yang, G.T. Pan, H.W. Fang, J.C. Yang, Sol-Gel Synthesis and Characterization of Lanthanide-Substituted Nanostructured Calcium Hydroxyapatite, *Advances in Science and Technology* **86** (2013), p.22–27.
DOI: 10.4028/www.scientific.net/AST.86.22

2) K.A. Gross, J. Andersons, **M. Misevicius**, J. Svirksts. Traversing phase fields towards nanosized beta tricalcium phosphate. *Key Engineering Materials* **587** (2014) p. 97–100.
DOI:10.4028/www.scientific.net/KEM.587.97

3) M. Skruodiene, **M. Misevicius**, M. Sakalauskaite, A. Katelnikovas, R. Skaudzius. Doping effect of Tb^{3+} ions on luminescence properties of $Y_3Al_5O_{12}$: Cr^{3+} phosphor, *Journal of Luminescence*, **179** (2016), p. 355–360.
DOI: 10.1016/j.jlumin.2016.07.041.

4) M. Janulevicius, P. Marmokas, **M. Misevicius**, J. Grigorjevaite, L. Mikoliunaite, S. Sakirzanovas, A. Katelnikovas. Luminescence and luminescence quenching of highly efficient $Y_2Mo_4O_{15}$:Eu^{3+} phosphors and ceramics, *Scientific reports* **6** (2016), 26098.
DOI:10.1038/srep26098

Conferences participated

1) **M. Misevicius**, A. Kareiva, "Sol-gel Synthesis and Characterization of Various Strontium Aluminates", 1st NFFA summer school, 18–22 July 2016, Barcelona (Spain)

2) **M. Misevicius**. Synthesis of $SrAl_4O_7$ strontium aluminate using aqueous sol-gel method. Nanochemistry and Nanomaterials 2015 : 2nd International Conference of Chemists: Programme and Proceedings of International Conference, 27.

3) **M. Misevičius**, G. Kibildaitė, P. Taborsky, J. Pinkas, A. Kareiva. Synthesis and characterization of $SrAl_4O_7$:Eu^{2+} and $SrAl_4O_7$:Eu^{2+},Dy^{3+} phosphors. 41-oji Lietuvos Nacionalinė Fizikos Konferencija : Programa Ir Pranešimų Tezės, Vilnius, 2015 M. Birželio 17-19 D. Vilnius, Valstybinis Fizinių Ir Technologijos Mokslų Centras, 307.

4) **M. Misevičius**, G. Kibildaitė, A. Kareiva, "Synthesis and characterization of SrAl4O7". Chemistry and Chemical Technology 2015 : International Conference of Lithuanian Chemical Society, Dedicated to Professor Vitas Daukšas on His 80th Birth Anniversary, Vilnius, Lithuania, January 23, 2015 : Programme and Proceedings of the International Conference, 107-109.

5) **M. Misevičius**, J.-E. Jørgensen, A.Kareiva, "Partial Substitution of Sr^{2+} by Ca^{2+} and Ba^{2+} in the Crystal Structure of $Sr_4Al_{14}O_{25}$", Baltic Neutron School, Tartu (Estonia) May 4–8, 2014.

6) **M. Misevicius**, P. Taborsky, J. Pinkas, A. Kareiva, "Luminescence and afterglow properties of Eu doped and Dy co-doped $SrAl_4O_7$", Chemistry and chemical technology: proceedings of the international conference, Kaunas, 25 April 2014. ISSN 2351-5643 p. 72-75.

7) **M. Misevičius**, J-E. Jørgensen, A. Kareiva, "Synthesis and investigation of different strontium aluminates", EcoBalt 2013: 18th international scientific conference, Vilnius, Lithuania, October 25-27, 2013: book of abstracts. ISBN 9786094592416 p. 91.

8) **M. Misevičius**, M. Kilmanas, S. Culunlu, A.U. Morkan, A. Kareiva, "Formation and photoluminescent properties of cerium-doped $Sr_4Al_{14}O_{25}$", The Fourth International Workshop on Advanced Spectroscopy and Optical Materials, 14-19 July 2013, Gdansk, Poland : book of abstracts. p. 85.

9) **M. Misevičius**, M. Kilmanas, S. Culunlu, "Preparation and characterization of undoped and cerium-doped $Sr_4Al_{14}O_{25}$". Nanochemistry and nanomaterials: international conference of young chemists, 7-9 December, 2012, Palanga, Lithuania: conference program and book of abstracts. Vilnius: Vilniaus universitetas, 2012. ISBN 9786094591389. p. 36.

10) **M. Misevičius**, A. Kareiva, „Stroncio aliuminato $Sr_4Al_{14}O_{25}$, dalinai pakeisto Ba ir Ca vietoje Sr, sintezė ir tyrimas". Chemija ir cheminė technologija: studentų mokslinės konferencijos pranešimų medžiaga. Klaipėda, 2012, gegužės 15 d. ISBN 9789955186519 p. 133-136.

11) **M. Misevičius**, J-E. Jørgensen, A. Kareiva, "Synthesis and structural characterization of $Sr_4Al_{14}O_{25}$ with partial substitution of Sr^{2+} by Ca^{2+} and Ba^{2+}". Chemistry and chemical technology of inorganic materials: proceedings of scientific conference. ISSN 2029-9222 p. 5-9.

12) **M. Misevičius**, G. Degutis, I. Grigoravičiūtė-Puronienė, A. Kareiva, "Preparation and characterization of various strontium aluminates". Chemistry 2011: 10th international conference of Lithuanian chemists, Vilnius, 14-15 October, 2011: abstracts. ISBN 9789955634652 p. 83.

Acknowledgements

I would like to express my very great appreciation to Prof. **Aivaras Kareiva** for his patient guidance and valuable support since I joined Sol-Gel group six years ago. His encouragement, advices, example and all the help has been very much appreciated.

I am thankful to Prof. **Jurgis Barkauskas** for his support and advices related to crystal chemistry.

I would like to offer my special thanks to Prof. **Jens-Erik Jørgensen** for not-so-basic introduction to the wonderful world of crystallography during my visit to Aarhus.

My special thanks are extended to Prof. **Jiři Pinkas** and his research group at Masaryk University for quality time and making me feel welcome during my stay in Brno.

I wish to acknowledge dr. **Simas Šakirzanovas**, dr. **Artūras Katelnikovas** and dr. **Ramūnas Skaudžius** for very valuable discussions, especially topics related to luminescence.

I wish to thank all my **friends and colleagues** from Faculty of Chemistry (Vilnius University) for being around, creating friendly atmosphere, discussing science and stuff, working hard together or just having fun.

Finally, I am grateful to my **family** for all the support throughout these years. And my biggest thanks goes to my beloved wife **Akvilė** for enabling me to pursue career in science and for not killing me during last months of my PhD project.

I would like to dedicate this thesis to my twin sons **Margiris** and **Mindaugas** (*names given in alphabetical order*) whose birth coincides with the beginning of this project.

Bibliography

[1] G. Blasse and BC Grabmaier. *Luminescent materials*. Springer Science & Business Media, 1994.

[2] A. Katelnikovas, T. Bareika, P. Vitta, T. Jüstel, H. Winkler, A. Kareiva, A. Žukauskas, and G. Tamulaitis. $Y_{3-x}Mg_2AlSi_2O_{12}$: phosphors – prospective for warm-white light emitting diodes. *Optical Materials*, 32(9):1261–1265, 2010.

[3] Ted X. Sun. Combinatorial search for advanced luminescence materials. *Biotechnology and Bioengineering*, 61(4):193–201, 1999.

[4] A. Toncelli, A. Di Lieto, P. Minguzzi, and M. Tonelli. Discovering energy-transfer paths in laser crystals. *Optics Letters*, 22(15):1165, 1997.

[5] A. Douy and M. Capron. Crystallisation of spray-dried amorphous precursors in the $SrO-Al_2O_3$ system: a DSC study. *Journal of the European Ceramic Society*, 23(12):2075–2081, 2003.

[6] D. Haranath, V. Shanker, H. Chander, and P. Sharma. Tuning of emission colours in strontium aluminate long persisting phosphor. *Journal of Physics D-Applied Physics*, 36(18):2244–2248, 2003.

[7] M. Avdeev, S. Yakovlev, A. A. Yaremchenko, and V.V. Kharton. Transitions between $P2_1$, $P6_3$ and $P6_322$ modifications of $SrAl_2O_4$ by in situ high-temperature X-ray and neutron diffraction. *Journal of Solid State Chemistry*, 180(12):3535–3544, 2007.

[8] Y. H. Lin, Z. L. Tang, and Z. T. Zhang. Preparation of long-afterglow $Sr_4Al_{14}O_{25}$-based luminescent material and its optical properties. *Materials Letters*, 51(1):14–18, 2001.

[9] M. Akiyama, C. N. Xu, H. Matsui, K. Nonaka, and T. Watanabe. Photostimulated luminescence phenomenon of $Sr_4Al_{14}O_{25}$: Eu,Dy using only visible lights. *Journal of Materials Science Letters*, 19(13):1163–1165, 2000.

[10] H. F. Brito, J. Holsa, T. Laamanen, M. Lastusaari, M. Malkamaki, and L. C. V. Rodrigues. Persistent luminescence mechanisms: human imagination at work. *Optical Materials Express*, 2(4):371–381, 2012.

[11] T. Matsuzawa. A new long phosphorescent phosphor with high brightness, $SrAl_2O_4$:Eu^{2+},Dy^{3+}. *Journal of The Electrochemical Society*, 143(8):2670, 1996.

[12] F. Clabau, X. Rocquefelte, S. Jobic, P. Deniard, M. H. Whangbo, A. Garcia, and T. Le Mercier. Mechanism of phosphorescence appropriate for the long-lasting phosphors Eu^{2+}-doped $SrAl_2O_4$ with codopants Dy^{3+} and B^{3+}. *Chemistry of Materials*, 17(15):3904–3912, 2005.

[13] K. Van den Eeckhout, P. F. Smet, and D. Poelman. Persistent luminescence in Eu^{2+}-doped compounds: A review. *Materials*, 3(4):2536–2566, 2010.

[14] K. Van den Eeckhout, D. Poelman, and P. Smet. Persistent luminescence in non-Eu^{2+}-doped compounds: A review. *Materials*, 6(7):2789–2818, 2013.

[15] F. Massazza. The system $SrO-Al_2O_3$. *Chim. Ind.(Milan)*, 41:108–115, 1959.

[16] F Ganits, T Yu Chemekova, and Yu P Udalov. The $SrO-Al_2O_3$ system. *Zhurnal Neorganicheskoj Khimii*, 24(2):471–475, 1979.

[17] X. Ye, W. Zhuang, J. Wang, W. Yuan, and Z. Qiao. Thermodynamic description of $SrO-Al_2O_3$ system and comparison with similar systems. *Journal of Phase Equilibria and Diffusion*, 28(4):362–368, 2007.

[18] M. L. Capron and A. Douy. Strontium dialuminate $SrAl_4O_7$: Synthesis and stability. *Journal of the American Ceramic Society*, 85(12):3036–3040, 2002.

[19] O. Yamaguchi, A. Narai, and K. Shimizu. New compound in the system $SrO-Al_2O_3$. *Journal of the American Ceramic Society*, 69(2):C–36–C–37, 1986.

[20] V. Kahlenberg. Synthesis and crystal structure of $Sr_{10}Al_6O_{19}$: a derivative of the perovskite structure type in the system $SrO-Al_2O_3$. *Materials Research Bulletin*, 37(4):715–726, 2002.

[21] T. Takeda, K. Takahashi, K. Uheda, H. Takizawa, and T. Endo. Crystal structure and luminescence properties of $Sr_2Al_6O_{11}$:Eu^{2+}. *Journal of the Japan Society of Powder and Powder Metallurgy*, 49(12):1128–1133, 2002.

[22] N.N. Nevskij, L.D. Glasser, V.V. Ilyukhin, and N.V. Belov. Crystal structure of simplest strontium aluminate with three-dimensional skeleton. *Doklady Akademii Nauk SSSR*, 241(4):821–824, 1978.

[23] K. Hayashi, N. Ueda, S. Matsuishi, M. Hirano, T. Kamiya, and H. Hosono. Solid state syntheses of $12\,SrO \cdot 7\,Al_2O_3$ and formation of high density oxygen radical anions, O^- and O^{2-}. *Chemistry of Materials*, 20(19):5987–5996, 2008.

[24] M. Miyakawa, N. Ueda, T. Kamiya, M. Hirano, and H. Hosono. Novel room temperature stable electride $12\,SrO \cdot 7\,Al_2O_3$ thin films: Fabrication, optical and electron transport properties. *Journal of the Ceramic Society of Japan*, 115(1345):567–570, 2007.

[25] M. Miyakawa, H. Hiramatsu, T. Kamiya, M. Hirano, and H. Hosono. Fabrication and electron transport properties of epitaxial films of electron-doped $12\,CaO \cdot 7\,Al_2O_3$ and $12\,SrO \cdot 7\,Al_2O_3$. *Journal of Solid State Chemistry*, 183(2):385–391, 2010.

[26] H. Iida, K. Noguchi, T. Numa, A. Igarashi, and K. Okumura. $Ru/12\,SrO-7\,Al_2O_3$ (S12A7) catalyst prepared by physical mixing with Ru $(PPh_3)_3Cl_2$ for steam reforming of toluene. *Catalysis Communications*, 72:101–104, 2015.

[27] H. Iida, N. Onuki, T. Numa, and A. Igarashi. Steam reforming of dodecane and toluene over $Ru/12\,SrO-7\,Al_2O_3$ (S12A7) catalysts. *Fuel Processing Technology*, 142:397–402, 2016.

[28] C. Li, M. Wang, F. Dai, and K. Suzuki. New nickel-based material ($Sr_{12}Al_{14}O_{33}$) for biomass tar steam reforming for syngas production. *Journal of Renewable and Sustainable Energy*, 5(4):043106, 2013.

[29] B. Smets, G. Hoeks J. Rutten, and J. Verlijsdonk. $SrO \cdot 3\,Al_2O_3{:}Eu^{2+}$ and $1.29\,(Ba, Ca)O{,}6\,Al_2O_3{:}Eu^{2+}$. *Journal of The Electrochemical Society*, 136(7):2119, 1989.

[30] D. Wang and M. Wang. Research on the phase composition and microstructure of high-efficient phosphor $Sr_2Al_6O_{11}{:}Eu^{2+}$. *Journal of Materials Science Letters*, 18(17):1433–1435, 1999.

[31] N.N. Nevskii, L.D. Glasser, V.V. Ilyukhin, and N.V. Belov. Determination of the crystal structure of strontium aluminate by means of vector subsystems. *Soviet physics, crystallography*, 24(1):93–95, 1979.

[32] H. Akasaka, H. Tada, T. Ooki, A. Nakamura, K. Komatsu, S. Tsuchida, S. Ohshio, N. Nambu, and H. Saitoh. New violet phosphor $Sr_7Al_{12}O_{25}{:}Eu^{2+}$ synthesized from Sr–Al–O:Eu powder mounted on polycrystalline alumina. *Japanese Journal of Applied Physics*, 49(12):122601, 2010.

[33] M.J. Buerger. The stuffed derivatives of the silica structures. *American Mineralogist*, 39(7-8):600–614, 1954.

[34] F. P. Glasser and L. S. Dent Glasser. Crystal chemistry of some AB_2O_4 compounds. *Journal of the American Ceramic Society*, 46(8):377–380, 1963.

[35] S. Ito, S. Banno, K. Suzuki, and M. Inagaki. Phase transition in$SrAl_2O_4$. *Zeitschrift für Physikalische Chemie*, 105(3-4):173–178, 1977.

[36] A. R. Schulze and H.M. Buschbaum. Zur verbindungsbildung von MeO: M_2O_3. IV. zur struktur von monoklinem $SrAl_2O_4$. *Zeitschrift für anorganische und allgemeine Chemie*, 475(4):205–210, 1981.

[37] D. Dutczak, T. Justel, C. Ronda, and A. Meijerink. Eu(2+) luminescence in strontium aluminates. *Physical Chemistry Chemical Physics*, 17(23):15236–49, 2015.

[38] T. Aitasalo, J. Hölsä, H. Jungner, J.-C. Krupa, M. Lastusaari, J. Legendziewicz, and J. Niittykoski. Effect of temperature on the luminescence processes of $SrAl_2O_4$:Eu^{2+}. *Radiation Measurements*, 38(4-6):727–730, 2004.

[39] I. C. Chen and T. M. Chen. Sol-gel synthesis and the effect of boron addition on the phosphorescent properties of $SrAl_2O_4$:Eu^{2+},Dy^{3+} phosphors. *Journal of Materials Research*, 16(3):644–651, 2001.

[40] R. Ianos, R. Istratie, C. Pacurariu, and R. Lazau. Solution combustion synthesis of strontium aluminate, $SrAl_2O_4$, powders: single-fuel versus fuel-mixture approach. *Physical Chemistry Chemical Physics*, 18(2):1150–7, 2016.

[41] T. Katsumata, S. Toyomane, R. Sakai, S. Komuro, and T. Morikawa. Trap levels in Eu-doped $SrAl_2O_4$ phosphor crystals co-doped with rare-earth elements. *Journal of the American Ceramic Society*, 89(3):932–936, 2006.

[42] W. Jia, H. Yuan, L. Lu, H. Liu, and W.M. Yen. Crystal growth and characterization of Eu^{2+},Dy^{3+}:$SrAl_2O_4$ and Eu^{2+},Nd^{3+}:$CaAl_2O_4$ by the LHPG method. *Journal of Crystal Growth*, 200(1-2):179–184, 1999.

[43] J. Geng and Z. Wu. Synthesis of long afterglow $SrAl_2O_4$:Eu^{2+},Dy^{3+} phosphors through microwave route. *Journal of Materials Synthesis and Processing*, 10(5):245–248, 2002.

[44] R. E. Rojas-Hernandez, F. Rubio-Marcos, R. H. Goncalves, M. A. Rodriguez, E. Veron, M. Allix, C. Bessada, and J. F. Fernandez. Original synthetic route to obtain a $SrAl_2O_4$ phosphor by the molten salt method: Insights into the reaction mechanism and enhancement of the persistent luminescence. *Inorganic Chemistry*, 54(20):9896–907, 2015.

[45] K. Song, J.-G. Mo, W. Chen, and K. Feng. Hydrothermal synthesis and luminescence of $SrAl_2O_4$:Eu^{2+}/Yb^{3+} hierarchical nanostructures. *Journal of Materials Science: Materials in Electronics*, 27(1):49–53, 2015.

[46] R. Zheng, L. Xu, W. Qin, J. Chen, B. Dong, L. Zhang, and H. Song. Electrospinning preparation and photoluminescence properties of $SrAl_2O_4$:Ce^{3+} nanowires. *Journal of Materials Science*, 46(23):7517–7524, 2011.

[47] C.-C. Chang, C.-Y. Yang, and C.-H. Lu. Preparation and photoluminescence properties of $Sr_4Al_{14}O_{25}$:Eu^{2+} phosphors synthesized via the microemulsion route. *Journal of Materials Science: Materials in Electronics*, 24(5):1458–1462, 2012.

[48] T. Peng, L. Huajun, H. Yang, and C. Yan. Synthesis of $SrAl_2O_4$:Eu,Dy phosphor nanometer powders by sol-gel processes and its optical properties. *Materials Chemistry and Physics*, 85(1):68–72, 2004.

[49] S.H.M. Poort, W.P. Blokpoel, and G. Blasse. Luminescence of Eu^{2+} in barium and strontium aluminate and gallate. *Chemistry of Materials*, 7(8):1547–1551, 1995.

[50] D.P. Bisen and R. Sharma. Mechanoluminescence properties of sral2 o4 :eu(2+) phosphor by combustion synthesis. *Luminescence*, 31(2):394–400, 2016.

[51] Y.M. Huang and Q. Ma. Long afterglow of trivalent dysprosium doped strontium aluminate. *Journal of Luminescence*, 160:271–275, 2015.

[52] A.K. Choubey, N. Brahme, D. P. Bisen, and S. J. Dhoble. Thermoluminescence of γ-irradiated $SrAl_2O_4$:Dy. *Recent Research in Science and Technology*, 4(8), 2012.

[53] Q. L. Ma, B. G. Zhai, and Y. M. Huang. Dopant concentration-dependent photoluminescence and afterglow of $SrAl_2O_4$:Dy^{3+} phosphors. *Materials Research Innovations*, 19(sup7):s40–s44, 2015.

[54] R. Sharma, D. P. Bisen, and B. P. Chandra. Mechanoluminescence of Dy doped strontium aluminate nanophosphors. *Journal of Luminescence*, 168:49–53, 2015.

[55] I.P. Sahu, D. P. Bisen, N. Brahme, R.K. Tamrakar, and R. Shrivastava. Luminescence studies of dysprosium doped strontium aluminate white light emitting phosphor by combustion route. *Journal of Materials Science: Materials in Electronics*, 26(11):8824–8839, 2015.

[56] N. K. Zurba, I. Bdikin, A. Kholkin, D. Golberg, and J. M. Ferreira. Intercrystalline distal-effect on the afterglow phenomenon in photoluminescent $SrAl_2O_4$:CeIII, Ln nanotube growth. *Nanotechnology*, 21(32):325707, 2010.

[57] Z. Gyori, V. Havasi, D. Madarasz, D. Tatrai, T. Brigancz, G. Szabo, Z. Konya, and A Kukovecz. Luminescence properties of Ho^{3+} co-doped $SrAl_2O_4$:Eu^{2+},Dy^{3+} long-persistent phosphors synthesized with a solid-state method. *Journal of Molecular Structure*, 1044:87–93, 2013.

[58] N. Yu, F. Liu, X. Li, and Z. Pan. Near infrared long-persistent phosphorescence in $SrAl_2O_4$:Eu^{2+},Dy^{3+},Er^{3+} phosphors based on persistent energy transfer. *Applied Physics Letters*, 95(23):231110, 2009.

[59] K.-S. Sohn, S.Y. Seo, Y.N. Kwon, and H.D. Park. Direct observation of crack tip stress field using the mechanoluminescence of $SrAl_2O_4$:(Eu,Dy,Nd). *Journal of the American Ceramic Society*, 85(3):712–714, 2004.

[60] H. Song and D. Chen. Combustion synthesis and luminescence properties of $SrAl_2O_4$:Eu^{2+}, Dy^{3+}, Tb^{3+} phosphor. *Luminescence*, 22(6):554–558, 2007.

[61] X. Lü, W. Shu, Q. Fang, Q. Yu, and X. Xiong. Roles of doping ions in persistent luminescence of $SrAl_2O_4$:Eu^{2+},RE^{3+} phosphors. *Journal of Materials Science*, 42(15):6240–6245, 2007.

[62] D. Jia, X. Wang, W. Jia, and W. M. Yen. Trapping processes of $5d$ electrons in Ce^{3+} doped $SrAl_2O_4$. *Journal of Luminescence*, 122-123:311–314, 2007.

[63] X. Xu, Y. Wang, X. Yu, Y. Li, and Y. Gong. Investigation of Ce – Mn energy transfer in $SrAl_2O_4$:Ce^{3+},Mn^{2+}. *Journal of the American Ceramic Society*, 94(1):160–163, 2011.

[64] A. Lopez, M.G. Silva, E. Baggio-Saitovitch, A.R. Camara, R.N. Silveira, and R.J.M. Fonseca. Luminescence of $SrAl_2O_4$:Cr^{3+}. *Journal of Materials Science*, 43(2):464–468, 2007.

[65] S. Chawla, N. Kumar, and H. Chander. Broad yellow orange emission from $SrAl_2O_4$:Pr^{3+} phosphor with blue excitation for application to white LEDs. *Journal of Luminescence*, 129(2):114–118, 2009.

[66] Z. L. Fu, S. H. Zhou, and S. Y. Zhang. Study on optical properties of rare-earth ions in nanocrystalline monoclinic $SrAl_2O_4$: Ln (Ln = Ce^{3+}, Pr^{3+}, Tb^{3+}). *Journal of Physical Chemistry B*, 109(30):14396–14400, 2005.

[67] N. Rakov, R. B. Guimarães, and G. S. Maciel. Infrared-to-visible frequency up-conversion in $SrAl_2O_4$ powders containing Er^{3+} and Yb^{3+}. *Applied Physics B*, 98(2-3):435–438, 2009.

[68] K. Lagerqvist, S. Wallmark, and A. Westgren. Röntgenuntersuchung der system $CaO-Al_2O_3$ und $SrO-Al_2O_3$. *Zeitschrift für anorganische und allgemeine Chemie*, 234(1):1–16, 1937.

[69] F. P. Glasser. Polymorphism of $Ba_3Al_2O_6$ and solid solution between $Ba_3Al_2O_6$, $Sr_3Al_2O_6$ and $Ca_3Al_2O_6$. *Cement and Concrete Research*, 4(5):745–752, 1974.

[70] J. A. Alonso, I. Rasines, and J. L. Soubeyroux. Tristrontium dialuminum hexaoxide: an intricate superstructure of perovskite. *Inorganic Chemistry*, 29(23):4768–4771, 1990.

[71] B. C. Chakoumakos, G. A. Lager, and J. A. Fernandez-Baca. Refinement of the structures of $Sr_3Al_2O_6$ and the hydrogarnet $Sr_3Al_2(O_4D_4)_3$ by Rietveld analysis of neutron powder diffraction data. *Acta Crystallographica Section C Crystal Structure Communications*, 48(3):414–419, 1992.

[72] A. K. Prodjosantoso, B.J. Kennedy, and B.A. Hunter. Synthesis and structural studies of strontium-substituted tricalcium aluminate $Ca_{3-x}Sr_xAl_2O_6$. *Australian Journal of Chemistry*, 53(3):195, 2000.

[73] A. K. Prodjosantoso, B. J. Kennedy, and B. A. Hunter. Phase separation induced by hydration of the mixed Ca/Sr aluminates $Ca_{3-x}Sr_xAl_2O_6$ – a crystallographic study. *Cement and Concrete Research*, 32(4):647–655, 2002.

[74] T. Katsumata, K. Sasajima, T. Nabae, S. Komuro, and T. Morikawa. Characteristics of strontium aluminate crystals used for longâĂŘduration phosphors. *Journal of the American Ceramic Society*, 81(2):413–416, 1998.

[75] P. Zhang, M. Xu, Z. Zheng, B. Sun, and Y. Zhang. Microwave synthesis and characterization of new red long afterglow phosphor $Sr_3Al_2O_6$:Eu. *Transactions of Nonferrous Metals Society of China*, 16:s423–s425, 2006.

[76] Y. Xu, P. Lu, G. Huang, and C. Zeng. Synthesis of $SrAl_4O_7$ via citric acid precursor. *Materials Chemistry and Physics*, 95(1):62–66, 2006.

[77] P. Zhang, M. Xu, Z. Zheng, L. Liu, and L. Li. Synthesis and characterization of europium-doped $Sr_3Al_2O_6$ phosphors by sol-gel technique. *Journal of Sol-Gel Science and Technology*, 43(1):59–64, 2007.

[78] S.K. Sharma, S.S. Pitale, M.M. Malik, R.N. Dubey, and M.S. Qureshi. Synthesis and detailed kinetic analysis using computerized glow-curve deconvolution technique of nanocrystalline $Sr_3Al_2O_6:Pr^{3+}$ – a new phosphor for uv applications. *physica status solidi (a)*, 205(11):2695–2703, 2008.

[79] H.M. Gao, F.Y. Yan, and L. He. Synthesis and luminescence property of $Sr_3Al_2O_6:Eu^{3+}$ red phosphor prepared by co-precipitation technique. *Advanced Materials Research*, 1096:486–491, 2015.

[80] X. Li, H. Pan, A. Tang, J. Zhang, L. Guan, H. Su, G. Dong, Z. Yang, H. Wang, and F. Teng. Hydrothermal synthesis and luminescent properties of Eu^{3+} doped $Sr_3Al_2O_6$ phosphor for white LED. *Journal of Nanoscience and Nanotechnology*, 16(4):3474–3479, 2016.

[81] P. Zhang, M. Xu, Z. Zheng, B. Sun, and Y. Zhang. Rapid formation of red long afterglow phosphor $Sr_3Al_2O_6:Eu^{2+}$, Dy^{3+} by microwave irradiation. *Materials Science and Engineering: B*, 136(2-3):159–164, 2007.

[82] P. Huang, Q. Zhang, C. Cui, and J. Li. Influence of excitation wavelengths on luminescent properties of $Sr_3Al_2O_6:Eu^{2+},Dy^{3+}$ phosphors prepared by sol-gel-combustion processing. *Optical Materials*, 33(8):1252–1257, 2011.

[83] C. Xu and D.Q. Lu. Photoluminescence and afterglow behavior of Eu^{2+}, Dy^{3+} and Eu^{2+}, Sm^{3+} in $Sr_3Al_2O_6$ matrix. *Advanced Materials Research*, 634-638:2493–2497, 2013.

[84] P. Huang, C. Cui, and S. Wang. Influence of calcination temperature on luminescent properties of $Sr_3Al_2O_6:Eu^{2+},Dy^{3+}$ phosphors prepared by sol-gel-combustion processing. *Optical Materials*, 32(1):184–189, 2009.

[85] P. Huang, E. Cui C., and S. Wang. Synthesis and characterization of $Sr_3Al_2O_6:Eu^{2+},Dy^{3+}$ phosphors prepared by sol-gel-combustion processing. *Chinese Physics B*, 18(10):4524, 2009.

[86] C. Chang, W. Li, X. Huang, Z. Wang, X. Chen, X. Qian, R. Guo, Y. Ding, and D. Mao. Photoluminescence and afterglow behavior of Eu^{2+}, Dy^{3+} and Eu^{3+}, Dy^{3+} in $Sr_3Al_2O_6$ matrix. *Journal of Luminescence*, 130(3):347–350, 2010.

[87] H.H. Shin, J.H. Kim, K.P. Kim, B.Y. Han, and J.S. Yoo. Study on the valence state of Eu ions in $Sr_3Al_2O_6$:Eu phosphor. *Japanese Journal of Applied Physics*, 49(4):042601, 2010.

[88] Y. Li, Y. Wang, Y. Xiong, T. Peng, and M. Mo. Effect of electron traps on long afterglow behavior of $Sr_3Al_2O_6$:$Eu_{0.01}{}^{2+}$,$Dy_{0.02-x}{}^{3+}$,$Ho_x{}^{3+}$. *Journal of Rare Earths*, 30(2):105–109, 2012.

[89] Y. Li, Y.H. Wang, Y. Xiong, T.Q. Peng, and M.S. Mo. Luminescent properties, afterglow behavior and thermoluminescence characteristics of (Eu, Dy) doped $Sr_3Al_2O_6$ phosphors. *Applied Mechanics and Materials*, 152-154:198–203, 2012.

[90] A. Yu, D. Zhang, Y. Hu, and R. Yang. Synthesis and characterizations of Dy^{3+} doped $Sr_3Al_2O_6$:Eu^{2+} powder phosphors through citric acid precursor. *Journal of Materials Science: Materials in Electronics*, 25(10):4434–4438, 2014.

[91] M. Akiyama, C.-N. Xu, M. Taira, K. Nonaka, and T. Watanabe. Visualization of stress distribution using mechanoluminescence from $Sr_3Al_2O_6$:Eu and the nature of the luminescence mechanism. *Philosophical Magazine Letters*, 79(9):735–740, 1999.

[92] M. Akiyama, C.-N. Xu, K. Nonaka, and T. Watanabe. Intense visible light emission from $Sr_3Al_2O_6$:Eu,Dy. *Applied Physics Letters*, 73(21):3046, 1998.

[93] P. Zhang, M. Xu, L. Liu, and L. Li. Luminescent properties of $Sr_3Al_2O_6$: Eu, Pr prepared by sol-gel method. *Journal of Sol-Gel Science and Technology*, 50(3):267–270, 2009.

[94] C. Xu, D.Q. Lu, and H.F. Jiang. Influence of different auxiliary activators doping on spectral properties of $Sr_3Al_2O_6$:Eu^{2+} phosphors. *Advanced Materials Research*, 601:54–58, 2012.

[95] G. Li, Y. Lai, T. Cui, H. Yu, D. Liu, and S. Gan. Luminescence properties and charge compensation of $Sr_3Al_2O_6$ doped with Ce^{3+} and alkali metal ions. *Materials Chemistry and Physics*, 124(2-3):1094–1099, 2010.

[96] W. Zhang, F. Liu, S. Feng, S. Hao, Y. Xu, and J. Guan. Synthesis and luminescence of $Sr_3Al_2O_6$:Ce^{3+} powders synthesized by solid state reaction method with addition of H_3BO_3. *Journal of Materials Science: Materials in Electronics*, 25(5):2355–2358, 2014.

[97] V Adelsköld. X-ray studies on magneto-plumbite, $PbO \cdot 6\,Fe_2O_3$, and other substances resembling "beta-alumina", $Na_2O \cdot 11\,Al_2O_3$. *Arkiv for Kemi Mineralogioch Geologi, Series A-12*, 29:1–9, 1938.

[98] A. J. Lindop, C. Matthews, and D. W. Goodwin. The refined structure of $SrO \cdot 6\,Al_2O_3$. *Acta Crystallographica Section B Structural Crystallography and Crystal Chemistry*, 31(12):2940–2941, 1975.

[99] T. R. Wagner and M. O'Keeffe. Bond lengths and valences in aluminates with the magnetoplumbite and β-alumina structures. *Journal of Solid State Chemistry*, 73(1):211–216, 1988.

[100] K. Kimura, M. Ohgaki, K. Tanaka, H. Morikawa, and F. Marumo. Study of the bipyramidal site in magnetoplumbite-like compounds, $SrM_{12}O_{19}$ (m = Al, Fe, Ga). *Journal of Solid State Chemistry*, 87(1):186–194, 1990.

[101] S. R. Jansen, H. T. Hintzen, R. Metselaar, J. W. de Haan, L. J. M. van de Ven, A. P. M. Kentgens, and G. H. Nachtegaal. Multiple quantum Al-27 magic-angle-spinning nuclear magnetic resonance spectroscopic study of $SrAl_{12}O_{19}$: Identification of a Al-27 resonance from a well-defined AlO_5 site. *Journal of Physical Chemistry B*, 102(31):5969–5976, 1998.

[102] J. Li, E.A. Medina, J.K. Stalick, A.W. Sleight, and M. A. Subramanian. Structural studies of $CaAl_{12}O_{19}$, $SrAl_{12}O_{19}$, $La_{2/3+\delta}Al_{12-\delta}O_{19}$, and $CaAl_{10}NiTiO_{19}$ with the hibonite structure; indications of an unusual type of ferroelectricity. *Zeitschrift für Naturforschung B*, 71(5):475–484, 2016.

[103] L. Xie and A. N. Cormack. Defect solid state chemistry of magnetoplumbite structured ceramic oxides. *Journal of Solid State Chemistry*, 83(2):282–291, 1989.

[104] J.M.P.J. Verstegen. A survey of a group of phosphors, based on hexagonal aluminate and gallate host lattices. *Journal of The Electrochemical Society*, 121(12):1623, 1974.

[105] M. N. Baranov, E. F. Kustov, and V. P. Petrov. Crystal field spectra of Nd^{3+} ions in $SrAl_{12}O_{19}$ and $CaSc_2O_4$. *Physica Status Solidi (a)*, 21(2):K123–K125, 1974.

[106] J. S. Choi, S. H. Baek, S. G. Kim, S. H. Lee, H. L. Park, S. I. Mho, T. W. Kim, and Y. H. Hwang. Energy transfer between Ce^{3+} and Eu^{2+} in $SrAl_{12}O_{19}$:$Ce_x{}^{3+}$,$Eu_{0.01}{}^{2+}$ (x =0.01–0.09). *Materials Research Bulletin*, 34(4):551–556, 1999.

[107] S. Huang, L. Lu, W. Jia, X. Wang, W. M. Yen, A. M. Srivastava, and A. A. Setlur. The spectral properties of the $^1s_0$ state in $SrAl_{12}O_{19}$:Pr. *Chemical Physics Letters*, 348(1-2):11–16, 2001.

[108] Y. Xu, W. Peng, S. Wang, X. Xiang, and P. Lu. Synthesis of $SrAl_{12}O_{19}$ via citric acid precursor. *Materials Science and Engineering: B*, 123(2):139–142, 2005.

[109] H. T. Hintzen, C. J. M. Denissen, and H. M. van Noort. ^{151}Eu Mössbauer spectroscopic study of the phosphor $SrAl_{12}O_{19}$:Eu with the magnetoplumbite structure. *Materials Research Bulletin*, 24(2):247–259, 1989.

[110] A. Lupei, V. Lupei, C. Gheorghe, and L. Gheorghe. Cationic distribution and spectral properties of Nd^{3+} in hexa-aluminate. *Advanced Solid-State Photonics*, page 52, 2005.

[111] H. R. Verdun, D. E. Wortman, C. A. Morrison, and J. L. Bradshaw. Optical properties of Nd^{3+} in single crystal $SrAl_{12}O_{19}$. *Optical Materials*, 7(3):117–128, 1997.

[112] W. Yan, Y. Chen, and M. Yin. Quenching mechanism of Er^{3+} emissions in Er^{3+} - and Er^{3+}/Yb^{3+}-doped $SrAl_{12}O_{19}$ nanophosphors. *Journal of Rare Earths*, 29(3):202–206, 2011.

[113] V. Singh and J.-J. Zhu. Synthesis and photoluminescence properties of Er^{3+}, Eu^{3+} ions activated $SrAl_{12}O_{19}$. *International Journal of Modern Physics B*, 20(29):4891–4898, 2006.

[114] L. Wang, Y. Xu, D. Wang, R. Zhou, N. Ding, M. Shi, Y. Chen, Y. Jiang, and Y. Wang. Deep red phosphors $SrAl_{12}O_{19}:Mn^{4+}$,M (M = Li^+, Na^+, K^+, Mg^{2+}) for high colour rendering white LEDs. *physica status solidi (a)*, 210(7):1433–1437, 2013.

[115] D. T. Marzahl, P. W. Metz, C. Krankel, and G. Huber. Spectroscopy and laser operation of Sm(3+)-doped lithium lutetium tetrafluoride ($LiLuF_4$) and strontium hexaaluminate ($SrAl_{12}O_{19}$). *Optics Express*, 23(16):21118–27, 2015.

[116] V. Singh, T. K. Gundu Rao, and J.-J. Zhu. Preparation, luminescence and defect studies of Eu^{2+}-activated strontium hexa-aluminate phosphor prepared via combustion method. *Journal of Solid State Chemistry*, 179(8):2589–2594, 2006.

[117] A. L. N. Stevels and A. D. M. Schrama-de Pauw. Effects of defects on the quantum efficiency of Eu^{2+} -doped aluminates with the magnetoplumbite-type crystal structure. *Journal of Luminescence*, 14(2):147–152, 1976.

[118] J.M.P.J. Verstegen, J.L. Sommerdijk, and A. Bril. Line emission of $SrAl_{12}O_{19}:Eu^{2+}$. *Journal of Luminescence*, 9(5):420–423, 1974.

[119] B. Ma, Q. Guo, M.S. Molokeev, Z. Lv, J. Yao, L. Mei, and Z. Huang. Crystal structure and luminescence properties of green-emitting $Sr_{1-x}Al_{12}O_{19}:xEu^{2+}$ phosphors. *Ceramics International*, 42(5):5995–5999, 2016.

[120] S. Chawla and A. Yadav. Role of valence state of dopant (Eu^{2+}, Eu^{3+}) and growth environment in luminescence and morphology of $SrAl_{12}O_{19}$ nano- and microcrystals. *Materials Chemistry and Physics*, 122(2-3):582–587, 2010.

[121] R. Zhong, J. Zhang, X. Zhang, S. Lu, and X. Wang. Efficient energy transfer and photoluminescent characteristics in $SrAl_{12}O_{19}$:Eu^{2+},Cr^{3+} nano-rods. *Nanotechnology*, 18(44):445707, 2007.

[122] Larry D. Merkle and Bahram Zandi. Spectroscopic studies and laser operation of Pr,Mg:$SrAl_{12}O_{19}$. 79(4):1849–1856, 1997.

[123] B. Zandi, L.D. Merkle, J.B. Gruber, D.E. Wortman, and C.A. Morrison. Optical spectra and analysis for Pr^{3+} in $SrAl_{12}O_{19}$. *Journal of Applied Physics*, 81(3):1047, 1997.

[124] A. M. Srivastava and W. W. Beers. Luminescence of Pr^{3+} in $SrAl_{12}O_{19}$: Observation of two photon luminescence in oxide lattice. *Journal of Luminescence*, 71(4):285–290, 1997.

[125] S. Huang, X. Wang, B. Chen, D. Jia, and W. M. Yen. Photon cascade emission and quantum efficiency of the $^3p_0$ level in Pr^{3+}-doped $SrAl_{12}O_{19}$ system. *Journal of Luminescence*, 102-103:344–348, 2003.

[126] S.M. Loureiro, A. Setlur, W. Heward, S.T. Taylor, H. Comanzo, M. Manoharan, A. Srivastava, P. Schmidt, and U. Happek. First observation of quantum splitting behavior in nanocrystalline $SrAl_{12}O_{19}$:Pr,Mg phosphor. *Chemistry of Materials*, 17(12):3108–3113, 2005.

[127] P. A. Rodnyi, P. Dorenbos, G. B. Stryganyuk, A. S. Voloshinovskii, A. S. Potapov, and C. W. E. van Eijk. Emission of Pr^{3+} in $SrAl_{12}O_{19}$ under vacuum ultraviolet synchrotron excitation. *Journal of Physics-Condensed Matter*, 15(4):719–729, 2003.

[128] F. Reichert, D. T. Marzahl, P. Metz, M. Fechner, N. O. Hansen, and G. Huber. Efficient laser operation of Pr^{3+}, Mg^{2+}:$SrAl_{12}O_{19}$. *Optics Letters*, 37(23):4889–4891, 2012.

[129] F. Reichert, T. Calmano, S. Muller, D. T. Marzahl, P. W. Metz, and G. Huber. Efficient visible laser operation of Pr,Mg:$SrAl_{12}O_{19}$ channel waveguides. *Optics Letters*, 38(15):2698–2701, 2013.

[130] M. Fechner, F. Reichert, N. O. Hansen, K. Petermann, and G. Huber. Crystal growth, spectroscopy, and diode pumped laser performance of Pr,Mg:$SrAl_{12}O_{19}$. *Applied Physics B*, 102(4):731–735, 2011.

[131] T. Calmano, J. Siebenmorgen, F. Reichert, M. Fechner, A. G. Paschke, N. O. Hansen, K. Petermann, and G. Huber. Crystalline Pr:$SrAl_{12}O_{19}$ waveguide laser in the visible spectral region. *Optics Letters*, 36(23):4620–2, 2011.

[132] T.N. Nadzhina, Pobedimskaya E.A., and N.V. Belov. Crystal structure of strontium aluminate $Sr_4Al_4O_2[Al_{10}O_{23}]$. 21:826–828, 1976.

[133] D. Wang, M. Q. Wang, and G. L. Lu. Synthesis, crystal structure and X-ray powder diffraction data of the phosphor matrix $4\,SrO \cdot 7\,Al_2O_3$. *Journal of Materials Science*, 34(20):4959–4964, 1999.

[134] M. Capron, F. Fayon, D. Massiot, and A. Douy. $Sr_4Al_{14}O_{25}$: Formation, stability, and Al-27 high-resolution NMR characterization. *Chemistry of Materials*, 15(2):575–579, 2003.

[135] Y. Lin, Z. Tang, Z. Zhang, and C.W. Nan. Anomalous luminescence in $Sr_4Al_{14}O_{25}$:Eu,Dy phosphors. *Applied Physics Letters*, 81(6):996, 2002.

[136] G. Inan Akmehmet, S. Šturm, L. Bocher, M. Kociak, B. Ambrožič, C.W. Ow-Yang, and C. W. Ow-Yang. Structure and luminescence in long persistence Eu, Dy, and B codoped strontium aluminate phosphors: The boron effect. *Journal of the American Ceramic Society*, 99(6):2175–2180, 2016.

[137] H.N. Luitel, T. Watari, R. Chand, T. Torikai, and M. Yada. Giant improvement on the afterglow of $Sr_4Al_{14}O_{25}$:Eu^{2+},Dy^{3+} phosphor by systematic investigation on various parameters. *Journal of Materials*, 2013:1–10, 2013.

[138] S. Nagamani and B.S. Panigrahi. Luminescence properties of $SrO-Al_2O_3$:Eu^{2+},Dy^{3+} prepared at different temperatures. *Journal of the American Ceramic Society*, 93(11):3832–3836, 2010.

[139] T.N. Nadezhina, E.A. Pobedimskaya, and N.V. Belov. The coordination polyhedra of strontium in the structures $Na_4SrGe_3O_3[GeO_4]_3$, $Sr_3[Ge_3O_9]$, $Sr_4Al_4O_2[Al_{10}O_{23}]$ and $Sr_2(OH_2)Cu(OH)_4$. *Kristallografiya*, 25(5):938–943, 1980.

[140] Y. Lu, Y. Li, Y. Xiong, D. Wang, and Q. Yin. $SrAl_2O_4$:Eu^{2+},Dy^{3+} phosphors derived from a new sol-gel route. *Microelectronics Journal*, 35(4):379–382, 2004.

[141] C. Zhao, D. Chen, Y. Yuan, and M. Wu. Synthesis of $Sr_4Al_{14}O_{25}$:Eu^{2+},Dy^{3+} phosphor nanometer powders by combustion processes and its optical properties. *Materials Science and Engineering: B*, 133(1-3):200–204, 2006.

[142] K. Toh, K. Sakasai, T. Nakamura, K. Soyama, S. Nagata, B. Tsuchiya, and T. Shikama. Proton-induced fluorescence and long lasting emission of $Sr_4Al_{14}O_{25}$:Eu^{2+},$Dy_3{}^{+}$. *2009 Ieee Nuclear Science Symposium Conference Record, Vols 1-5*, pages 1427–1430, 2009.

[143] S. Demirci, S. Gültekin, S.A. Akalin, Ö. Öter, K. Ertekin, and E. Celik. Synthesis and spectral characterization of $Sr_4Al_{14}O_{25}:Eu^{2+}/Dy^{3+}$ blue-green phosphorous powders by sol-gel method. *Materials Science in Semiconductor Processing*, 31:611–617, 2015.

[144] B.-J. Kim, Z. Hasan, and J.-S. Kim. Synthesis and characterization of long persistence $Sr_4Al_{14}O_{25}:Eu^{2+},Dy^{3+}$ phosphor prepared by combustion method. *Journal of Ceramic Processing Research*, 14(5):601–605, 2013.

[145] N. Thompson, P. Murugaraj, C. Rix, and D.E. Mainwaring. Role of oxidative pre-calcination in extending blue emission of $Sr_4Al_{14}O_{25}$ nanophosphors formed with microemulsions. *Journal of Alloys and Compounds*, 537:147–153, 2012.

[146] Q. Xiao, L. Xiao, Y. Liu, X. Chen, and Y. Li. Synthesis and luminescence properties of needle-like $SrAl_2O_4$:Eu,Dy phosphor via a hydrothermal co-precipitation method. *Journal of Physics and Chemistry of Solids*, 71(7):1026–1030, 2010.

[147] N. Suriyamurthy and B. S. Panigrahi. Luminescence studies during combustion synthesis of a long afterglow phosphor $Sr_4Al_{14}O_{25}:Eu^{2+},Dy^{3+}$. *Indian Journal of Engineering and Materials Sciences*, 16(3):178–180, 2009.

[148] S.-S. Yao, Y.-Y. Li, D.-H. Chen, W.-J. Tang, and Y.-H. Peng. Combustion synthesis and luminescent properties of green-emitting phosphor (Sr, Zn) Al_2O_4: Eu^{2+}, B^{3+} for white light emitting diodes (WLED). *Central European Journal of Physics*, 7(1):96–101, 2008.

[149] D. Jia. $Sr_4Al_{14}O_{25}:Eu^{2+}$ nanophosphor synthesized with salted sol-gel method. *Electrochemical and Solid-State Letters*, 9(10):H93, 2006.

[150] N. Suriyamurthy and B. S. Panigrahi. Effects of non-stoichiometry and substitution on photoluminescence and afterglow luminescence of $Sr_4Al_{14}O_{25}:Eu^{2+},Dy^{3+}$ phosphor. *Journal of Luminescence*, 128(11):1809–1814, 2008.

[151] H.N. Luitel, T. Watari, T. Torikai, and M. Yada. Preparation and characteristics of Eu and Dy doped $Sr_4Al_{14}O_{25}$ phosphor. *Materials Science Forum*, 569:249–252, 2008.

[152] Z.-X. Yuan, C.-K. Chang, D.-L. Mao, and W.J. Ying. Effect of composition on the luminescent properties of $Sr_4Al_{14}O_{25}:Eu^{2+}$, Dy^{3+} phosphors. *Journal of Alloys and Compounds*, 377(1-2):268–271, 2004.

[153] D. Dacyl, D. Uhlich, and T. Jüstel. The effect of calcium substitution on the afterglow of Eu^{2+}/Dy^{3+} doped $Sr_4Al_{14}O_{25}$. *Central European Journal of Chemistry*, 7(2):164–167, 2009.

[154] C. R. Garcia, J. Oliva, M. T. Romero, and L. A. Diaz-Torres. Enhancing the photocatalytic activity of $Sr_4Al_{14}O_{25}$:Eu^{2+},Dy^{3+} persistent phosphors by codoping with Bi^{3+} ions. *Photochemistry and Photobiology*, 92(2):231–237, 2016.

[155] R. Zhong, J. Zhang, X. Zhang, S. Lu, and X. Wang. Red phosphorescence in $Sr_4Al_{14}O_{25}$: $Cr_3{}^+$,Eu^{2+},Dy^{3+} through persistent energy transfer. *Applied Physics Letters*, 88(20):201916, 2006.

[156] S.H. Han and Y.J. Kim. Luminescent properties of Ce and Eu doped $Sr_4Al_{14}O_{25}$ phosphors. *Optical Materials*, 28(6-7):626–630, 2006.

[157] S.K. Sharma, S.S. Pitale, M. Manzar Malik, R. N. Dubey, and M. S. Qureshi. Luminescence studies on the blue-green emitting $Sr_4Al_{14}O_{25}$:Ce^{3+} phosphor synthesized through solution combustion route. *Journal of Luminescence*, 129(2):140–147, 2009.

[158] G. N. Nikhare, S. C. Gedam, and S. J. Dhoble. Luminescence in $Sr_4Al_{14}O_{25}$:Ce(3+) aluminate phosphor. *Luminescence*, 30(2):163–167, 2015.

[159] S. Sakirzanovas, A. Katelnikovas, D. Dutczak, A. Kareiva, and T. Jüstel. Synthesis and Sm^{2+}/Sm^{3+} doping effects on photoluminescence properties of $Sr_4Al_{14}O_{25}$. *Journal of Luminescence*, 131(11):2255–2262, 2011.

[160] H.N. Luitel, T. Watari, R. Chand, T. Torikai, and M. Yada. Photoluminescence properties of a novel orange red emitting $Sr_4Al_{14}O_{25}$:Sm^{3+} phosphor and PL enhancement by Bi^{3+} co-doping. *Optical Materials*, 34(8):1375–1380, 2012.

[161] L. Chen, Y. Zhang, F. Liu, W. Zhang, X. Deng, S. Xue, A. Luo, Y. Jiang, and S. Chen. The red luminescence of $Sr_4Al_{14}O_{25}$:Mn^{4+} enhanced by coupling with the $SrAl_2O_4$ phase in the $3\,SrO \cdot 5\,Al_2O_3$ system. *Physica Status Solidi (a)*, 210(9):1791–1796, 2013.

[162] M. Peng, X. Yin, P.A. Tanner, C. Liang, P. Li, Q. Zhang, J. Qiu, and A. Srivastava. Orderly-layered tetravalent manganese-doped strontium aluminate $Sr_4Al_{14}O_{25}$:Mn^{4+}: An efficient red phosphor for warm white light emitting diodes. *Journal of the American Ceramic Society*, 96(9):2870–2876, 2013.

[163] M. Peng, X. Yin, P.A. Tanner, M.G. Brik, and P. Li. Site occupancy preference, enhancement mechanism, and thermal resistance of Mn^{4+} red luminescence in $Sr_4Al_{14}O_{25}$:Mn^{4+} for warm WLEDs. *Chemistry of Materials*, 27(8):2938–2945, 2015.

[164] A. J. Lindop and D. W. Goodwin. The refined structure of $SrO \cdot 2\,Al_2O_3$. *Acta Crystallographica Section B Structural Crystallography and Crystal Chemistry*, 28(8):2625–2626, 1972.

[165] K. I. Machida, G. Y. Adachi, J. Shiokawa, M. Shimada, and M. Koizumi. Structure of strontium tetraaluminate β-$SrAl_4O_7$. *Acta Crystallographica Section B Structural Crystallography and Crystal Chemistry*, 38(3):889–891, 1982.

[166] X. J. Wang, S. H. Huang, L. Z. Lu, W. M. Yen, A. M. Srivastava, and A. A. Setlur. Measurement of quantum efficiency in Pr^{3+}-doped $CaAl_4O_7$ and $SrAl_4O_7$ crystals. *Applied Physics Letters*, 79(14):2160–2162, 2001.

[167] K.R.S. Preethi, C.-H. Lu, J. Thirumalai, R. Jagannathan, T. S. Natarajan, N. U. Nayak, I. Radhakrishna, M. Jayachandran, and D. C. Trivedi. $SrAl_4O_7$:Eu^{2+} nanocrystals: synthesis and fluorescence properties. *Journal of Physics D: Applied Physics*, 37(19):2664–2669, 2004.

[168] N. K. Giri, S. K. Singh, D. K. Rai, and S. B. Rai. $SrAl_4O_7$:Tm^{3+}/Yb^{3+} nanocrystalline blue phosphor: structural, thermal and optical properties. *Applied Physics B-Lasers and Optics*, 99(1-2):271–277, 2010.

[169] B. Cheng, Z. Zhang, Z. Han, Y. Xiao, and S. Lei. $SrAl_xO_y$:Eu^{2+},Dy^{3+} ($x = 4$) nanostructures: Structure and morphology transformations and long-lasting phosphorescence properties. *CrystEngComm*, 13(10):3545, 2011.

[170] X. Yuan, Y. Xu, G. Huang, and C. Zeng. Synthesis of strontium dialuminate via an ethylenediaminetetraacetic acid precursor. *Journal of the American Ceramic Society*, 90(7):2283–2286, 2007.

[171] M. Karmaoui, M. G. Willinger, L. Mafra, T. Herntrich, and N. Pinna. A general nonaqueous route to crystalline alkaline earth aluminate nanostructures. *Nanoscale*, 1(3):360–365, 2009.

[172] D. Singh, V. Tanwar, A.P. Simantilleke, S. Bhagwan, B. Mari, P.S. Kadyan, K.C. Singh, and I. Singh. Synthesis and enhanced luminescent characterization of $SrAl_4O_7$:Eu^{2+},RE^{3+} (RE = Nd, Dy) nanophosphors for light emitting applications. *Journal of Materials Science: Materials in Electronics*, 27(5):5303–5308, 2016.

[173] M.G. Eskin, H. Kurt, M.A. Gulgun, and C.W. Ow-Yang. The effect of boron on processing and phosphorescence behavior of $SrAl_4O_7$ (SA2) co-doped with Eu^{2+} and Dy^{3+}. *MRS Proceedings*, 1309, 2011.

[174] M. Akiyama, C.-N. Xu, Y. Liu, K. Nonaka, and T. Watanabe. Influence of Eu, Dy co-doped strontium aluminate composition on mechanoluminescence intensity. *Journal of Luminescence*, 97(1):13–18, 2002.

[175] W. Jia, H. Liu, H. Yuan, L. Lu, and W.M. Yen. Luminescence spectra of divalent europium ions doped in $SrAl_{407}$. *Luminiescent materials VI*, 97(29):368, 1998.

[176] A. N. Yerpude and S. J. Dhoble. Combustion synthesis of $SrAl_4O_7$:Eu^{2+}, Dy^{3+}, Gd^{3+} long lasting phosphor. *IOP Conference Series: Materials Science and Engineering*, 73:012126, 2015.

[177] X. Wang, S. Huang, J. Zhang, and W.M. Yen. Spectral properties and quantum efficiency of optical emission in rare earth doped crystals. In *Journal of Physics: Conference Series*, volume 28, page 18. IOP Publishing, 2006.

[178] S. K. Sharma, S. S. Pitale, M. M. Malik, T. K. GunduRao, S. Chawla, M. S. Qureshi, and R. N. Dubey. Spectral and defect analysis of Cu-doped combustion synthesized new $SrAl_4O_7$ phosphor. *Journal of Luminescence*, 130(2):240–248, 2010.

[179] Jisha V.T. and G. Suresh. Structural and optical properties of dy doped sol gel synthesized $SrAl_4O_7$ nanaparticle. *International Journal of Scientific Research*, 5(4):443–447, 2016.

[180] A.K. Choubey, N. Brahme, S.J. Dhoble, D. P. Bisen, and K.B. Ghormare. Thermoluminescence characterization of γ-ray irradiated Dy^{3+} activated $SrAl_4O_7$ nanophosphor. *Advanced Materials Letters*, 5(7):396–399, 2014.

[181] A.N. Yerpude, S.J. Dhoble, B. Ramesh, and B.D.P. Raju. Photoluminescence and decay properties of Sm^{3+} and Dy^{3+} in $SrAl_4O_7$ phosphor. *Advanced Materials Letters*, 6(12):1111–1115, 2015.

[182] M. A. Kale, S. A. Kale Kale, and C. P. Joshi. Preparation and characterization of Pb^{2+} and Ce^{3+} activated strontium aluminate based phosphor. *Physics and Chemistry of Glasses: European Journal of Glass Science and Technology Part B*, 57(3):130–132, 2016.

[183] A. D. McNaught and A. Wilkinson. *IUPAC. Compendium of Chemical Terminology, 2nd ed. (the "Gold Book").* Blackwell Scientific Publications, Oxford, 1997.

[184] R. Ropp. *Luminescence and the Solid State, 2nd Edition*. Elsevier Science, 2004.

[185] K.-D. Gundermann. Luminescence, 2016.

[186] J. Emsley. *The Shocking History of Phosphorus: A Biography of the Devil's Element*. Pan, 2001.

[187] D. Jia and W. M. Yen. Trapping mechanism associated with electron delocalization and tunneling of $CaAl_2O_4$:Ce^{3+}, a persistent phosphor. *Journal of The Electrochemical Society*, 150(3):H61, 2003.

[188] G.F.J. Garlick. Luminescence. In S. Flugge, editor, *Light and Matter II / Licht und Materie II*, pages 1–128. Springer Berlin Heidelberg, Berlin, Heidelberg, 1958.

[189] Kartik N. Shinde, S. J. Dhoble, H. C. Swart, and Kyeongsoon Park. *Phosphate Phosphors for Solid-State Lighting*, volume 174 of *Springer Series in Materials Science*. Springer-Verlag Berlin Heidelberg, 2012.

[190] M. Lastusaari, T. Laamanen, M. Malkamäki, K.O. Eskola, A. Kotlov, S. Carlson, E. Welter, H.F. Brito, M. Bettinelli, H. Jungner, and J. Hölsä. The bologna stone: history's first persistent luminescent material. *European Journal of Mineralogy*, 24(5):885–890, 2012.

[191] H. Yamamoto and T. Matsuzawa. Mechanism of long phosphorescence of $SrAl_2O_4$:Eu^{2+},Dy^{3+} and $CaAl_2O_4$:Eu^{2+},Nd^{3+}. *Journal of Luminescence*, 72-74:287–289, 1997.

[192] Y. Lin, Z. Tang, Z. Zhang, X. Wang, and J. Zhang. Preparation of a new long afterglow blue-emitting $Sr_2MgSi_2O_7$-based photoluminescent phosphor. *Journal of Materials Science Letters*, 20(16):1505–1506, 2001.

[193] T. Aitasalo, P. Deren, J. Holsa, H. Jungner, J. C. Krupa, M. Lastusaari, J. Legendziewicz, J. Niittykoski, and W. Strek. Persistent luminescence phenomena in materials doped with rare earth ions. *Journal of Solid State Chemistry*, 171(1-2):114–122, 2003.

[194] P. Dorenbos. Mechanism of persistent luminescence in Eu^{2+} and Dy^{3+} codoped aluminate and silicate compounds. *Journal of The Electrochemical Society*, 152(7):H107, 2005.

[195] T. Aitasalo, J. Holsa, H. Jungner, M. Lastusaari, and J. Niittykoski. Thermoluminescence study of persistent luminescence materials: Eu^{2+}- and R^{3+}-doped calcium aluminates, $CaAl_2O_4$:Eu^{2+},R^{3+}. *The Journal of Physical Chemistry B*, 110(10):4589–4598, 2006.

[196] J. Trojan-Piegza, E. Zych, J. Hoolsa, and J. Niittykoski. Spectroscopic properties of persistent luminescence phosphors: Lu_2O_3:Tb^{3+},M^{2+} (M = Ca, Sr, Ba). *The Journal of Physical Chemistry C*, 113(47):20493–20498, 2009.

[197] L.C.V. Rodrigues, H.F. Brito, J. Holsa, R. Stefani, M.C. F. C. Felinto, M. Lastusaari, T. Laamanen, and L.A.O. Nunes. Discovery of the persistent luminescence mechanism of $CdSiO_3$:Tb^{3+}. *The Journal of Physical Chemistry C*, 116(20):11232–11240, 2012.

[198] J.M. Carvalho, L.C.V. Rodrigues, J. Hölsä, M. Lastusaari, L.A.O. Nunes, M.C F.C. Felinto, O.L. Malta, and H.F. Brito. Influence of titanium and lutetium on the persistent luminescence of ZrO_2. *Optical Materials Express*, 2(3):331, 2012.

[199] Z. Pan, Y. Y. Lu, and F. Liu. Sunlight-activated long-persistent luminescence in the near-infrared from Cr(3+)-doped zinc gallogermanates. *Nat Mater*, 11(1):58–63, 2012.

[200] J. Hölsä, A. Kotlov, T. Laamanen, M. Lastusaari, M. Lindström, and M. Malkamäki. Yellow persistent luminescence of the Sr_3SiO_5:Eu^{2+},R^{3+} materials.

[201] H.M. Rietveld. A profile refinement method for nuclear and magnetic structures. *Journal of Applied Crystallography*, 2(2):65–71, 1969.

[202] H.M. Rietveld. Line profiles of neutron powder-diffraction peaks for structure refinement. *Acta Crystallographica*, 22(1):151–152, 1967.

[203] V.K. Pecharsky and P.Y. Zavalij. *Fundamentals of powder diffraction and structural characterization of materials*. Springer, 2009.

[204] W. H. Bragg and W. L. Bragg. The reflection of X-rays by crystals. *Proceedings of the Royal Society A: Mathematical, Physical and Engineering Sciences*, 88(605):428–438, 1913.

[205] R. W. Cheary and A. Coelho. A fundamental parameters approach to X-ray line-profile fitting. *Journal of Applied Crystallography*, 25(2):109–121, 1992.

[206] J. Rodriguez-Carvajal. *An introduction to the program FullProf 2000*. Laboratoire Léon Brillouin, CEA-CNRS: Saclay, France, 2001.

[207] K. Pearson. Mathematical contributions to the theory of evolution. XIX. second supplement to a memoir on skew variation. *Philosophical Transactions of the Royal Society A: Mathematical, Physical and Engineering Sciences*, 216(538-548):429–457, 1916.

[208] P. Thompson, D. E. Cox, and J. B. Hastings. Rietveld refinement of debye-scherrer synchrotron X-ray data from Al_2O_3. *Journal of Applied Crystallography*, 20(2):79–83, 1987.

[209] G. Caglioti, A. Paoletti, and F. P. Ricci. Choice of collimators for a crystal spectrometer for neutron diffraction. *Nuclear Instruments*, 3(4):223–228, 1958.

[210] G. S. Pawley. Unit-cell refinement from powder diffraction scans. *Journal of Applied Crystallography*, 14(6):357–361, 1981.

[211] A. Le Bail, H. Duroy, and J. L. Fourquet. Ab-initio structure determination of $LiSbWO_6$ by X-ray powder diffraction. *Materials Research Bulletin*, 23(3):447–452, 1988.

[212] R. A. Young. *The Rietveld Method*. Oxford university press, 1995.

[213] Brian H. Toby. R factors in Rietveld analysis: How good is good enough? *Powder Diffraction*, 21(01):67–70, 2006.

[214] N. Dubnikova, E. Garskaite, A. Beganskiene, and A. Kareiva. Sol-gel synthesis and characterization of sub-microsized lanthanide (Ho, Tm, Yb, Lu) aluminium garnets. *Optical Materials*, 33, 2011.

[215] B. Schrader. *Infrared and Raman spectroscopy: methods and applications*. John Wiley & Sons, 2008.

[216] K. Nakamoto. *Infrared and Raman Spectra of Inorganic and Coordination Compounds*. John Wiley and Sons, New York, 1986.

[217] Y. Liu, Z.-F. Zhang, B. King, J. Halloran, and R.M. Laine. Synthesis of yttrium aluminium garnet from yttrium and aluminium isobutyrate precursors. *Journal of the American Ceramic Society*, 79, 1996.

[218] M. Chroma, J. Pinkas, I. Pakutinskiene, A. Beganskiene, and A. Kareiva. Processing and characterization of sol-gel fabricated mixed metal aluminates. *Ceramics International*, 31, 2005.

[219] S. Cizauskaite, S. Johnsen, J.-E. Jørgensen, and A. Kareiva. Sol-gel preparation and characterization of non-substituted and Sr-substituted gadolinium cobaltates. *Materials Chemistry and Physics*, 125, 2011.

[220] A. Kareiva. Aqueous sol-gel synthesis methods for the preparation of garnet crystal structure compounds. *Materials Science (Medžiagotyra)*, 17(4):427–436, 2011.

[221] A. Katelnikovas, H. Bettentrup, D. Uhlich, S. Sakirzanovas, T. Jüstel, and A. Kareiva. Synthesis and optical properties of Ce^{3+}-doped $Y_3Mg_2AlSi_2O_{12}$ phosphors. *Journal of Luminescence*, 129, 2009.

[222] D Haranath, P. Sharma, H. Chander, A. Ali, N. Bhalla, and S.K. Halder. Role of boric acid in synthesis and tailoring the properties of calcium aluminate phosphor. *Materials chemistry and physics*, 101(1):163–169, 2007.

[223] Z. Wu, J. Shi, J. Wang, M. Gong, and Q. Su. Synthesis and luminescent properties of $Sr_4Al_{14}O_{25}:Eu^{2+}$ blue-green emitting phosphor for white light-emitting diodes (LEDs). *Journal of Materials Science: Materials in Electronics*, 19(4):339–342, 2007.